NMR Investigation of Polymer Nanocomposites

Dissertation

zur Erlangung des Doktorgrades der Naturwissenschaften

(Dr. rer. nat.)

der

Naturwissenschaftlichen Fakultät II

Chemie, Physik und Mathematik

der Martin-Luther-Universität

Halle-Wittenberg

vorgelegt von

Frau Mozhdeh Abbasi

Contents

Introduction

The concepts of nanotechnology were first discussed in the late 1950s by Nobel laureate physicist Richard Feynman in a lecture entitled "There is a lot of space at the bottom", who proposed the synthesis of substances through the direct manipulation of atoms [1]. With time, the significance of this revolutionary idea became evident when researchers discovered the profound impact of size on the physicochemical properties of composites, particularly at the nanoscale where properties such as adhesion, dispersion, and bonding are amplified. Moreover, unique phenomena like electromagnetic forces and quantum confinement enhance intermolecular bonding and surface energy, making them invaluable in developing advanced nanotechnology materials [2].

Nanocomposites consist of multiple components, with at least one having dimensions under 100 nanometers [2–4]. Unlike their individual constituents, these materials boast distinctive properties. Depending on the matrix material chosen, nanocomposites can be categorized variably. Among matrices, polymers are a popular choice as a host for nanocomposites due to their lightweight nature, versatility, and durability. These long-chain molecules can exhibit a wide range of fascinating physical properties, including the ability to undergo large-scale conformational changes. When constrained within limited spaces, the motion and conformational behavior of polymers can be significantly altered, resulting in novel and potentially useful physical properties [2].

Toyota's research group was among the first to propose the use of nano-scale sheets of a silicate material, known as montmorillonite clay, to improve the mechanical and thermal properties of polymers. The development of properties of composites in the 1990s was a significant breakthrough in materials science and opened up a world of possibilities for various industries. These polymer nanocomposites (PNCs) have demonstrated remarkable capabilities, higher stiffness, strength, thermal stability, and barrier properties at low nanoparticle content compared to traditional plastics with

micrometer-sized particles and are particularly useful in the transportation industry, where their high strength, wear resistance, and traction makes them an ideal choice for various parts of ground and air vehicles [5–9]. In addition, where durability and performance are important, their properties make them suitable for sports equipment. PNCs also show great potential in membrane and separation technologies, such as gas separation and water filtration [10], due to their exceptional barrier, permeability, and selectivity properties. Furthermore, they are also used in food packaging to maintain freshness and extend the shelf life of food products [11]. Thus, with the potential to improve material properties while maintaining low costs and weight, polymer nanocomposites are a promising solution for a wide range of industries [3, 12–15].

When bare nanoparticles (NPs) are introduced into a polymer melt, achieving a uniform dispersion is typically contingent upon favorable interactions between the polymer and NPs. Under such conditions, certain polymer chains tend to adhere to the surface of NPs, creating an essentially irreversible layer. In recent years, it has been recognized that the properties of PNCs are significantly influenced by this nanometer-thin layer with slowed-down dynamics [16–18]. While polymer nanocomposites have seen significant advancements and found widespread applications, the precise polymer configuration within the interfacial region remains a subject of speculation. This is partly due to the complexity of polymer nanocomposites and the need to re-examine polymer physics principles, as well as a lack of reliable experimental data. Thus, understanding the properties of this interfacial layer is critical to optimizing the design and performance of PNCs and is critical to determining many macroscopic properties of the composite [19–25].

One key aspect of this complexity lies in elucidating how mechanical, thermal, and structural properties are influenced by a myriad of factors, such as intermolecular interactions, and non-equilibrium factors, like the choice of casting solvent, the rate of solvent evaporation, and processing temperature. Addressing these challenges is vital for developing strategies to improve miscibility between NPs and polymers [24, 26–28]. Recent experimental findings have indicated that the thickness of the interfacial layer can vary depending on the size of the NPs. Specifically, an interfacial layer of approximately 1 nm is observed for NPs with a diameter close to 10 nm, while the thickness increases to about 4-5 nm for flat surfaces [29]. Despite these observations,

the precise factors determining this layer's thickness, its temporal stability, and the influence of NP shape remain elusive.

This interfacial layer can be identified using advanced techniques such as Small Angle X-ray Scattering (SAXS) and Small Angle Neutron Scattering (SANS). These methods detect changes in the density of the polymer surrounding the nanoparticles. Other techniques such as Differential Scanning Calorimetry (DSC) and Broadband Dielectric Spectroscopy (BDS) measurements have also detected the presence of the interfacial layer with a significant broadening of the calorimetric glass transition and slower segmental dynamics [17–21, 25, 30–32]. Several coarse-grained simulations of composite materials also have revealed that the interfacial layer has a unique structure and dynamics that are different from the bulk polymer [33–35].

To address the complexity of these modern polymer systems, encompassing both their structural intricacies and dynamic behavior, advanced capabilities of NMR techniques are used in this dissertation. Although more primitive techniques such as low resolution ^{1}H time domain spectroscopy have been used to describe the mesoscopic structures and insights into the volume or size of nanoscale domains in multiphase systems [22, 24, 36, 37], but to identify chemical components and elucidate aspects of chain behavior, configurations, and compositions, high-resolution ^{1}H and ^{13}C MAS spectra were required. Challenges arose when studying the dynamics of polymers affected by nanoparticles in the narrow interfacial region of a few nanometers. Advanced NMR techniques became necessary to quantitatively explore the dynamics of complex chains spanning a wide range of time scales [38, 39]. These methods allowed us to detect intra and intermolecular spin interactions, and the signal strength was used as a quantitative measurement of the concentration of different components in a sample [22, 24, 36, 39–44].

The motivation behind the presented thesis lies in the growing demand to elucidate the microscopic complexities of Poly(ethylene oxide) (PEO) chain dynamics, especially in the confined interface region, as well as the quantitative characterization of the thickness of this interfacial layer. PEO, a water-soluble polymer renowned for its rapid dynamics in the amorphous phase and distinguished by low glass transition and melting temperatures, offers the flexibility for measurements across a broad temperature spectrum making it a prominent choice in the research arena, being a frequently studied model for nanocomposites and readily available across a range of

molecular weights [24, 25, 45, 46]. An important foundation of our work is the recent study within our research group by Golitsyn et al. [22]. Their noteworthy finding, the lack of heat-induced softening in the PEO/SiO$_2$ system, points to the absence of a distinct gradient in the PEO/SiO$_2$ nanocomposite's glass transition temperature. This characteristic notably differentiates the PEO/SiO$_2$ nanocomposite from its counterparts in analogous situations. Building on these insights, our research delves deeper into the complex area of PEO chain dynamics, particularly in the confined interface region.

In this dissertation, a comprehensive study of polymer nanocomposites is presented, with a particular emphasis on how confinement affects polymer dynamics. Chapter 2 delves into the foundational concepts of polymer nanocomposites. This chapter initiates with an exploration of polymers, detailing the phenomenon of the glass transition through the lens of the free volume theory, and subsequently discussing the intricacies of chain dynamics in polymer melts, then transitions into a thorough examination of fillers, spotlighting spherical silica nanoparticles and clays as pivotal components. The latter section of this chapter is dedicated to model polymer nanocomposites, emphasizing the criticality of achieving optimal dispersion and the factors influencing it. A notable focus is placed on polymer conformation at interfaces, exploring how varying levels of confinement can impact their structure and behavior.

Chapter 3 provides an in-depth exploration of NMR - a key tool that sheds light on polymer structures and their dynamic behavior. In particular, this chapter highlights the interplay between relaxation mechanisms and molecular dynamics and emphasizes the central role of NMR in their study. Special emphasis is placed on ^{1}H NMR experiments, especially free induction decay (FID) analysis at high and low magnetic fields, which provides a comprehensive understanding of the phase behavior of our systems. This chapter addresses the utility of techniques such as saturation recovery and the differences between echoes and refocusing. The chapter further addresses the intricacies of magic-angle spinning, a technique fundamental to high-resolution NMR. Venturing into ^{13}C NMR experiments, we discuss direct-polarization, the subtleties of cross-polarization, decoupling, and specific methods such as the Torchia approach to measure ^{13}C T_1 and ^{13}C $T_{1\rho}$ measurement are discussed.

In Chapter 4, we detail the specifications of the samples and outline the techniques employed in the experiments. The experimental results are discussed in chapters 5 and 6. Chapter 5 presents a case study of Polyethylenoxide/Nanoclay nacre-mimetic model nanocomposites, as documented in Ref [25]. What sets this case apart is its fixed d-spacing between clay sheets, a feature that contrasts with typical behaviors where interlayer spacing expands with an increase in polymer content. In Chapter 6, we examine the Polyethylenoxide/Silica model nanocomposites. This system is particularly fascinating as it reveals unexpected internal molecular mobility within regions typically characterized as immobilized (part of the results are published in Ref [24]). The impact of these different confinement environments on polymer dynamics is investigated. Additionally, we address the semiquantitative clarification of tight ethanol and water surface contacts in these thin molecular layers. Chapter 7 will then provide a comprehensive summary of the entire work.

In this thesis, artificial intelligence (GPT-3.5) was used exclusively for improving the language and clarity of my writing. Specifically, I employed it to rephrase certain paragraphs to ensure a higher level of English proficiency. The content, structure, and arguments presented remain entirely my own.

Polymer Nanocomposites

The theoretical overview in this chapter is based on the books by Rubinstein and Colby [47], Strobl [48], Sperling [49], Pielichowski and Majka [2], Koo [4], and Schönhals [50].

2.1   Polymer Chain Behavior: Properties and Movements

Polymers are large molecules made up of repeating units known as monomers. A polymer made up of a single type of monomer unit is referred to as a homopolymer, while a polymer composed of multiple types of monomers is known as a hetero or copolymer. The degree of polymerization is the number of backbone bonds in a polymer. Polymers consisting of a small number of monomers, typically less than 20, are known as oligomers. As the degree of polymerization increases, the physical properties of the polymer change, which can affect its potential uses. The architecture of the polymer, such as linear, branched, or crosslinked also plays an important role in determining its properties. Thus, the properties of the polymer can be tailored by manipulating the microstructure of the polymer chain.

Polymers can be natural or synthetic. Synthetic polymers are man-made polymers that are not found naturally. They are typically produced from petrochemicals or other raw materials through chemical processes like plastics, which are used in a wide variety of applications including packaging, construction, and automotive industries; rubber, which is used for tires, belts, and seals; and fibers, which are used in clothing, textiles, and other products. Synthetic polymers can be designed to have specific properties, such as strength, flexibility, and resistance to heat and chemicals, making them useful in a wide range of applications.

In polymerization, monomers covalently bond together to form long chains. The molar mass of the polymer can be determined by multiplying the molar mass of the monomer with the number of monomer units in the chain. It is crucial to deter-

mine the molecular conformation and configuration of polymers to understand their physical behavior. The inherent properties of polymer materials, such as flexibility, tension, and stiffness, are deeply tied to the organization of their constituent atoms or molecules. This organization, or arrangement of atoms or molecules in space, is influenced by the configuration that achieves a more stable state and minimizes interatomic energy.

At the core of polymer dynamics are two primary types of movements: vibrational and rotational. The vibrational motions involve rapid oscillations in bond lengths and angles, occurring at high frequencies. Although these vibrations contribute to the internal energy of the polymer, they do not significantly alter its overall shape or conformation. In contrast, rotational motions around bonds—especially carbon-carbon bonds—play a crucial role in determining the polymer's structure. These rotations can lead to significant changes in the chain's conformation, allowing it to adopt various shapes. For instance, a polymer chain can transition from a linear arrangement to a more coiled configuration through these rotational movements. The conformational states of a polymer chain can be characterized by specific angles associated with its bonds. The most stable arrangement is known as the trans state, where the chain adopts a zigzag conformation with no rotation (0° angle). This state represents the lowest energy configuration. Conversely, there are also higher-energy states, such as gauche+ and gauche-, which correspond to rotational angles of +120° and -120°, respectively. Transitions between these states are vital for understanding how polymers can flex and adapt their shapes under different conditions.

The internal dynamics of a polymer, such as its strength and flexibility, depend on the energy difference between different rotational isomeric states and the height of the barriers between them. When the torsion angles along the length of an aliphatic polymer chain are all in the trans mode, resulting in a zig-zag conformation in a plane, the end-to-end distance of the chain has its maximum value, resulting in the bonds being aligned in a straight line, $R_{max}=nlcos(\theta/2)$, with n, the number of main chain bonds and l, its length. However, when gauche conformations are populated, due to the greater number of potential arrangements available for polymer segments the entropy of the gauche conformation exceeds that of the trans conformation and the chain becomes more flexible. This is the case at a higher temperature at which the chains adopt the different conformations more easily. Usually, all-trans segments

consist of less than ten main chain bonds, and the majority of synthetic polymers exhibit considerable flexibility.

An equivalent freely jointed chain can be used as a straightforward representation for all flexible polymers, where the polymer chain is divided into N_s freely jointed segments, with the same length, known as the Kuhn length, $a_k = R_{max}/N_s$. This length is a measure of the stiffness of a polymer chain. The orientation of a Kuhn segment is independent of other segments beyond the Kuhn length, a requisite condition for the random walk model. The chain appears rod-like on length scales smaller than the Kuhn length, but it becomes more flexible on larger scales. It should be emphasized that ideal chain models do not take into account the interactions between monomers and assume that the polymer chains can freely overlap with each other without any energetic penalty. However, in real polymer chains, the excluded volume interaction which is caused by the repulsive forces between any two monomers along the chain changes this situation and leads to a reduction in the number of possible conformations that the polymer can adopt. In a good solvent, where the effective interaction of monomer-monomer energy is always repulsive, the chains consequently expand. At the peculiar temperature, so-called θ-temperature, the excluded volume effect apparently disappears and the chains behave as an ideal chain. The conformations of long chains polymer melt that have been heated to a temperature above their glass transition are also nearly ideal because the excluded volume interactions between the monomers are partially screened by the presence of other chains.

2.1.1 Glass transition; free volume theory

The state of a polymer varies depending on the temperature and the time devoted to the experiment. By heating a polymer that is in its glassy state, the molecules slowly begin to perform a long-range coordinated motion. The temperature at which the glass begins to soften is called the glass transition temperature. At this temperature, the polymer undergoes a sudden change in its mechanical and thermal properties, which can be influenced by the presence of free volume in the material. It is believed that molecular motion in the polymer is not possible without empty volume in neighborhoods. In the absence of free volume, a material will have an infinitely high glass transition temperature, as there is no space for the molecules to move around and the material is more resistant to deformation.

As the temperature increases, the molecular motion of the material increases, and the polymer begins to vibrate, the free volume fraction in the polymer system also increases due to thermal expansion and the relaxation time decreases. This behavior is reflected in the Williams-Landel-Ferry (WLF) equation. This analytical relationship between polymer melt viscosity and free volume drives a logarithmic relationship between time and temperature. The logarithm of scaled time in the context of the WLF equation refers to the time it takes for a material to relax or respond to external deformation. This means the material becomes less viscous as the temperature rises.

$$\log a_T = \ln \left(\frac{\eta}{\eta_{T_g}} \right) = \frac{-C_1(T - T_g)}{C_2 + (T - T_g)} \tag{2.1}$$

Here a_T is the shift parameter that superimposes various data sets obtained at varying temperatures onto the reference temperature and generates a master curve representing the response function. It is defined as the ratio of the shear viscosity η/η_{T_g} - or since viscosity is a time-dependent variable, is defined as the ratio of relaxation time τ/τ_{T_g}, $(\eta/\eta_{T_g} \sim \tau/\tau_{T_g})$ - at a given temperature to the value at a reference temperature which is usually chosen as a fixed reference temperature, such as the glass transition temperature in the absence of free volume which is a temperature at which the material becomes completely solid and no longer exhibits any viscose behavior. This means that the viscosity of the material would be extremely high and constant in the absence of free volume. It is expressed as:

$$\log a_T = \ln \left(\frac{\tau}{\tau_{T_g}} \right) = -\frac{\dfrac{B}{f_0}(T - T_g)}{\dfrac{f_0}{\alpha_f} + (T - T_g)} \tag{2.2}$$

which is the Doolittle equation [51] and serves as a specific variant of the broader Vogel-Fulcher relation, connecting the dynamic behavior of materials to a single variable, free volume. It is an expression for the change in the logarithm of time as a function of temperature, with f_0, as the fractional free volume of the polymer.

The free volume of a polymer in its glassy state may have only minor changes, and as a result, the coefficient of thermal expansion in the glassy state, α_g is rather

small. The coefficient of thermal expansion is a measure of the change in volume of a material as a function of temperature and is often used to describe the expansion or contraction of a material as it is heated or cooled. Above the glass transition temperature, the free volume of the polymer increases steadily, and as a result, the coefficient of thermal expansion in the rubbery state α_r is higher than the coefficient of thermal expansion in the glassy state. The difference between the coefficient of thermal expansion in the rubbery state and the coefficient of thermal expansion in the glassy state is often referred to as the coefficient of thermal expansion of the free volume α_f.

The experimentally found universal parameters $C_1 = 17.44$ and $C_2 = 51.6$ in equation 2.1 can be converted into an estimate of the free volume at the glass transition, which has a constant value of about 2.5% for all polymers. This equation is a commonly used approximation for flexible polymer chains, which can undergo significant thermal motion over a broad temperature range typically from the T_g to T_g+ 100 C°. The shortest relaxation time for an individual monomer is temperature-dependent. As the temperature rises, the relaxation time of a single monomer changes. therefore all other chain modes within the system synchronize with and mirror these variations. This phenomenon serves as the foundational principle for time-temperature superposition. It's important to note that this equation is only an approximation based on free volume and assumes that it can be determined directly, which is not easy.

In our study, it is important to note that incorporating nanoscale reinforcements can reduce the free volume in polymer nanocomposite systems by limiting the mobility of the polymer chains [52]. This restriction leads to the polymer chains clustering more tightly around the reinforcements, thereby decreasing the free volume within the polymer matrix. Consequently, the segmental dynamics exhibit weak anisotropy due to these constraints. The extent of these variations can be influenced by factors such as the size and shape of both the polymer chains and the reinforcing fillers, as well as the material's temperature and pressure. These factors are examined in detail in this work.

2.1.2 Chain dynamics in polymer melts

The concept of "sub-segmental motions" refers to the vibrational and rotational movements of individual monomer units within the polymer chain. At temperatures above

T_g, the collective effect of these sub-segmental motions evolves into coordinated movements known as "segmental motion". This transition from localized, random movements to more concerted motions involving multiple monomer units along the polymer chain is a key aspect of polymer dynamics. Once in the melt state above Tg, the motion of polymer chains can be effectively described by models such as the Rouse model, which explains how polymer segments move cooperatively based on thermal fluctuations and interactions along the chain. It postulates that polymer chains behave as a series of interconnected beads (representing monomer units) linked by springs (representing covalent bonds) of root mean square size b. The beads experience Brownian motion due to the random collisions with the surrounding molecules. This is a type of random motion that is caused by the thermal fluctuations of the solvent molecules. The springs, on the other hand, represent the elastic tensile forces between the beads. These forces act to restore the polymer chain to its equilibrium configuration when it is stretched or deformed. The hydrodynamic interaction between the segments of a polymer chain refers to how the motion of one segment of the chain can affect the motion of other segments, these interactions are neglected in the Rouse model.

The relaxation time of a polymer chain can be characterized by a mode index. Due to the self-similar nature of polymer chains, Sub-sections of the chain also relax in the same way as the entire polymer chain. If we number these N different subsections with different relaxations with mode index p from one to N, then pth mode relaxation time is $\tau_p \approx \tau_0(N/p)^2$ for the chain with N/p monomers, where τ_0 is the relaxation time of a single bead. The mode index p equal to N representing the shortest relaxation time for one monomer,τ_0, and conversely, p=1 represents the longest relaxation time for the entire polymer chain and is known as the Rouse time, $\tau_R = \tau_0 N^2$. The Rouse time is a measure of the time it takes for a polymer chain to relax to its equilibrium configuration. It is determined by the size of the polymer chain, the number of beads in the chain, the temperature, and the friction coefficient. During this relaxation time, chain sections diffuse a distance of the order of their size R. The time required for this movement is proportional to the diffusion coefficient of the Rouse chain. The friction coefficient of the applied friction force and the diffusion coefficient of the Rouse chain, are related through $D = kT/N\zeta$ and therefore:

$$\tau_R \approx \frac{R^2}{D} \approx \frac{NR^2\zeta}{kT} \qquad (2.3)$$

Thus, for time scales shorter than the Kuhn monomer relaxation time τ_0 the polymer exhibits an elastic-dynamic response which means that when the polymer is subjected to a force, it stretches or deforms elastically and then returns to its original shape once the force is removed. At $\tau_0 < t < \tau_R$ polymer exhibits viscoelastic behavior, and for a period longer than the Rouse time, the polymer is in a viscous state of motion. That is when the polymer is subjected to a force, it flows or deforms viscoelastically and does not return to its original shape once the force is removed.
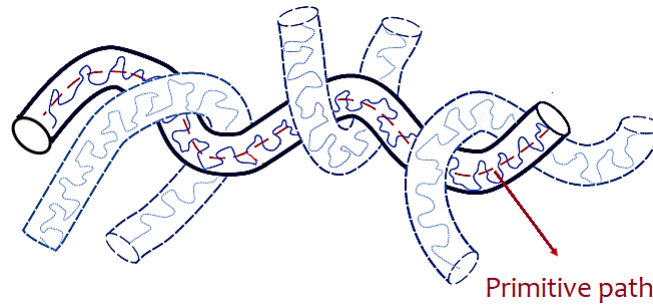

Primitive path

Figure 2.1. Diagram illustrating the Edwards tube concept: It depicts a polymer chain experiencing topological constraints due to surrounding chain entanglements. Adapted from reference [47].

Since chains cannot cross each other in polymers with high molar masses, they create temporary topological constraints called entanglements that restrict the movement of the polymer chains. De Gennes and Edwards explain this restricted motion by a comprehensive model called the **tube model** (Fig 2.1). In this model, polymer chains far above their glass transition temperature show complicated and different dynamics in different time scales. In fact, this tube-like region caused by adjacent polymers acting as barriers limits lateral fluctuations. For chains with modes of shorter length than the entanglement sequence, they do not hit the tube walls and only fluctuate close to their primitive path which is a hypothetical trajectory along the cross-section of the tube, indicating the average positions of the monomers. This means in a time shorter than the entanglement time τ_e, which is the relaxation time

15

of an entanglement strand, the segments are not affected by the obstacles and move freely, which is consistent with the behavior predicted by the Rouse model. The mean square monomer displacement, $\langle[\vec{r}(t) - \vec{r}(0)]^2\rangle$, of the polymer chain at this time has a time dependence of $t^{1/2}$. It should be considered that at a shorter time, the polymer will be in the subsegmental regime, a time scale at which the segments are highly constrained and unable to move freely and exhibit slow, glassy behavior.

On a longer time scale, when the length scale of the motion is bigger than the tube diameter, which defines as the end-to-end distance of an entanglement sequence of N_e monomers, a $\approx$ b $N_e^{1/2}$, polymer chain exceeds certain entanglement molecular weight of M_e, topological constraints feel by the sections of linear chain and restrict the motion and resulting in slower cooperative motion and less displacement, with the slower time dependency of $t^{1/4}$ corresponding to the **constrained-Rouse** regime. At a time longer than Rouse time, the entangled chain diffuses with a worm-like motion along the tube (**reptation**), and all monomers of a linear chain are involved in this coherent motion and finally get out of the tube. The time it takes for a single chain to pass through the entire length of the tube is called the reptation time and eventually, a **free diffusion** is observed after a very long time. So in this kinetic phenomenon, whether a polymer behaves glassy or rubbery it is only a matter of time. As the allotted time increases, more molecular motion occurs and the sample becomes softer.

Therefore, the dynamics of a polymer chain are divided into different motion regimes depending on how the mean square displacement changes as a function of time:

$$
\begin{aligned}
\langle[\vec{r}(t) - \vec{r}(0)]^2\rangle &\approx t^{1/2} & t \lesssim \tau_e & \quad \text{1) free Rouse} \\
&\approx t^{1/4} & \tau_e \lesssim t \lesssim \tau_R & \quad \text{2) Constrained Rouse} \\
&\approx t^{1/2} & \tau_R \lesssim t \lesssim \tau_{rep} & \quad \text{3) Reptation} \\
&\approx t^1 & \tau_{rep} \lesssim t & \quad \text{4) Free diffusion}
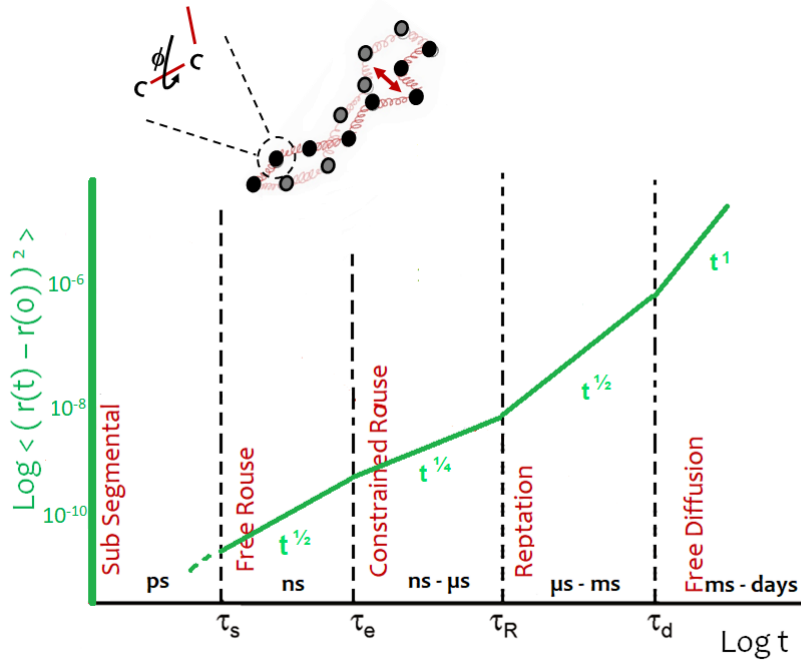\end{aligned}
\tag{2.4}
$$

Figure 2.2. Schematic representation of the dynamic regimes for the mean square monomer displacement, far above T_g. Adapted from [53] with permission from American Chemical Society.

Starting in the glassy state at short times on the picosecond timescale with rapid fluctuation corresponds to the Subsegmental mode which only the vibrational motion or motions within a kuhn segment are detectable. In a slightly longer but still short nanosecond time frame which is described by the Free Rouse model, motion is no longer a rotation about a single bond, but the unentangled segments of the polymer chain which move freely and only being exposed to the effects of chain connectivity.

2.2   Polymer Fillers

Fillers refer to solid additives that are incorporated into the polymer matrix to improve the physical and mechanical properties of the material. They are typically inorganic substances, such as metals, ceramics, or glass fibers. In this combination, inorganic nanofillers provide load-bearing and reinforcing capabilities, while the polymer matrix helps to dissipate energy and absorb impact [54]. Inorganic nanofillers can be classified based on their shape and structure, such as 2D and 3D nanofillers. The choice of nanofiller can depend on the specific performance requirements of the

composite material and the properties of the polymer matrix.

2.2.1 Spherical silica nanoparticles

Three-dimensional nanofillers refer to particles that have nanoscale dimensions in all three spatial directions and are usually spherical. These particles can vary widely in size, and their surface chemistry can be readily modified. This versatility makes them suitable for a variety of applications. Notable nanoparticles such as SiO_2, TiO_2, Ag, and ZnO play crucial roles in the formulation of polymer nanocomposites due to their inherent properties. These properties include good physical stability, a high refractive index, hydrophilicity, UV resistance, excellent transparency, non-toxicity, high photocatalytic activity, and most importantly, affordability [2].
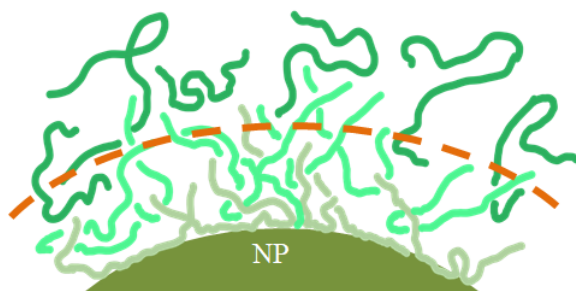

Figure 2.3. The schematic illustrates the interaction between the particle surface and polymer chains, which leads to the formation of an interfacial layer characterized by reduced segmental motion, as indicated by the dashed line.

Our special case is silica nanoparticles. The particle size distribution and surface chemistry of silica particles can be easily modified during their synthesis, or in conjunction with polymerization in a polymeric matrix. Silica is often chosen as a filler material due to its relative chemical inertness, thermal stability, amorphous structure, mechanical strength, and low cost. Additionally, the ease and simplicity of modifying silica's surface chemistry with different chemical groups are highly advantageous, as they can be tailored to suit specific application requirements [55]. Their high chemical stability, due to Si-O bonding, is important for applications such as drug delivery systems. In addition, their excellent biocompatibility and low toxicity, make them attractive for biological applications. Broad applications of silica nanoparticles can also be found in rubber technology, where they are applied to improve the properties

of tires and other rubber products [54, 56–58]

2.2.2 Clays

Clays are the most common examples of 2D nanofillers with a layered structure. Stacking many of these layers together with van der Waals forces leads to clay particles. The inter-layer distance between these layers is called a gallery. Upon adding polymer to this system two different structures can be found: (i) intercalated [45], when the polymer is inserted into a layered structure, extend the inner galleries of the layered clay and confined there, and (ii) exfoliated [59], which is a separation of individual inorganic silicate platelets in the polymer matrix.
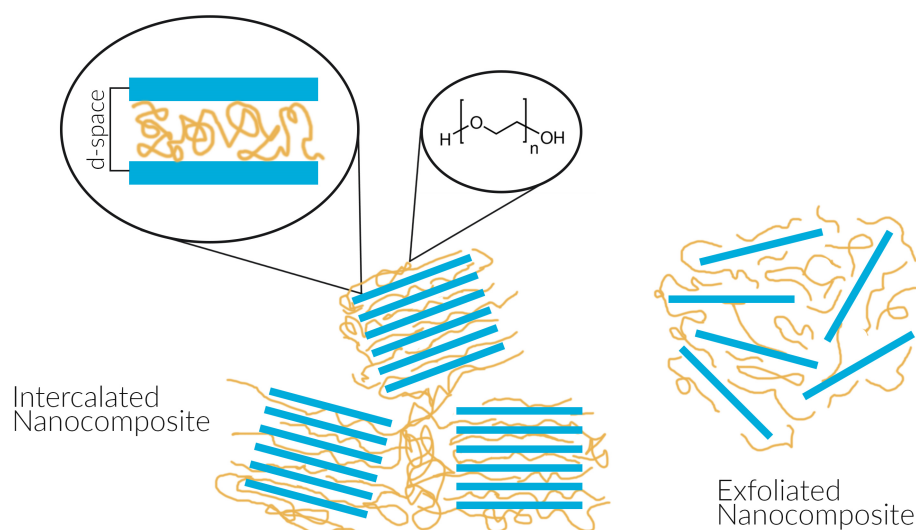
Figure 2.4. Intercalated and exfoliated morphologies.

Clays can be classified in nature based on their surface charge either as cationic, like montmorillonite (MMT), or anionic, like layered double hydroxides (LDH). The most common layered silicates used in nanocomposites are MMT, hectorite, and saponite. The thermodynamically favorable interaction only occurs between clays and hydrophilic polymers like poly (ethylene oxide), which are attracted to water and have a high affinity for polar solvents and have a high degree of polarity and can interact with the charged layers of clays through Coulombic forces, and not with nonpolar polymers [2].

Here we are dealing with sodium fluorohectorite platelets (NHT), one very specific synthetic nacre model as an interesting model system to study polymers under nano-confinement due to the well-defined layered nanocomposite arrangement. Distinguishing this case is its consistent d-spacing between clay sheets even in the presence of intercalated polymer, a characteristic that diverges from common trends where interlayer spacing tends to enlarge with heightened polymer content.

2.3   Model Polymer Nanocomposites

Polymer nanocomposites consisting of nano-sized fillers dispersed in polymer matrices have been at the forefront of polymer research for the past few decades. Significant early developments of these materials led to the expectation that these materials would revolutionize the plastic industry. The introduction of fillers overcomes the limitations of polymer materials by adjusting the thermal and mechanical properties and improving their dynamic, mechanical, electrical, or optical responses [3]. With a global industry worth billions of dollars and ongoing academic and commercial research, PNCs continue to gain attention for their potential to improve material properties. PNCs have demonstrated significant improvements in mechanical properties such as stiffness, modulus, and tensile strength, making them ideal for applications such as rubber products [3, 60].

However, despite their widespread use, understanding the microscopic factors that control their macroscopic properties is still quite a challenge. The properties of PNCs can be manipulated and controlled using various parameters related to size, shape, and surface of nanoparticles or molecular weight, chemistry and architecture of polymers, and concentration, degree of nanoparticle dispersion in the polymer matrix, and the interfacial interactions between the nanoparticles and the polymer matrix. This difference in composition results in PNCs with very different properties than traditional composites or the host matrix [13, 14, 19, 54, 61–65].

2.3.1   Dispersion

Model polymer nanocomposites are often synthesized through various techniques, including melt blending and solution blending. In melt blending, the polymer and nanoparticles are molten together, mixed, and then cooled to form the nanocomposite

material. In solution blending, the polymer and nanoparticles are dissolved in a solvent and then solidified through evaporation [66–68].

The preparation of polymer nanocomposites requires precise control of the dispersion of nanoparticles in the polymer matrix to achieve the desired properties. This is mainly determined by the interactions between the polymer and NPs. To make PNCs, the NPs and polymer are suspended in a common solvent and mixed, then the solvent is evaporated to form the PNCs. The uniform dispersion of NPs in the polymer matrix is influenced by the initial dispersibility of NPs and the solubility of the polymer in the initial solution [24, 69, 70].

The spatial distribution of nanoparticles in polymer nanocomposites is a critical factor in determining the material properties. Even if two systems have the same composition, they can exhibit different properties if developed using different techniques. Poor dispersion and aggregation can occur due to weak interactions between polymers and nanoparticles, which can lead to suboptimal material properties [71, 72]. The choice of casting solvent also significantly influences the dispersion state of nanoparticles. Specifically, it impacts the formation of the interfacial layer, which is believed to be pivotal in determining miscibility and, consequently, the final properties of the material [26, 27, 73]. Durning et al. [74] discovered that silica integrated effectively with poly(methylacrylate). However, adding minor amounts of ethyl acetate led to the agglomeration of nanoparticles. A limited number of research articles have highlighted the non-equilibrium effects observed during the fabrication of PNCs. During the fabrication, external conditions such as shear forces, temperature gradients, or solvent evaporation rates can drive the system away from its equilibrium state. Rapid cooling or solvent evaporation can trap the system in a metastable state. Even if thermodynamically favorable, some configurations may not be achieved due to kinetic restrictions. For instance, nanoparticles might be kinetically trapped in certain regions of the polymer matrix, preventing them from reaching their equilibrium positions [26–28].

Papon et al. studied the mechanical behavior of two sets of reinforced elastomers that differ in their particle arrangement. The two sets consist of the same polymer matrix and fillers coated with the same coupling agent and graft density, but one set has well-dispersed particles while the other includes large aggregates. The study finds that the particle arrangement plays a key role in the mechanical behavior, with the

set of well-separated particles exhibiting weak temperature dependence and little to no strain-softening effect known as the Payne effect, on the other hand, the samples with aggregated particles exhibit a significant dependence on temperature and a large strain-softening effect [71,72]. Therefore particle spacing is also crucial in understanding the mechanical behavior of different filled systems. In rubber nanocomposites, mechanical viscoelastic reinforcement is observed when particles cluster together, creating a network where polymer chains are trapped in tightly packed regions between the particles, while in model nanocomposites, well-dispersed nanoparticles with a high specific surface area maximize their interaction with polymer chains and enable accurate analysis of the desired surface layer surrounding the particles [17, 32, 34, 72, 75]. Small-angle X-ray and neutron scattering are the most appropriate techniques for characterizing the dispersion state of nanoparticles in polymer nanocomposites.

2.3.2   Polymer Conformation at Interfaces

Polymer chains of varying molecular weights exhibit distinct adsorption conformations on the surface of nanoparticles. Depending on the chain length, different conformational arrangements may emerge. Short chains form trains or tails on the surface. Trains are monomer sequences that are adsorbed on the surface of the nanoparticle along their entire path. Long chains, on the other hand, may create dangling chains with one end anchored to the surface and the other end free or generate multiple contacts with the surface to form loops or bridges between particles, particularly at high particle loadings, when their radius of gyration is comparable to the interparticle distance [2, 76–80].
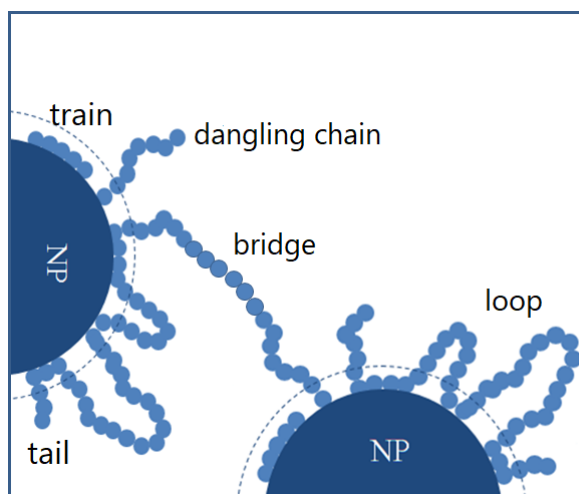
Figure 2.5. Different chain conformation on the particle surface. The dash-line indicates the interfacial layer.

It is worth noting that the conformation of chains adsorbed on the surface greatly affects the properties of the interfacial layer between the polymer and the nanoparticle. Short chains can easily flatten out on the surface and form a more compact layer around the particle. This results in a higher polymer density close to the surface and reduced free volume. On the other hand, high molecular weight chains have less room on the surface and tend to stand. They can only anchor to the surface by a few points per chain, leading to the formation of loops that make the surface inaccessible for other segments. As a result, there will be plenty of unadsorbed chains in the system, leading to larger free volume close to the surface and reduced polymer density [17, 31, 32]. Detailed measurements composed of $PVAc/SiO_2$ and $P2VP/SiO_2$ by Sokolov group [17] showed the effect of molecular weight on the interfacial layer. Surprisingly, the interfacial layer thickness with slowed down segmental relaxation decreased as the molecular weight increased, contrary to theoretical predictions [76–78]. In low molecular weight PNCs, the interfacial layer was more densely packed, causing a significant slowing down of segmental dynamics and a larger layer thickness. However, in high molecular weight PNCs, a competition between the enthalpic effect of surface anchoring and the entropic effect of frustrated chain packing (as a result of the formation of large loops at higher MW) caused unexpected changes in dynamics. In other experiments, a similar molecular weight effect or a weak dependence on MW has been reported [21, 24, 80, 81].

2.3.3   Confinement Effects

The confinement effect in polymer nanocomposites is the impact of nanoparticle size and distribution on the properties of the composite material. Nanofillers in the polymer matrix restrict polymer chain movement, resulting in increased material rigidity and improved mechanical properties such as increased strength and stiffness, as well as improved thermal and electrical conductivity. This effect is relevant at different length scales, at the microscopic scale, the confinement effect is observed in the behavior of individual polymer chains. When nanoparticles act as physical barriers, they confine the polymer chains, reducing their mobility and making it more difficult for them to deform under stress. This leads to an increase in the resistance of the composite material to deformation. while at the macroscopic scale, the confinement effect results in the overall mechanical properties of the composite material, such as its modulus and yield strength [82, 83].

The attraction between hydroxyl groups on silica surfaces and specific groups on polymer chains leads to the physical adsorption of polymers on the surface, creating an interfacial layer around nanoparticles with properties distinct from those of the neat polymer [20, 42, 75, 84, 85]. The introduction of nanoparticles into the polymer matrix is usually thought to create a gradient of properties in this interfacial layer, with increased polymer density and decreased mobility of the chains due to reduced free volume and more anisotropic and restricted motion in this interface region. Only at a sufficient distance from the nanoparticle surface do properties return to those of the bulk polymer. The advanced properties of polymer nanocomposites are closely tied to the dynamics of polymers confined in this nanoscale space [17, 20, 86, 87]. Understanding the structure and features of the filler-polymer interface and the interfacial region that forms due to the attractive interaction between them is critical to optimizing the properties of polymer nanocomposites. The characteristics of polymer adsorption at the interface depend on various factors, including the shape, size, and loading of the filler and the chain length and rigidity of the polymer matrix, but the role of some of these factors is still not well understood. The interface between nanoparticles and the polymer matrix can be divided into two regions: the **bound polymer layer** and the **interfacial layer** [88]. The bound polymer layer, also known as the Guiselin brush [78], is a layer of polymer macromolecules that are adsorbed onto the surface of NPs. This layer is formed due to the attractive forces between the

polymer chains and the surface of the NPs, which result in irreversible adsorption. The height of this layer increases with the molecular weight of the polymer chains and helps to prevent NPs from aggregating at high loading concentrations. The interfacial layer, on the other hand, is a region near the surface of the NPs where the properties of the polymer segments are changed due to restricted molecular mobility. The properties, such as density, segmental relaxation time, mechanical properties, etc., can be tailored and controlled by manipulating the conditions at the interface. This layer is particularly important in nanocomposites because it can play a critical role in determining the overall properties of the composite material [17, 19, 20, 75, 88].
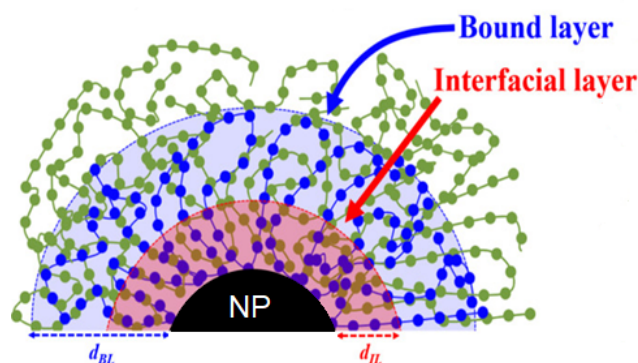

Figure 2.6. Bound layer and interfacial layer. Scheme reproduced from [88] with permission from the American Chemical Society.

These irreversibly adsorbed layers have introduced additional confusion due to the assumption that pictured these immobilized fractions of chains, as "dead layers"; regions with a near-zero expansion coefficient and no molecular mobility [89–91]. However, it is becoming increasingly clear that the structure of these layers is much more complex than previously thought, and the slowdown in the dynamics of this immobilized region can be explained by the dense packing of the polymer material and the formation of a more persistent layering of segments [22, 34, 92, 93]. The increased density at the interface affects the dynamics of the polymer chains, greatly slowing down the polymer dynamics near the particle surface. This slowdown is due to two main factors; the interactions between the polymer and particle, which leads to surface adsorption (the enthalpy effect), and the reduction in the number of conformational transitions at the interface, which results from the lowering of the free

volume required for the system to fluctuate (the entropic term). This means that as we move farther away from the surface, the chains become less restrictive and have more room to move, and the bulk behavior begins to dominate, with the interface effect becoming less evident.

The study conducted by T. Koga and coworkers [92] on Polystyrene film on silica substrates revealed two density regions of adsorbed layers in the direction perpendicular to the surface. According to their explanation, when the polymer chains encounter an initially bare surface, they spread out to maximize their contact with the surface. Therefore this first region, located closer to the substrate, has a higher density and is related to the polymer molecules that arrive first on the surface and are adsorbed with a flat conformation. This region remains nearly identical regardless of the molecular weight of the material. The second region, located further from the substrate, has a density similar to the bulk material and is related to the later arriving chains. These chains find fewer available adsorption spots and will bind with fewer surface segments and adsorbed more loosely. The thickness of this outer region increases as the molecular weight of the material increases. By generalizing the chain conformations of bulks, the author suggests that the change in the probability of polymer local chain conformations is the cause of the observed condensation process. The propagation distance of the chains is found to have also a strong effect on the thickness of the interfacial layer. The greater the propagation distance, the thicker the interfacial layer. However, it is not yet clear at what distance from the surface the chain dynamics continue to be disrupted by the presence of particles [94, 95]. However the transition from the interfacial phase to bulk-like behavior cannot be static or stepwise, but instead is a gradient of distribution. This means that the effect of the interfacial layer on the chain dynamics gradually decreases as the distance from the surface increases, and the bulk behavior becomes dominant again.

Napolitano et al have measured the volume available for structural relaxation at the interface between a thin polymer film and its supporting substrate and emphasized its importance [28, 52]. They discussed a direct correlation between changes in the dynamics of a glassy material and variations in the density of its constituent monomers at the interface. This correlation suggests that faster dynamics modes are related to localized increases in the volume that segments of the material can explore during conformational fluctuations. These localized increases in volume are believed

to manifest in the structural relaxation process, which is the process by which the material becomes less rigid over time. This idea is consistent with the observation that glass transition temperature tends to decrease at higher specific volumes and bigger interchain distances [96,97].

Previous investigations on poly(ethyl acrylate) (PEA) networks adsorbed on silica highlighted a noteworthy temperature reliance on both the immobilized fraction and relaxation parameters [62]. This dependence was later understood through a gradient in effective T_g, indicating a progressive softening upon heating [63,72]. To get further insight into the slowing down of polymer, Papon et al. proposed a new approach to quantitatively describe the dynamics of a polymer chain near a surface and to see if this immobilized fraction is processed as a continuous or as a bi-component layer [63]. They were able to demonstrate that their findings from both NMR and DSC analyses of poly(ethyl acrylate) matrix with monodispersed silica particles were in agreement with a continuous gradient in glass-transition temperature, which was initially observed in the T_g shift depending on the polymer thickness in thin polymer films [98–100]. This means the material that comes into direct contact with the surface exhibits the highest glass-transition temperature within the immobilized layer. However, as the distance from the surface increases, the T_g gradually decreases.

Similar studies were conducted on nano silica/P2VP composites using BDS. Cheng et al. [17] observed a fraction with a slower relaxation mode that appeared to be well-separated, and while Holt et al. [20] employed a bicomponent approach, Baeza et al. [83] considered a continuous broadening of the α-relaxation. In our recent joint study of a similar system [43], we examined two previous approaches to achieve the best description of immobile layer models using NMR and DSC data. The results showed that both the interfacial layer model and T_g gradient model can be successfully applied to fit NMR data. While the interfacial layer model may not be as effective in fitting the heat capacity of the polymer phase in PNCs as the T_g gradient model, it is important to note that the single interfacial component model can still account for anisotropic segmental motions at the interface with the filler. Therefore, both approaches can be seen as complementary in describing the overall physics of this material.

Conversely as observed previously, in a recent NMR study by Golitsyn et al. on poly(ethylene oxide) nanocomposites with spherical silica particles [22], temperature

variations lead to minimal alterations in component ratios and related relaxation parameters in this system. The only slight modifications are attributed to a faster movement in the outer layer which appears mobile, with minimal shifts in the rest of the layer. As a result, the movement range of the "backbone rotation" in the most stationary layer remains consistent, and any potential increase in its related correlation time is indistinguishable. The absence of heat-induced softening implies that PEO/SiO$_2$ lacks a noticeable gradient in its glass transition temperature, distinguishing the PEO/SiO$_2$ nanocomposite from other polymer nanocomposites in analogous scenarios, a contrast that will be further elaborated on subsequently.

In our other joint work on an epoxy-based nanocomposite system [44], we looked closely at how different concentrations of a particular filler (T-LDH) affect the system, especially in terms of molecular movement and the glass transition. Results from the epoxy were compared to the behavior of two glass-forming polymers, PS and PEA. The rigid amorphous fraction (RAF) estimations derived from both calorimetric data and NMR measurements exhibited strong agreement. Despite variations in the Rigid amorphous fraction or the composition of the epoxy mixtures, no significant gradient of T_g was found.

The relative amount of polymer and filler is also an important parameter to consider in PNCs. This is because it affects the interfacial area between the nanoparticles and the polymer matrix. When the NP concentration is high enough, the NPs can aggregate which causes less surface area accessible to the polymer matrix, which results in less disturbance to the segmental dynamics than when the NPs are individually dispersed [72, 101]. When the distance between nanoparticles approaches the size of the polymer chains ($\sim$2Rg), Polymer bridges are formed between nearby NPs [82]. At sufficiently high NP concentrations, where the distance between nanoparticles decreases down to the Kuhn length, the interfacial regions of adjacent NPs overlap and all polymers in the PNC effectively become interfacial. This means that the entire polymer chain is in close contact with multiple NP surfaces [84, 102].

Emamy and co-workers [84] explored the impact of attractively interacting polymer nanocomposites on T_g, using a combination of simulations and experiments. The authors identified multiple length scales that are critical for understanding these effects, such as the average distance between nanoparticles, the scale of dynamics dominated by interfacial effects, and the chain radius of gyration. They observed that the

influence of NPs on T_g is most significant when the interfacial regions of neighboring NPs overlap, but interfacial effects can still be substantial even at greater distances, through chain bridging effects. The authors' experimental findings align with their simulations, indicating that the key parameter to consider is the ratio of the average face-to-face separation between NPs to the chain radius of gyration and that the T_g shifts increase monotonically with decreasing ratio.

The addition of particles to a polymer typically increases the surface area per unit mass of the particles as $1/R$, where R is the characteristic dimension of the isotropic particle which has a favorable effect on the properties of the composite. However, it is important to note that very small particles typically less than 1 to 2 nm in size such as POSS (Polyhedral oligomeric silsesquioxanes) molecules [103], can actually have a plasticizing effect on the polymer matrix and cause the polymer to become more flexible [32]. This strong dependence of interfacial layer thickness on R shows that it is possible to adjust the thickness of these layers by changing the size of the nanoparticles, although systematically studying this dependence and understanding how curvature affects the movement of polymer chains is still a major challenge. It was first reported by Harton et al. [75] using positron annihilation lifetime spectroscopy (PALS) supported by differential scanning calorimetry (DSC) that the adsorbed layer on small nanoparticle (<20 nm) surfaces is significantly thinner (approximately half) than on chemically similar flat substrate surfaces which is in line with the theoretical prediction. Starr et al. [104] utilized coarse-grained MD simulations to investigate the impact of NP size on the segmental relaxations at the interface. They found that the segmental relaxations at the interface of a larger NP are slower than those near a smaller NP. To describe changes in T_g, the relevant parameter was found to be the interparticle distance relative to the polymer radius of gyration, which captures the combined effects of nanoparticle concentration and size and determines the amount of interfacial polymer in the PNC [84].

Kumar and Colby [30] used dielectric relaxation spectroscopy to measure the segmental relaxation of silica hydrophilic nanoparticles in polar P2VP polymer matrices with various silica sizes and concentrations. The results showed that the addition of nanoparticles broadened and slowed down the segmental relaxation. The thickness of the interfacial bound layer was calculated, and the theoretical models suggest that the bound layer thickness may increase with particle size in strongly adsorbing polymer

matrices. The decrease in dielectric intensity was attributed to segments immobilized in the bound layer. The relationship between the bound layer thickness and particle size suggests a possibility of tuning the bound layer thickness by changing the size of the nanoparticles.

Kumar et al. [29] conducted a study on the thickness of the bound polymer layer using various methods. The results obtained from TGA gave an estimate of the bound layer thickness, which was found to be lower than those obtained from DLS and TEM. However, all three methods consistently showed that the thickness of the bound layer increases with an increase in NP size. These findings led the authors to conclude that the effects of NP surfaces on polymer properties propagate to much larger distances than previously assumed. Sokolov's group [21] utilized several techniques, including temperature-modulated differential scanning calorimetry (TMDSC), BDS, and dielectric relaxation spectra to investigate the interfacial dynamics and structure of P2VP/silica nanocomposites and matrix-free P2VP grafted from silica nanoparticles. The study found that the degree of stretching of the polymer chains at the interface, influenced by chain crowding and steric hindrances at the NP surface, plays a more significant role in the suppression of segmental dynamics than whether the chain is physically adsorbed or covalently bonded to the NP. They also point out the essential role of NP curvature in this effect, where larger nanoparticles or flat surfaces are expected to exhibit more significant changes. These findings are consistent with predictions for the dynamics of polymer systems with anisotropic compositions [105].

Despite significant research efforts, a thorough comprehension of how the size and curvature of NPs affect the segmental dynamics in PNCs remains elusive, particularly in experimental contexts. Therefore, our study aims to investigate the complexities of polymer nanocomposites, with a focus on the amount of polymer adsorbed to the surface and the influence of this interfacial layer on PNC properties. Thus, conducting a systematic study that varies NP size and concentration or chain size, may be pivotal. Our chosen methodology involves utilizing nuclear magnetic resonance (NMR) techniques.

We employ static ^{1}H NMR techniques to determine absolute values for the fractions of immobilized and mobile polymer chains across varying overall mobility. This includes analyzing on-resonance ^{1}H low-field free-induction decay, occasionally supplemented with Hahn-echo or Carr-Purcell-Meiboom-Gill decay data. Additionally,

high-resolution ^{1}H and ^{13}C magic angle spinning spectra are necessary to identify chemical components and provide insights into chain behavior, configurations, and compositions. The dynamic nature of polymers influenced by nanoparticles within the narrow interfacial region, spanning only a few nanometers, presents significant challenges. To address these challenges, we utilize advanced NMR techniques. The ^{13}C T_1 relaxation time is a valuable parameter for understanding molecular dynamics. However, due to the low natural abundance of ^{13}C, there is minimal homonuclear coupling, leading to prolonged ^{13}C T_1 relaxation times. In such dilute spin systems, this extended ^{13}C T_1, coupled with a low signal-to-noise ratio, makes saturation recovery sequences impractical for T_1 measurement. Torchia's pulse sequence addresses this by transferring polarization from protons to carbons, enhancing the signal-to-noise ratio while allowing the use of a shorter ^{1}H recycle delay for efficient ^{13}C T_1 measurement.

The transverse magnetization, generated by a $\pi/2$ pulse, can be stabilized along a specific axis within the rotating frame by applying a continuous radio frequency field, known as a spin-locking pulse. In a $T_{1\rho}$ experiment, varying the strength and duration of the spin-lock pulse is crucial, as it determines the extent to which the transverse magnetization is decoupled from free precessional decay. The decay of magnetization along this locked axis then occurs with a time constant $T_{1\rho}$. This technique is particularly useful for investigating slow molecular dynamics.

The Free Induction Decay method indeed provides insights into the lower Rouse modes, characterized by larger-scale motions of the entire polymer chain, including overall chain diffusion and cooperative motions. Conversely, transitioning to ^{13}C relaxation measurements enables the exploration of higher Rouse modes, which involve more localized vibrations of segments of the polymer chain. These techniques allow us to quantitatively explore dynamic processes occurring across various timescales, which will be discussed further in the subsequent chapter.

NMR Basics and Principles

The basic theory of NMR spectroscopy in the following chapter is mainly based on the books of Harald Gunther [106], Malcolm H. Levitt [38] and James Keeler [107].

3.1   Key Concepts in NMR

Nuclear Magnetic Resonance (NMR), rooted in the atomic nucleus's interaction with magnetic fields, began with Wolfgang Pauli's spin concept in the 1920s. Isidor Isaac Rabi initiated NMR experiments in the late 1930s, evolving into solid-state demonstrations post-World War II by Felix Bloch and Edward M. Purcell. Key milestones, from Stern's spin proof to Ernst's 2D NMR breakthrough, enriched the field. Innovations like Dynamic Nuclear Polarization and Magic Angle Spinning, coupled with superconducting magnets and Fourier transform adoption, bolstered sensitivity and resolution. Today, NMR spectroscopy is vital in unraveling molecular structures in chemistry, offering insights into chemical structures and polymer chain dynamics.

The atomic nuclei at the center of the electron cloud, made up of protons and neutrons, act like small magnets with a magnetic moment. The concept of angular momentum is used in physics to describe rotational motion. However, when it comes to the motion of atomic nuclei, traditional mechanics is not enough to explain it. This is where quantum mechanics comes into play. In quantum mechanics, quantities can only take specific, discreet values and cannot vary continuously. The angular momentum of the nuclei is given by $\hbar\sqrt{I(I+1)}$, where I is the nuclear spin quantum number and it can only take certain values, such as 0, 1/2, 1, 3/2, and so on.

Among the various nuclei of atoms, about one hundred isotopes exhibit a property known as spin, which is a form of intrinsic angular momentum. To be observable by NMR, the isotope must have a non-zero spin value in its ground state, the lowest energy state of the nucleus. Isotopes with an odd mass number, such as ^{13}C, have half-integer spin values. In contrast, isotopes with an even mass number but an odd

atomic number, such as deuterium, have integer spins (e.g., spin 1). For instance, ^{12}C, the most abundant isotope of carbon, has a spin value of 0 and cannot be observed by NMR. In contrast, ^{13}C, which has a spin of 1/2, is observable by NMR despite its low natural abundance of 1.1%. Natural abundance refers to the mole fraction of an isotope as it occurs in nature; higher natural abundance leads to stronger NMR signals, which is why proton NMR is more sensitive than ^{13}C NMR. Another crucial property for NMR is the gyromagnetic ratio, a constant that relates the magnetic moment of a nucleus to its spin. A higher gyromagnetic ratio corresponds to a greater magnetic moment, resulting in a stronger NMR signal.

The magnetic dipole moment of an atomic nucleus can adopt any orientation in the absence of a magnetic field, but in the presence of a stationary magnetic field, B_0, the nucleus tends to align either parallel or antiparallel to the field. To be precise, the Zeeman effect is the result of the interaction between the magnetic dipole moment of the nucleus and an external magnetic field, which results in the splitting of the energy levels. Our focus here is on spin 1/2 nuclei, which have two Zeeman eigenstates: the α and β states, where the magnetic moment is parallel and antiparallel to the field, with quantum numbers of +1/2 and −1/2, respectively.

According to Boltzmann statistics, the α state, which has lower energy compared to the β state, is more populated by spins, leading to a macroscopic longitudinal magnetization (net magnetic moment, M) aligned with the direction of B_0, along the z-axis. In the presence of the static magnetic field, spins naturally precess around the direction of B_0 at a specific frequency known as the Larmor frequency, $\omega_0 = -\gamma B_0$, where γ is the gyromagnetic ratio. The role of the radio frequency (rf) pulse is to temporarily disturb this equilibrium by tipping the net magnetization away from the z-axis, causing the macroscopic magnetization to precess in the transverse plane (xy-plane) around the B_0 field. This transition only happens if the energy of the photon matches the difference in energy between the two levels. The flip angle is determined by the nutation frequency ω_{nut}, which is directly proportional to the intensity and duration of the applied rf field. The Larmor frequency differs between isotopes. The ^{13}C nucleus has a gyromagnetic ratio that is 4 times lower than the proton, so its Larmor frequency is about 100.6 MHz in a field of 9.4 T, while that of the proton is about 400 MHz.

3.2   Spin Interactions

The behavior of nuclear spins is influenced by the presence of electrons and other nuclei in the sample. The Schrödinger equation describes the motion and interactions of all particles in the system, including electrons and nuclei. The following time-dependent Schrödinger equation neglects the contributions of electrons and focuses only on the nuclear spin states. The wave function, $|\psi(t)\rangle$ represents the quantum state of the nuclei's spin system, and $\hat{H}$ denotes the nuclear spin Hamiltonian operator:

$$\frac{\partial}{\partial t}|\psi(t)\rangle = -i\hat{H}|\psi(t)\rangle \qquad (3.1)$$

However, wave functions and the Schrödinger equation are rarely used in the field of magnetic resonance. This is because a statistical average over a very large number of spins is usually considered. Individual states are described here by the density matrix, and their time evolution is governed by the Liouville-von Neumann equation.

NMR probes the structure and dynamics of samples by analyzing internal interactions' impact on energy levels and transition frequencies. In instances where molecules or their components are in motion, these internal interactions undergo modulation, often resulting in diminished intensities compared to static scenarios. Furthermore, this fluctuation leads to a shortening of the lifetime of certain states of the spin system, in other words, relaxation. These interactions involve the electron shell, neighboring spins, and external fields, influencing parameters like chemical shift. While nuclear quadrupole moments are irrelevant here, detailed exploration of magnetic interactions with neighboring spins is covered in section 3.3.2.

3.2.1   Chemical shift and its anisotropy

Chemical shift is a phenomenon in NMR spectroscopy that refers to the change in the resonance frequency of a nucleus in a molecule compared to a reference frequency, which is due to the influence of the local electronic and molecular environment. This change is calculated as the ratio of the difference between the resonance frequency, ω_0, of a nucleus in a molecule and a reference frequency, ω_{ref}, to the reference frequency:

$$\delta = \frac{\Omega_0}{\omega_{ref}} = \frac{\omega_0 - \omega_{ref}}{\omega_{ref}} \qquad\qquad (3.2)$$

It is typically reported in parts per million (ppm) and provides important information about the chemical composition and structure of molecules, as well as their interactions with other molecules. It is caused by the electron cloud surrounding the nucleus. The electron cloud induces small magnetic fields that can either align or oppose the applied magnetic field, resulting in the nucleus experiencing an effective magnetic field that is slightly different from the externally applied field. In general, the shielding effect depends on the orientation of the electronic environment concerning the external magnetic field. This implies that different molecular orientations typically result in various transition frequencies. This phenomenon is known as chemical shift anisotropy. The physical origin of chemical shift is based on a complex quantum mechanical interaction between the electron cloud and the applied magnetic field and is not discussed here.

3.2.2   Dipole–dipole couplings

Another anisotropic interaction that is important in solids is dipolar coupling which is a direct interaction between the magnetic moments of the two neighboring nuclei. The magnitude of this interaction is given by the dipole–dipole coupling constant, $D = -\frac{\mu_0}{4\pi}\frac{\gamma_j\gamma_k\hbar}{r_{jk}^3}$, where μ_0 is the magnetic constant and γ_j and γ_k is the gyromagnetic ratios of the spins j and k, therefore gyromagnetic ratio also plays a role, the larger the gyromagnetic ratio means the larger the magnetic moment.

In an isolated spin pair, the orientation dependence of dipole-dipole coupling is described by the second Legendre polynomial $P_2(\cos\theta) = 1/2(3\cos^2(\theta) - 1)$, where θ signifies the orientation dependence of the dipole-dipole coupling of an isolated spin pair and is the angle between the inter-spin vector and the magnetic field. Coupling only between theses two spin pare with two possible spin state leads to a dublet in spectra, but in solids the dipole–dipole couplings involve many spin pairs with all possible orientations, leading to 'homogeneous' line broadening, with Gaussian shape spectra. The restricted motion of molecules in crystalline structures allows the dipolar coupling between spins to reach its maximum value. However, in isotropic liquids,

molecules are tumbling fast and have all the possible orientations with respect to the magnetic field, thus averaging the anisotropy and canceling it out and showing a sharp peak at the isotropic chemical shift.

In scenarios where polymers are heated well above their glass transition temperature or beyond their melting point, the molecular dynamics become intensified, resembling a soft solid. In elastomers with permanent cross-links, high molecular weight polymer melts with entanglements, or, as in the context of our study, polymer nanocomposites influenced by fillers and restricted motion due to motion anisotropy, the dipolar interaction is not fully averaged out, and a small residual term, remains.

3.3   Relaxation and Dynamics

Relaxation in NMR spectroscopy refers to the process by which the spin system returns to equilibrium after the application of a perturbation. Equilibrium in this context means that the populations of the spin states in the system are following a Boltzmann distribution, where higher energy levels are correspondingly less populated, and all non-diagonal elements of the density matrix are zero. At equilibrium, the magnetization vector, M, lies along the z-axis, and there are no coherences present, no time dependency, and notably, no transverse magnetization that can be detected. The return of the spin system to equilibrium after the elimination of the perturbation is characterized by longitudinal or spin-lattice relaxation (T_1). From a classical standpoint, this corresponds to the recovery of the z-component of the magnetization. In quantum mechanical images, it relates to the return of the diagonal elements. The longitudinal relaxation corresponds to the re-establishment of the populations to their equilibrium level, or in the vector picture, the return of the magnetization vector along the z-axis, and the transverse relaxation or spin-spin relaxation (T_2) corresponds to the loss of phase coherence,i.e. the non-diagonal elements.

Applying a 90° rf pulse results classically in the magnetization being flipped from the z-axis to the x-axis, causing transverse magnetization to emerge in the x-y plane. After the rf pulse is withdrawn, the spins continue to precess around the z-axis of the external magnetic field at Larmor frequency, and the magnetization can be represented as a superposition state. In the classic Bloch or vector framework description of NMR, these relaxation phenomena can be introduced as additional exponential terms on top of the precession of magnetization:

$$M_x = Mcos(\omega_0 t)\exp(-t/T_2) \tag{3.3}$$

$$M_y = -Msin(\omega_0 t)\exp(-t/T_2) \tag{3.4}$$

When the observer rotates with the same frequency as the Larmor frequency, we are in the rotating frame which removes the oscillating term from the equation and simplifies the time dependency of the transverse magnetization. By using the rotating frame, the transverse magnetization appears static with the equation:

$$M_x = M\exp(-t/T_2) \tag{3.5}$$

and the return of z magnetization to equilibrium with:

$$M_z = M(1 - \exp(-t/T_1)) \tag{3.6}$$

The practical relevance of relaxation lies in the fact that it determines factors that are important for the NMR experiment. In this way, the length of the required recycle delay between acquisitions of the same experiment is determined by the T_1 relaxation time. In order to acquire accurate data, a sufficient amount of time needs to be allowed between two acquisitions of the same experiment, to ensure that the magnetization has relaxed sufficiently toward equilibrium. The T_2 relaxation time of the transverse magnetization determines the linewidth of the resonance peaks in the NMR spectrum. The full width at half maximum of an NMR signal corresponds to the transverse relaxation rate constant, $R_2 = \pi/T_2$. Therefore, the faster the spins relax in the transverse plane, the broader the resonance lines will be.

T_1 relaxation is caused by interactions between the spins and their surroundings, such as dipole-dipole or quadrupole coupling or chemical shift anisotropy, as well as molecular motion, such as changes in orientation or rotation either of a molecule entirely or locally in specific regions. These interactions cause energy to be transferred from the spin system to the surroundings, which leads to a change in the net magnetization along the longitudinal axis. The rates of both T_1 and T_2 relaxations

are connected to the correlation function $G(\tau)$, which describes the loss of coherence between the random local field values, B_x, at different times as the time delay τ is extended:

$$G(\tau) = \langle B_x(t) B_x(t + \tau) \rangle \tag{3.7}$$

For very short time intervals, the system will not have evolved much from its initial state, which means the random field will not have changed very much and is still pretty close to its original value, and consequently, the correlation is high. But for longer time intervals, the system has rearranged itself more and more, and there will be less and less correlation with its initial value. As a result, $G(\tau)$ decays to zero for an isotropic motion as τ increases. To describe the T_1 process, can assume a simple functional form that is often used for correlation functions, which is just an exponential decay, starting from a given value at time zero, or at a time interval τ.

$$G(\tau) = \langle B_x^2(t) \rangle \exp(-\frac{\tau}{\tau_c}) \tag{3.8}$$

This exponential decay is characterized by a time constant, the so-called correlation time, τ_c. The correlation time is the time at which the correlation function has decayed to a factor of $1/e$ of its initial value. If we consider the random rotation of a molecule, in this case, for such a random process, the correlation time corresponds approximately to the time it takes the molecule to rotate by one radian. The Fourier transform of the correlation function including a factor of 2 yields the spectral density. For a simple exponential correlation function, as mentioned above, the spectral density is a Lorentzian:

$$J(\omega) = 2\langle B_x^2(t) \rangle \frac{\tau_c}{1 + \omega_0^2 \tau_c^2} \tag{3.9}$$

The spectral density function is a measure of the "amount of motion" that the atomic nuclei experience at the given frequency due to their dynamic surroundings. The more the nuclei move, the broader the spectral density function becomes. Thus, the spectral density function of a system varies with different correlation times. For systems with long correlation times corresponding to slow motion as for rigid solids, where the random field that spin experiences does not change quickly, the resulting

spectral density function will be narrow as seen in the green curve in Figure 3.1a. Here more intensive motion is present at low frequencies and less intensive motion is present at higher frequencies. In the rigid lattice limit which is a very important region in solid-state NMR, when $\omega_0 \tau_c \gg 1$, the spectral density function is proportional to $1/\tau_c$. On the other hand, if τ_c gets shorter which implies fast motion, such as solutions, the spectral density function will be broader and will move out to higher frequencies, as seen in the orange curve in Figure 3.1a, therefore there will be less intensive motion present at low frequencies and correspondingly more intensive motion present at higher frequencies. In the extreme narrowing regime, when $\omega_0 \tau_c \ll 1$, the spectral density function is approximately $2\tau_c$.

The spin-lattice relaxation time, T_1, is inversely proportional to the $J(\omega_0)$, spectral density at the Larmor frequency, $T_1^{-1} = \gamma^2 \langle B_x^2(t) \rangle J(\omega_0)$ (according to the Bloembergen-Purcell-Pound relaxation theory). This means that relaxation depends on how much motion is present in the random process at the Larmor frequency. Therefore, if we plot the spin-lattice relaxation time constant as a function of correlation time for random field fluctuations, we will obtain the curve shown in Figure 3.1b. The relaxation time will have a minimum when the correlation time of the motion corresponds to the inverse of the Larmor frequency. Since temperature affects the molecular motion and increasing temperature brings more motion to the system and leads to shorter correlation times, the effect of temperature on the spin-lattice relaxation time depends on which side of the minimum the system is located.
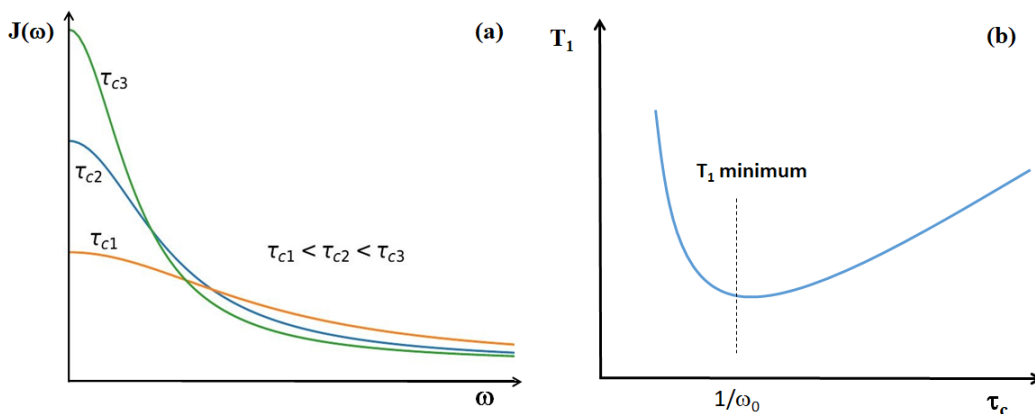

Figure 3.1. (a) spectral density as a function of frequency (b) The spin-lattice relaxation time constant as a function of correlation time. Adapted from [107].

3.4 ^{1}H NMR experiments

3.4.1   Free Induction Decay (FID)

NMR spectroscopy employs the use of radiofrequency pulses to manipulate the alignment of atomic nuclei in a magnetic field. A basic NMR pulse sequence is a 90° rf pulse tuned to the resonance conditions in a given magnetic field. This pulse flips the magnetization vector from the z-direction, along the main magnetic field, to the transverse x-y plane. The flip angle of the pulse depends on the nutation frequency, which is proportional to the applied rf field strength and the pulse duration. The brief interval between the end of a strong RF pulse and the initiation of the detection of transverse magnetization is known as the dead time. The magnetization vector then begins to precess around the main magnetic field at the Larmor frequency. The rotating magnetization creates a time-varying magnetic field, which induces an alternating current voltage in the coil surrounding the sample. This voltage is proportional to the magnetization and can be recorded as a function of acquisition time, producing a Free Induction Decay (FID) signal. The FID signal is the sum of many cosine waves, the intensity of which decays exponentially. The intensity of the FID signal in the time domain directly corresponds to the total number of protons in the sample. When the FID is transformed to the frequency domain to generate the NMR spectrum, each peak's integral reveals the number of protons resonating at that specific frequency. Peak integration allows us to estimate the number of protons contributing to a peak, therefore the peak caused by a methyl group has three times the area of the peak caused by a single proton in the same spectrum.
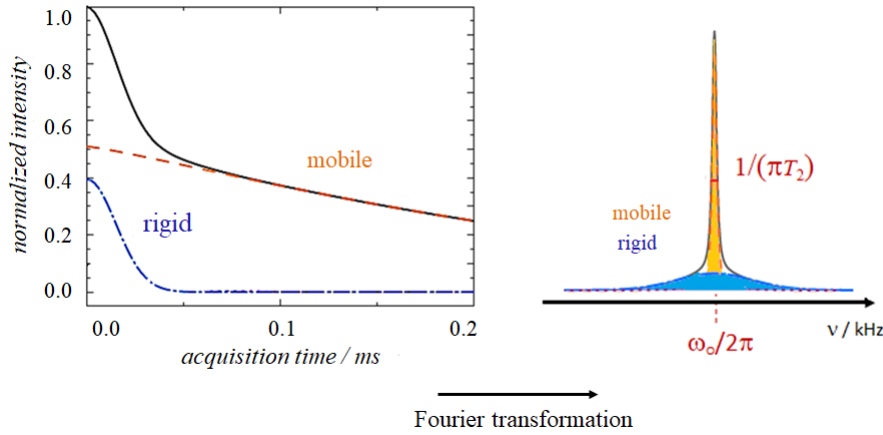
Figure 3.2. The free induction decay signal in the time domain is shown as a solid gray line, with its two distinct components: an amorphous phase (dashed orange line) and a rigid phase (blue dash-dotted line). In the frequency domain, analysis becomes more complex due to the overlap of signals from all phases.

Indeed, dipolar couplings between protons offer a valuable means to quantify the phase composition in polymers, utilizing the heterogeneity of molecular mobility. However, deconvolving the signal to distinguish the contributions of each phase becomes challenging due to the broad and overlapping peaks in the frequency domain [36]. FID analysis can be employed to determine the molar fractions of distinct phases within a multi-phase system, such as a semicrystalline polymer comprising both rigid and mobile phases. The amorphous and rigid regions of a semicrystalline polymer exhibit differing dipole-dipole couplings, resulting in varying transverse relaxation times, T_2 based on the mobility of each region. When the dipole-dipole coupling is high, leads to a significant dephasing effect, thereby reducing T_2 values. Conversely, regions with higher mobility and lower residual dipolar couplings exhibit longer T_2 values. Figure 3.2 illustrates the FID and provides insights into the contributions of the mobile, and rigid fractions.

In a system characterized by such dynamic inhomogeneity, the FID signal is fitted to a combination of stretched or compressed exponential functions. The following equation is utilized to analyze the detected FID [36]:

$$I_{FID} = f_r \cdot e^{-\left(\frac{t}{T_{2r}}\right)^{\beta_r}} + f_i \cdot e^{-\left(\frac{t}{T_{2i}}\right)^{\beta_i}} + (1 - f_r - f_i) \cdot e^{-\left(\frac{t}{T_{2m}}\right)^{\beta_m}} \tag{3.10}$$

Here, f and T_2 represent the fraction and transverse relaxation time of each component, while β is a shape parameter that characterizes the signal decay. The subscripts

41

r, i, and m correspond to rigid, intermediate, and mobile fractions, respectively. At short timescales, the FID signal is dominated by quasi-rigid phases with strong dipolar coupling and some fast, strongly anisotropic mobility will show fast decay, T_{2r} on the time scale of microseconds with a Gaussian shape parameter, $\beta = 2$. This is associated with the more immobilized regions of the polymer, where the chains are more tightly packed and have less mobility. The calculation of M_2 the second moment of the dipolar frequency distribution, which quantifies the dipolar coupling within the crystalline phase, can be derived by $M_2 = 2/T_{2r}^{-2}$. Intermediate phases with residual dipolar couplings arising from increased chain motion at longer timescales, and mobile phases with fast segmental motions will average out the dipolar couplings, resulting in a rather long T_2 in the range of milliseconds to seconds and their decay shapes described by a compressed ($\beta > 1$) or stretched ($\beta < 1$) exponential function. This is typically associated with the more amorphous regions of the polymer.

The principles outlined above have been applied in both of our investigations of Clay/PEO and SiO_2/PEO nanocomposite systems. The analysis of the FID signal properties allowed us to determine the fraction of the polymer chains that become immobilized or experience decreased mobility as a result of adsorption onto the filler surfaces.

3.4.2   Saturation recovery

To determine the longitudinal relaxation time T_1, the Saturation Recovery method is used. The process involves the use of two 90° pulses and a waiting time to observe the build-up of longitudinal magnetization. The first 90° pulse generates transverse magnetization and sets the longitudinal magnetization to zero.
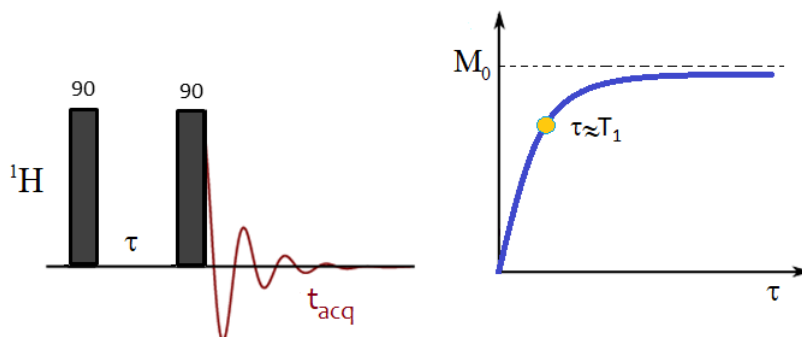

Figure 3.3. The saturation recovery pulse sequence.

After a waiting period, the longitudinal magnetization starts to build up with a characteristic relaxation time T_1. The second 90° pulse is then used to detect this longitudinal magnetization by rotating it into the transverse plane. This sequence is repeated at multiple time points to create an intensity build-up curve. To reach equilibrium after a perturbation, such as a radio-frequency pulse, the spin system needs a minimum of five times T_1. This period, also known as the recycle delay, determines the waiting time between subsequent scans. The Saturation Recovery experiment is crucial in NMR spectroscopy and is used to determine the necessary recycle delay.

3.4.3   Echoes and refocusing

In NMR spectroscopy, echo sequences are a group of pulse sequences that are specifically designed to extract detailed information about the molecular structure and dynamics of a sample. These sequences reverse dephasing, which is particularly valuable in solid-state NMR where signals often broaden due to frequency dispersions. **The magic sandwich echo sequence (MSE)** is one such echo sequence that is particularly useful when homogeneous line broadening occurs in solids due to multiple homonuclear dipolar couplings. By utilizing echo generation, it becomes possible to record the NMR signal at zero time, thereby overcoming the constraints imposed by the finite duration of pulses and the dead time, which inhibits immediate signal recording after the application of a pulse. MSE also exhibits signal loss that is variable due to imperfections in the echo pulse sequence the intensity of dipole coupling and the fact that the pulses have finite duration even if they are adjusted exactly. This unique property makes it a valuable tool for the study of molecular dynamics within intermediate timescales ranging from tens to hundreds of microseconds [44]. The decay of the echo amplitude is used to probe the timescale of molecular motions. The success of dephasing reduction relies on the preservation of coherence throughout the pulse sequence. Thermal motion progressively erodes these coherences. As the length of the pulse sequence increases, the echo amplitude will decay with a relaxation time T_2 which is a measure of how quickly the coherence between nuclear spins in a molecule decays due to molecular motions [41, 108]. It should be noted that the success of this depends on coherence being maintained throughout the entire pulse sequence. Thermal motion increasingly destroys this coherence. The MSE pulse se-

quence begin with a 90° pulse followed by a delay of τ and a "sandwich" section of 4τ duration containing two 90° pulses of the same phase and two sets of four 90° pulses in between. The MSE sequence refocuses the rapidly decaying NMR signals by reversing dipolar dephasing, which eliminates line broadening and improves the resolution of the NMR spectrum [108, 109].
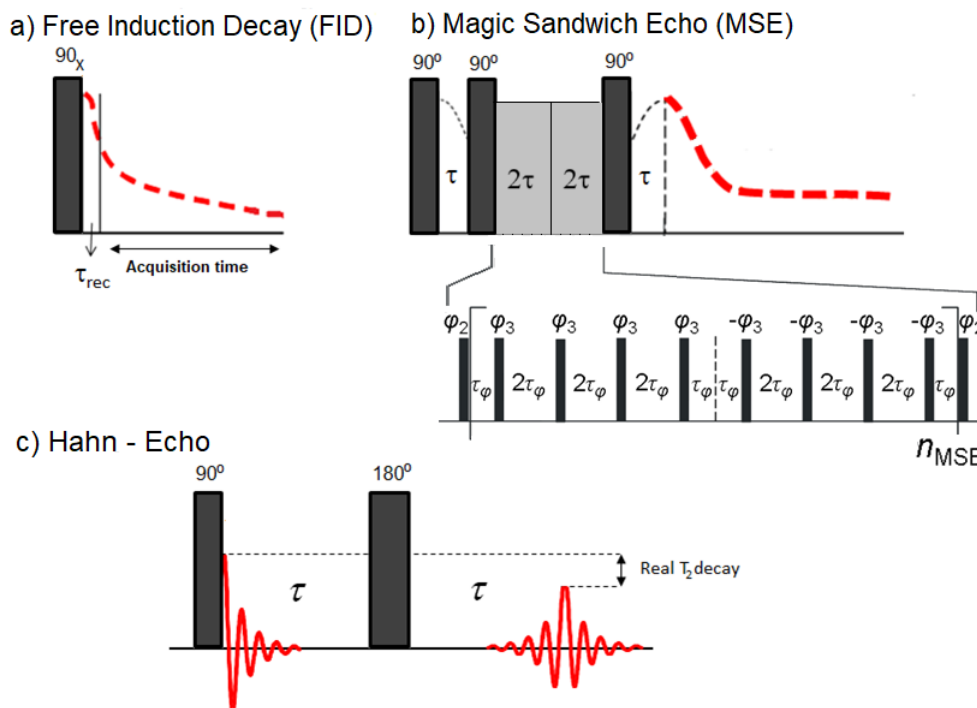

Figure 3.4. Schematic plot of a) FID b) MSE and c) Hahn echo pulse sequences. MSE pulse started with a 90° pulse followed by a delay of τ and a 4τ duration "sandwich" section, which includes two 90° pulses of the same phase and two sets of four 90° pulses in between. The waiting time τ in the MSE sequence is calculated as $\tau = (2\tau p_{90} + 4\tau_\phi)n_{MSE}$, with τp_{90}, τ_ϕ and n_{MSE} being the 90° pulse length, the phase-switching time and the number of MSE cycles, respectively. Adapted from [36].

The **Hahn echo sequence** uses a 180° pulse, also known as a refocusing pulse, to refocus the dephasing caused by chemical shift anisotropy or heteronuclear dipole-dipole couplings ($P_x^{\pi/2} - \tau - P_x^{\pi} - \tau$) [110, 111]. The 180° pulse reverses the effects of the offset that occurred during the first delay τ by refocusing during the second delay. The delay between the $\pi/2$ and the π pulses determines the time at which the echo reaches its maximum value. On the other hand, the **Carr-Purcell-Meiboom-Gill (CPMG)** pulse sequence is an extension of the Hahn echo sequence. It utilizes a

train of π pulses, separated by short intervals, instead of a single π pulse. This train of refocusing pulses helps to further refocus the dephased magnetization and enhance the echo signal. The multiple refocusing pulses in the CPMG sequence minimize the impact of external magnetic field inhomogeneities and improve the measurement of T_2 relaxation time [112, 113].

Where the initial fast decay of the FID data characterizing the rigid components is extended by CPMG or Hahn echo decay to effectively assess the much slower large-scale motions encoded in the relatively long T_2 of the mobile phase, we used the global fit of Origin to fit this full decay. Global Fitting commonly refers to the process of simultaneously fitting curves to multiple datasets using a single model. Optionally, fit parameters can be shared between datasets. For shared (global) parameters, a single best-fit value is determined from all fitted datasets. For non-shared (local) parameters, a unique best-fit value is generated for each individual fitted dataset. We assumed that the shape of the relaxation components of these experiments was the same but their amplitudes were different, Consequently, we shared the beta values while independently fitting the amplitudes of the components which is used in section 5.4.

3.5   Magic-angle spinning

Magic-angle spinning (MAS) is a widely used technique to improve the resolution of NMR spectra of solids and is often used to eliminate the effects of anisotropic inter-actions, by averaging out the interactions over different orientations of the molecule. By mechanically rotating the sample around an axis tilted by 54.7°, referred to as the magic angle, with respect to the B_0 field, the angular-dependent part of the interactions, $(3cos^2(\theta) - 1)$, becomes zero, and the broadening effect caused by anisotropic interactions is eliminated.

More precisely, when the sample is spinning at the magic angle, the CSA powder line shape splits into many peaks, called sidebands, which remain narrow, even under very low MAS frequency. The difference in frequency between two nearby sidebands is the MAS frequency, and with fast enough spinning mainly the isotropic line will be observed. This increase in resolution allows for the detection of weak signals and the identification of small chemical shifts. However, the MAS effect is slightly different in systems that experience homonuclear dipolar couplings. These interactions, which

are caused by the magnetic dipole-dipole interaction between nuclei of the same type, here MAS frequency should be much larger than the strength of the dipolar interaction to observe a narrow isotropic line.
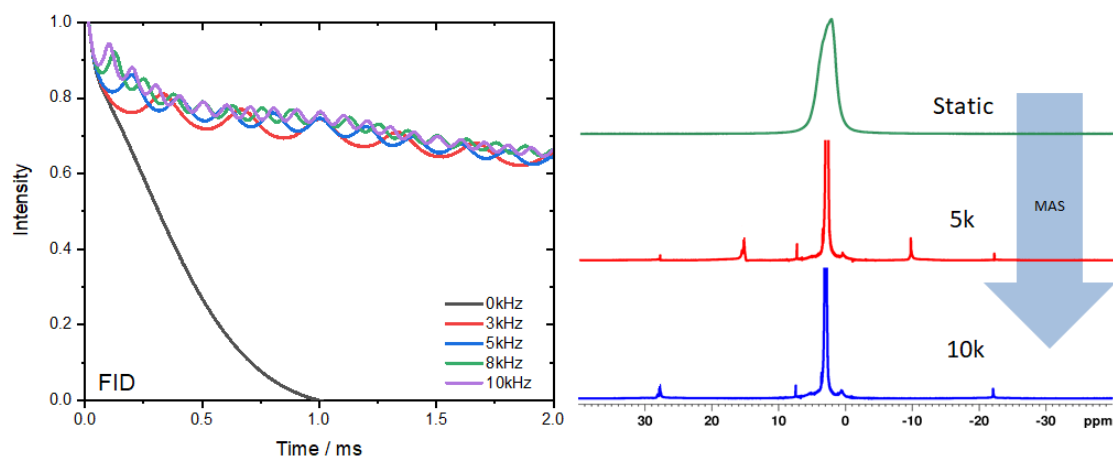

Figure 3.5. Evolution of Free Induction Decay with increasing spinning speeds of Magic-Angle Spinning on E(PEO3K-40nm-0.5). Analyzing the decay patterns reveals a significant increase in the T_2 relaxation time which indicates a substantial influence of the MAS spinning speed on the characteristics and duration of the observed transverse relaxation.

However, this spinning motion introduces a challenge when acquiring and analyzing NMR time domain signals because the signal is modulated periodically due to the rotation. By synchronizing the acquisition with the spinning cycle, the NMR signals are captured at the same phase every time (on the top of rotor echoes). By ensuring that the rotor period, which is the time it takes for the sample to complete one full rotation, is an integer multiple of the rf pulse period. This is achieved by adjusting the spinning frequency and rf pulse timing so that they are in exact synchrony, effectively averaging out the spinning sidebands over multiple rotations.

The efficiency of MAS in averaging out anisotropic interactions is closely linked to the spinning speed. Generally, as the spinning speed increases, the effectiveness of averaging out interactions like chemical shift anisotropy and dipolar interactions improves. This means that at higher spinning speeds, one can expect to see longer T_2 relaxation times due to reduced contributions from these interactions. In Figure 3.5, we observe the evolution of the FID profile as a function of increased spinning speeds of MAS. Upon analyzing the decay patterns of each FID, we observed a distinct increase in the T_2 relaxation time. In the rigid fraction, it expanded from 30 μs to 0.2

ms, while in the mobile fraction, it ranged from 0.5 ms to 10 ms as the MAS frequency approached 10 kHz. This indicates a substantial influence of the MAS spinning speed on the characteristics and duration of the observed transverse relaxation.

Solid-state ^{13}C NMR spectroscopy with high resolution is typically accomplished by combining magic angle spinning with high-power dipolar decoupling (DD) and cross-polarization (CP) techniques. MAS and DD play a crucial role in enhancing spectral resolution by effectively transforming broad line shapes into narrower lines.

3.6 ^{13}C NMR experiments

3.6.1   Cross-polarization and Decoupling

Line broadening in ^{13}C spectra due to the strong heteronuclear dipolar interactions between ^{13}C and ^{1}H poses a challenge. One approach to overcome this is to decouple the spins by continuously applying high-frequency pulses at the proton resonance frequency during the signal detection period [114]. In solid-state NMR, cross-polarization (CP) is a technique used to increase the sensitivity of less abundant nuclei, such as ^{13}C, ^{15}N, and ^{29}Si, by borrowing the magnetization from the more abundant nuclei, such as protons or ^{19}F. The process relies on the dipolar coupling between the two nuclei. This technique not only increases the sensitivity of the experiment but also reduces the overall time required to acquire the NMR signal, because the repetition time of the experiment is determined by the relaxation time of the proton and not by carbon which is approximately one order of magnitude longer than proton spin-lattice relaxation time, therefore signal to noise ratio can also be faster accumulated.

In the CP sequence, transverse magnetization along the x-axis is created by applying a $\pi/2$ y-pulse on the proton channel. This magnetization is then locked using an on-resonance contact pulse along x, effectively canceling out the influence of the external magnetic field during the application of the spin lock field $B_1(^{1}\text{H})$. At the same time, a spin lock field $B_1(^{13}\text{C})$ is applied on the ^{13}C channel. To achieve efficient polarization transfer two conditions must be met: coupling between the proton and ^{13}C nuclei and fulfillment of the Hartmann-Hahn match [115], which ensures that the nutation frequencies of the two nuclei being studied match. This condition is achieved by adjusting the appropriate radio frequency field strength. The transfer

of magnetization continues until an equilibrium between the ^{1}H and ^{13}C magnetizations is established, and the signal intensity reaches a plateau. In parallel, the $T_{1\rho}$ relaxation along the B_1 field of the spin-lock pulse leads to the decay of the built-up magnetization. This results in an optimum duration for the contact pulse, during which the magnetization transfer is at its maximum [115, 116].
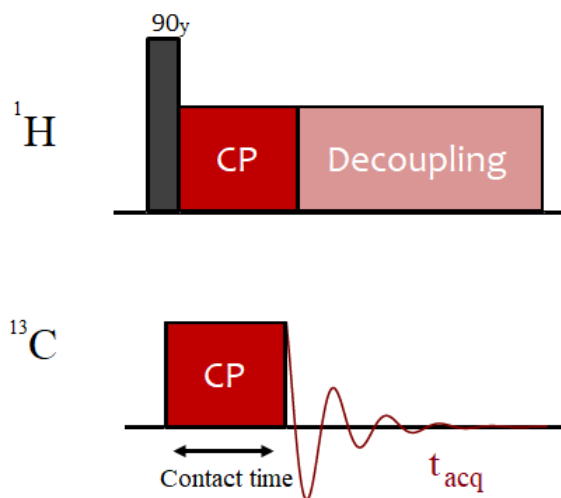

Figure 3.6. Schematic representation of the cross-polarization (CP) pulse sequence for a polarization transfer from ^{1}H to ^{13}C. Transverse polarization of ^{1}H is achieved through a $\pi/2$ pulse applied along the y-axis.

In most ^{13}C MAS NMR experiments, CP is a prevalent technique. The efficiency of this polarization transfer hinges on the contact time's duration. Given the inherent heterogeneity of solid samples, marked by diverse molecular interactions and dynamics, it's crucial to adjust the contact time in CP tests. This adjustment not only maximizes magnetization transfer but, upon optimal time determination, also enhances the signal-to-noise ratio and offers insights into molecular behaviors, all while mitigating risks like over-saturation or back-transfer of magnetization. In the case of a short contact time, only the nearest protons are able to transfer their polarization. Additionally, a stronger dipolar coupling leads to a higher rate of polarization transfer [117].

Fast molecular motions in the system have the effect of averaging the dipolar coupling, leading to a reduction in the efficiency of CP. Furthermore, when the system undergoes magic-angle spinning, the dipolar coupling is further averaged, resulting in an additional decrease in CP efficiency. The success of the Hartmann-Hahn match,

which is essential for efficient polarization transfer, relies on the MAS frequency when the spinning rates approach the magnitude of the dipolar coupling. When MAS is in play, it modifies the H-H condition: the proton spin-lock needs to match the carbon spin-lock concerning the MAS frequency. Also, the H-H condition sharpens significantly under MAS, making it challenging to calibrate. Additionally, considering inhomogeneity in the B_1 magnetic field, the polarization transfer efficiency can be relatively low. Ramp-CP comes in to enhance this efficiency by "spreading out" the sharp H-H condition to a flatter one [118]. The field strength of the ^{1}H channel is linearly varied while the second field strength remains constant. This adjustment enables control over the efficiency of polarization transfer and ensures a favorable Hartmann-Hahn match. It's important to note that the obtained spectra's intensities from CP cannot be considered quantitative. This is because the transfer of magnetization from protons to carbons occurs more efficiently for carbons bonded to protons compared to nonprotonated carbons or mobile segments with weaker H-C dipolar couplings [119].

A straightforward method to evaluate dynamic heterogeneity involves comparing CP spectra obtained using short contact times, which selectively polarize rigid, strongly dipolar-coupled ^{13}C nuclei, with one-pulse direct polarization spectra acquired with a short recycle delay of a few seconds. This comparison allows for the emphasis of signals originating from highly mobile, liquid-like ^{13}C nuclei that exhibit shorter T_1 relaxation times.

Despite the reduced quantitative accuracy, CP MAS NMR is still preferred in certain cases because the DP delay times rely on the relaxation of carbons and are much longer. This allows for a more complete longitudinal relaxation of the carbon nuclei, resulting in improved signal intensity.

3.6.2 Direct-polarization

In MAS NMR spectroscopy, direct polarization (DP) methods, coupled with extended recycle delays, are typically favored for obtaining quantitative ^{13}C spectra. DP (unlike CP) seeks to achieve balanced excitation of both the mobile and rigid components within a sample. By applying a $\pi/2$ pulse (Figure 3.7), the magnetization of the ^{13}C nuclei is transferred to the transverse plane and subsequently detected [120].
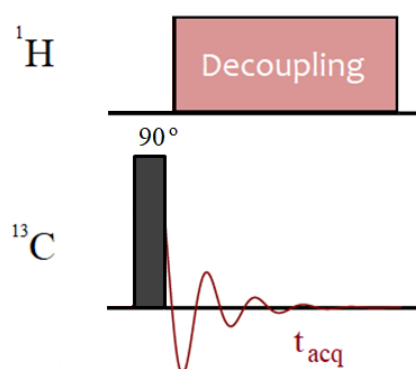
Figure 3.7. Schematic representation of the direct-polarization (DP) pulse sequence.

3.6.3 Torchia method for T_1 measurement

When aiming for accurate quantification, understanding the wide disparity in T_1 relaxation times among diverse system components becomes imperative. For instance, within polymorphic systems, the crystalline regions can exhibit notably prolonged T_1 times, sometimes extending up to 100 seconds. This contrasts the amorphous regions, where the heightened molecular mobility often results in much shorter T_1 times. This, coupled with a low signal-to-noise ratio, makes the saturation recovery sequence impractical for measuring T_1. However, the T_1 relaxation time of ^{13}C nuclei is an important parameter as it provides valuable information about molecular motions. The Torchia pulse sequence utilizes cross-polarization transfer from protons to carbons, providing the advantages of an enhanced signal-to-noise ratio and a shorter recycle delay for protons. This sequence uses a two step phase cycle.
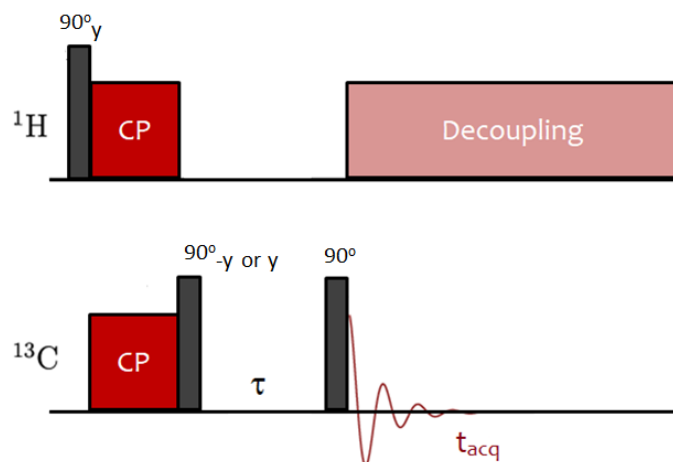
Figure 3.8. Diagrammatic representation of the Torchia experiment, comprising two sequences with distinct phases (-y and y). This discrepancy arises from the initial 90-degree pulse applied to the carbon channel. Adapted from [121].

Initially, the magnetization of protons is transferred to carbons by using a cross-polarization contact pulse, following a $90°_y$ pulse in the proton channel. Once enough polarization has been transferred, the magnetization in ^{13}C nuclei is rotated along the z-axis using a $90°_{-y}$ pulse. This magnetization gradually decreases over time until it reaches M_0, which represents the distribution of ^{13}C spin states in a static magnetic field at a specific temperature. After a certain waiting period, another 90° pulse redirects the magnetization to the x-y plane, enabling the recording of a Free induction decay signal with the protons decoupled. In the second step of the phase cycle, y, the phase of the initial 90° pulse applied to the carbon channel is varied and is selected in a way that causes the transferred magnetization to align along the negative z-axis. By subtracting the detected magnetization from both steps of the phase cycle, the longitudinal magnetization decays to zero with the T_1 relaxation time of the rigid component of ^{13}C. It is important to note that a second variant of Torchia's z-filter decay technique, which employs direct polarization with a 90° ^{13}C excitation pulse instead of cross-polarization, allows for the measurement of T_1 relaxation times across the entire sample.

3.6.4   The $T_{1\rho}$ relaxation time

To study molecular dynamics in solids and analyze the amplitudes and correlation times of molecular motions in the microsecond time scale, a key tool is the measurement of the rotating frame relaxation time, $T_{1\rho}$, which refers to the rate of magnetization decay along the radio frequency field when subjected to a spin-locking pulse in the rotating frame of reference. It serves as an analogous parameter to T_1 but specifically describes the relaxation behavior along the applied RF field of the pulse which remains static in the rotating frame, rather than the relaxation along the static B_0 magnetic field. The significance of ^{13}C $T_{1\rho}$ measurements lies in ability to provide more detailed information compared to measurements of the analogous $T_{1\rho}$ relaxation times for protons. $T_{1\rho}$ relaxation times for protons are susceptible to homonuclear spin diffusion, which complicates their interpretation, especially in polymers where molecular mobility varies throughout the sample. In contrast, ^{13}C $T_{1\rho}$ are less susceptible to proton spin diffusion, making them more suitable for studying molecular motion in polymers. Furthermore, ^{13}C $T_{1\rho}$ measurements allow for a more selective examination of molecular motion due to techniques such as magic angle sample spinning, which enables the resolution of chemically distinct carbon resonances [122].
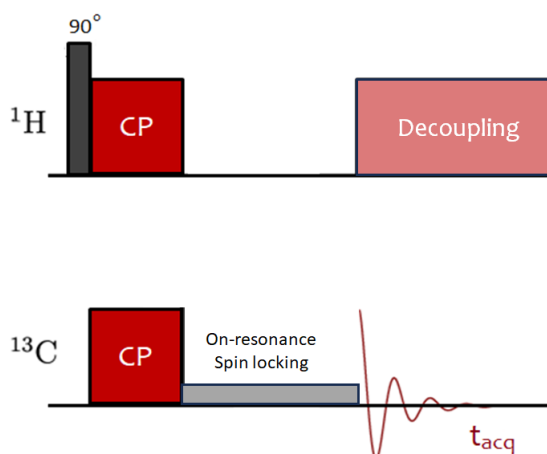

Figure 3.9. Pulse sequence for the on-resonance $T_{1\rho}$ experiment. Adapted from [123]. $T_{1\rho}$ is measured by analysing the intensity of the NMR signal in spectra collected as a function of the duration of the spin locking pulse, τ_{SL}.

The $T_{1\rho}$ relaxation time of ^{13}C can be measured using two distinct pulse sequences: cross-polarization and direct polarization. In the CP method, the sequence begins with a 90° proton pulse, followed by simultaneous spin-locking of both ^{1}H and ^{13}C nuclei under the Hartmann-Hahn condition. This facilitates magnetization transfer from protons to carbons, enhancing the ^{13}C signal. Conversely, the DP method starts with direct excitation of ^{13}C nuclei using a 90° carbon pulse. A variable-length spin-locking pulse is then applied on the ^{13}C channel. During this spin-locking period, the magnetization vector, initially aligned with the strong B_0 field, decays towards a low equilibrium value within the weaker B_1 field. The NMR signal intensity is measured as a function of the spin-locking duration, yielding a decay curve characterized by the time constant $T_{1\rho}$. The CP-based $T_{1\rho}$ measurement, primarily reflects the relaxation of rigid components and is influenced by ^{1}H-^{13}C dipolar interactions. In contrast, the DP-based $T_{1\rho}$ measurement, provides information about the bulk carbon relaxation, including both rigid and mobile components. The comparison of $T_{1\rho,\mathrm{CP}}$ and $T_{1\rho,\mathrm{DP}}$ can offer valuable insights into molecular dynamics and structural heterogeneity in the sample.

In static samples, $T_{1\rho}$ directly correlates with the spectral density at the spin-lock frequency. However, when measuring $T_{1\rho}$ under MAS conditions and accounting for heteronuclear dipolar and CSA relaxation mechanisms, it aligns with a specific combination of spectral-density functions:

$$\frac{1}{T_{1\rho}} \propto K_{CH}(J(\omega_{SL} - 2\omega_{MAS}) + 2J(\omega_{SL} - \omega_{MAS}) + 2J(\omega_{SL} + \omega_{MAS}) + J(\omega_{SL} + 2\omega_{MAS}))$$

(3.11)

Where ω_{MAS} and ω_{LS} are the MAS and spin lock frequencies respectively and K_{CH} is the ^{13}C-^1H coupling constant ($2.12 \cdot 10^{10} s^{-2}$) which is doubled for CH_2. The ^{13}C $T_{1\rho}$ measurement is sensitive to molecular motions. In systems where multiple relaxation mechanisms are at play (e.g., dipolar interactions, chemical shift anisotropy, or exchange processes), varying the spin-lock frequency can help to determine the motional correlation function more precisely. Different spin-lock frequencies can be sensitive to different rates of molecular motion. By sampling across a range of frequencies, you can probe molecular dynamics across various timescales [124,125]. To study slow dynamics, we take advantage of the frequency difference between the spin-lock

and MAS frequencies. However, rotary resonance conditions, such as $\omega_{LS} = \omega_{MAS}$ and $\omega_{LS} = 2\omega_{MAS}$, should be avoided because they result in the recoupling of dipolar interactions and chemical shift anisotropies [123, 126].

To interpret the carbon $T_{1\rho}$ data, we employed the correlation function formalism and the model-free approach, which are commonly used in dynamic studies. Kurbanov et al. [127] explored the applicability of the well-known model-free approach for analyzing solid-state NMR relaxation data. Study demonstrates that the auto-correlation functions and hence, the spectral density functions are practically identical regardless of the correlation time of motion. Rather than breaking down the correlation function into a few discrete exponential components, they present a more effective method to capture the form of the correlation function by incorporating a continuous distribution of correlation time. Among the various convenient phenomenological distribution functions, the Fuoss-Kirkwood distribution function [123, 126] emerges as a suitable choice. The spectral density function undergoes a transformation when the sample nucleus engages in two separate motions characterized by different time scales:

$$J(\omega) = (1 - S_2^2) \cdot \frac{\beta_2}{\omega} \cdot \frac{(\omega\tau_2)_2^\beta}{1 + (\omega\tau_2)^{2\beta_2}} + S_2^2 \cdot (1 - S_1^2) \cdot \frac{\beta_1}{\omega} \cdot \frac{(\omega\tau_1)_1^\beta}{1 + (\omega\tau_1)^{2\beta_1}} \qquad (3.12)$$

Here, $S_{1,2}^2$ and $\tau_{1,2}$ denote the order parameters and correlation times corresponding to two distinct motions, specifically, the fast and slow motions in our scenario. The dynamic order parameter S^2, serves as a quantitative measure of anisotropy, precisely quantifying the ratio between residual dipolar coupling and the static dipolar coupling, providing the degree of anisotropy of the corresponding motion, and β is the distribution width parameter from zero for infinitely broad distribution to one for no distribution. A nonzero order parameter value denotes restricted orientation fluctuations of the segments, whereas a zero value denotes the locally isotropic melt phase.

As will be demonstrated later, the selected model for this study incorporates two distinct motional modes: fast internal conformational motion occurring on the picosecond time scale, and a slower motion. To account for the internal dynamic heterogeneity within our sample, we incorporate a distribution of correlation times that characterizes the fast internal motion. Two fundamental assumptions underpin-

ning our analyses are as follows: First, the order parameter for both motions remains unaffected by temperature variations. Second, the temperature dependence of the correlation times follows the modified Arrhenius law, $\tau = \tau_{293K} \cdot \exp\left(\dfrac{E_a}{R}\left(\dfrac{1}{T} - \dfrac{1}{293}\right)\right)$, where τ_{293K} is correlation time at 20°C (293 K), R is the universal gas constant, E_a is the activation energy.

Experimental details

4.1   Measurements

The NMR measurements were conducted at the house by myself (NMR group, in-stitute of Physics). Investigations using X-ray scattering and dynamic differential calorimetry were undertaken by our colleagues in Korea and Freiburg. Details regarding the spectrometers utilized can be found below.

^{1}H-NMR Analysis: [1]H time domain signals, FIDs were acquired utilizing a Bruker Avance III spectrometer, operating at a Larmor frequency close to 200 MHz. The 5 mm static probe head with a short dead time of around 2.5 μs was used. Each measurement adopted a 90° pulse duration of 3.0 μs. To ascertain the magnetization's full relaxation, intervals between successive measurements were set to 5 times T_1 with saturation recovery assessments conducted at each temperature setting. We maintained a uniform count of recorded measurements in a series, optimizing for an adequate signal-to-noise ratio. The sample's temperature was precisely controlled, within an accuracy of 1K, using either warming or cooling airflow, while ensuring a temperature differential of about 0.5K. Calibration of the temperature was anchored to the ^{1}H resonance positions found in methanol or ethylene glycol spectra [128]. A standard procedure was to wait for a minimum of 20 minutes post any temperature adjustment before commencing measurements.

The PEO/Clay nanocomposites project data sets were captured using a Bruker minispec mq20. This instrument operated at a proton resonance frequency of 20 MHz and was associated with a static magnetic field strength of 0.5 T. The experiments involved typical 90° pulse durations of 2.35 μs and recycling delays of 3 s to ensure complete relaxation. For these measurements, NMR tubes of 10 mm in diameter were employed. To prevent undesired water and oxygen intake, these tubes were first evacuated, flushed with Ar, and then sealed using flames.

^{13}C-NMR Measurements: Experiments utilizing ^{13}C-MAS were conducted on a Bruker Avance spectrometer, with a carbon Larmor frequency of roughly 100 MHz. We used a Bruker 4mm double-resonance MAS probe head. 5 and 10 kHz MAS frequency were used. In ^{13}C $T_{1\rho}$ measurments, the ^{1}H-90° pulse had a duration of 3.0 μs, the ^{13}C-90° pulse's length was between 3 μs and 4 μs. The delay for the ^{13}C-CP measurements was set to five times the T_1 of protons, while the ^{13}C-DP spectra had a recycle delay of 8 seconds. The CP contact time fluctuated between 0.3 and 0.4 ms based on temperature. ^{13}C $T_{1\rho}$ measurements A minimum of 1024 scans were recorded, contingent on sample volume and signal-to-noise ratio. The COO resonance of l-Alanine at 176.6 ppm served as a reference for the ^{13}C spectra.

4.2   Materials

PEO/Clay nanocomposites: were produced by our collaborators in Freiburg. NHT was supplied by Topy Industries Ltd. PEO of four distinct molecular weights ($M_v = 2$kg mol^{-1}, $M_v = 20$kg mol^{-1}, $M_v = 2000$kg mol^{-1} $M_n = 2000$ kg mol^{-1}) was sourced from Sigma-Aldrich and utilized as received without additional purification. All preparations incorporated deionized water. PEO/NHT nacre-like structures were created using a purified aqueous NHT dispersion with a concentration of 50 % was gradually introduced to a vigorously mixed PEO solution of 50 wt %. After mixing continuously for 24 hours, the combined solution was poured into Petri dishes. Upon drying at ambient conditions, the resultant films had an approximate thickness of 30 μm.

The labeling system for the samples is PEOMW$_{wt\%}$/NHT$_{wt\%}$. The samples utilized have molecular weights of 2k, 20k, and 2M along with different weight percentages of PEO and NHT, which included combinations of of 50/50, 40/60, and 30/70 wt %.

PEO/SiO$_2$ nanocomposites: were produced by our collaborators in Korea. Silica nanoparticles of varying diameters of 10 nm, 40 nm, and 90 nm, and varying volume fractions, spanning from 0.05 to 0.65 were synthesized based on the method of Stöber [129] utilizing base-catalyzed hydrolysis and condensation of tetraethylorthosilicate (TEOS), were dispersed in solvents, either ethanol or water. The average silica particle diameters were determined by SEM micrographs and the analysis of the particle form factor was obtained through the angle dependence of neutrons scattered

from a dilute suspension. These dispersions were then mixed vigorously with PEG, having different molecular weights (MWs) of 0.4, 3.3, and 20 kg/mol. The PEO was hydroxyl-terminated (=PEG) and was purchased from Sigma-Aldrich. The volume fractions of particles were determined based on the mass of individual components and their respective densities. The density value for the silica particles stands at 1.6 g/cm^3. The resulting PNCs were obtained by rapidly evaporating the solvent in a vacuum oven set at 70°C [24].

The labeling system for the samples follows the format: initial solvent (PEO MW-diameter-Φ_c). For example, E(PEO3k-40nm-0.5) indicates a polymer-nanoparticle composite consisting of 50% volume silica particles (40 nm diameter) mixed with PEO of 3 kg/mol molecular weight, initially dispersed in ethanol.

Poly(ethylene oxide)/Clay Nanocomposites

In this section, we investigate the behavior of poly(ethylene oxide) (PEO), a crystal-mobile polymer, when mixed with sodium fluorohectorite platelets (NHT), a natural nacre model also known as "mother of pearl." This combination provides a well-defined layered nanocomposite arrangement, making it an ideal system for studying polymers under nano-confinement. However, the structure of PEO within the narrow 1 nm gaps between the inorganic layers is not well understood. The objective of this study is to determine the effect of PEO chain confinement within the nanoclay sheets on its dynamics. We used proton low-resolution solid-state NMR to carefully investigate the motion of PEO chains within the inter-layer spacing. By quantifying the amount of mobile and immobilized polymer species, we found evidence of immobilized polymer layers between the nanoclay galleries and around the proposed tactoid stacks embedded in a PEO matrix. Our focus was on understanding the timescale and amplitude of motion of the confined polymer within the gallery spacing. Overall, this study sheds light on the behavior of PEO under nano-confinement, providing insights into the structure and dynamics of polymers in such systems.

5.1   Characterization process

The lateral dimensions of the clay and its ability to break up into individual layers determine the aspect ratio of the clay, which in turn, has a significant impact on the interfacial interactions between polymer and clay. The exceptional mechanical properties of nacre arise from the presence of well-ordered hard and soft building blocks, creating a "brick-and-mortar" structure. The hard platelets function as load-bearing and reinforcing components, while the soft polymer segments dissipate energy. This subsection focuses on the preparation and characterization of samples, using

nacre as a model for developing advanced materials [130–132].

We employed a synthetic nanoclay, NHT (sodium fluorohectorite), with an aspect ratio of 750 and a thickness of approximately 1 nm [25]. NHT has a weight percentage of above 50% and is free from paramagnetic contamination, making it suitable for NMR investigations. As the polymer component, we selected PEO with various molecular weights ranging from 2 kg/mol to 2000 kg/mol. The entanglement molecular weight of PEO is approximately 1620 g/mol, and it has T_m and T_g at 339 K and 206 K, respectively. However, the use of conventional processing methods for high-aspect-ratio nanoclays with a high level of reinforcement is not recommended due to high melt viscosity and poor order formation. Our collaborators developed a waterborne dispersion casting method to produce ordered layered nacre-mimetic films. This method involves mixing water-soluble polymers and fully delaminated nanoclay sheets to form core/shell nanoplatelets. Concentration-induced self-assembly occurs upon drying, resulting in highly ordered layered structures.

5.2   Structural analysis by XRD

X-ray diffraction (XRD) study of a standard composition with equal weight percentages of polymer and clay (50/50 w/w) conducted by our colleagues, as presented in Figure 5.1a, demonstrates the diffractogram of PEO/NHT at various molecular weights. The study revealed a sharp primary peak at the (001) reflection plane, which quantified the interlayer spacing to be 1.8 nm for all composite samples. In comparison, the yellow spectrum, which relates to the polymer-free neat NHT stacks, exhibits a unique peak of NHT, releasing a d-spacing of about 1.2 nm, indicating that each clay platelet has a thickness of 1 nm. Lacking NHT peak in the nanocomposite XRD pattern, indicating successful intercalation of polymer chains in all clay stacks.
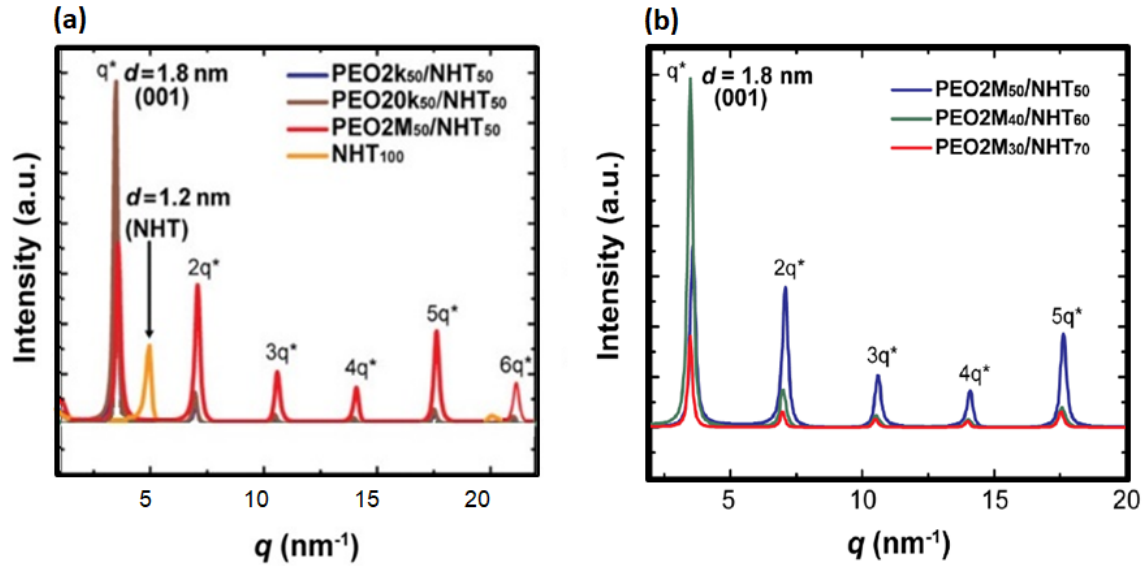
Figure 5.1. XRD diffractogram of PEO/NHT (a) Equal weight percentage of polymer and clay but different PEO molecular weights plus pure NHT (b) changing the PEO/clay ratio. Reproduced from Ref. [25] with permission from the American Chemical Society.

The second dataset, illustrated in Figure 5.1b, depicts the XRD analysis of samples with a constant polymer molecular weight of 2M, but varying amounts of NHT from 50 wt% to 70 wt%. This indicates a reduction in the proportion of polymer in the sample. Surprisingly, despite this decrease in polymer content, the gallery spacing remains constant, which distinguishes this system from others where a change in polymer content typically results in a change in the clay distance.

In Figure 5.2, the expected spacing between galleries at various polymer/nacre ratios is illustrated using simple geometric calculations [25, 133]. These calculations demonstrate that the observed d-spacings of nacre-mimetics, with a weight fraction of 50 wt%, consistently fall below the predicted value from equation 5.1. Specifically, equation 5.1 suggests that a 50/50 w/w mixture of a polymer with a density of 1.21 g cm^{-3} (PEO) and a nanoclay with a density of 2.78 g cm^{-3} (NHT) should produce films with a d-spacing of approximately 3.3 nm (as depicted in Figure 5.2). However, our experimental data show lower values.

$$d = h_{NHT} + \frac{\dfrac{V_{NHT} \times \rho_{NHT}}{x_{NHT}} - V_{NHT} \times \rho_{NHT}}{A^2 \times \rho_{PEO}} \qquad (5.1)$$

The variable h_{NHT} represents the height of the NHT clay platelets, while V_{NHT} stands for their volume. ρ_{NHT} refers to the density of the NHT clay, and x_{NHT} represents the weight percentage of NHT in the composite. Additionally, A denotes the surface area of the clay platelets, and ρ_{PEO} stands for the density of the PEO polymer.
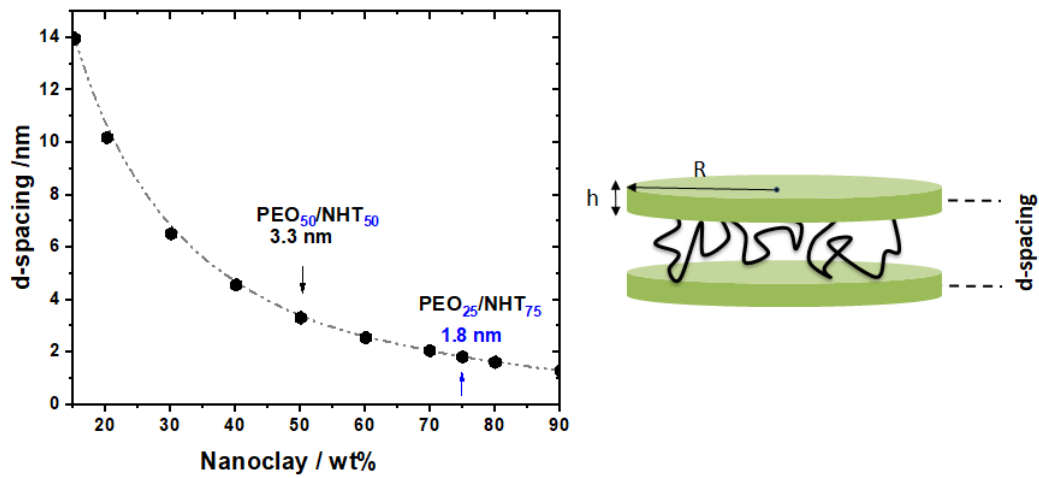

Figure 5.2. Theoretical model of dependency of d-spacing and polymer/nanoclay ratio

This prediction suggests that the interlayer spacing widens as the polymer content increases. However, our experimental results indicate a constant d-spacing of 1.8 nm for all samples, irrespective of the PEO/clay ratio. This finding aligns with the theoretical prediction that a minimum polymer share of 25/75 wt/wt is sufficient to cover all surfaces of the layered nanoclay and fill the galleries [134]. In other systems, an increased proportion of polymers can cause gallery expansion as the excess polymers intercalate between two single nanoclay platelets. However, in our system, changing the PEO/NHT ratios has no effect on d-spacing, indicating that the remaining polymers exist outside of the galleries. This outcome reveals that the excess PEO is separated into a distinct phase instead of being uniformly distributed or intercalated within the nanoclay galleries. XRD analysis confirms the absence of gallery expansion, implying that the excess PEO does not integrate into the galleries.

We hypothesize that the formation of tactoids in the film cast of a polymer-coated nanoclay mixture was caused by depletion flocculation. This is because PEO is known to effectively induce depletion flocculation [135], a phenomenon in which polymer molecules preferentially adsorb onto the surfaces of the suspended particles, reducing the concentration of polymer in the space between the particles. The study results suggest that this process led to the forced packing of core/shell polymer-coated nanoclay particles into tactoids, while the rest of the polymer formed a separate phase-segregated matrix.

5.3 Thermal studies by DSC

Previous research on polymer/clay nanocomposites has shown no evidence of crystalline melting temperatures for compositions with 70 wt% or less PEO [45, 46]. This was interpreted as a sign of complete intercalation of polymer chains between clay layers. However, our study offers a contrasting result with a clear indication of a crystalline melting transition for all samples analyzed. This is supported by the presence of endothermic peaks in the DSC profiles, which can be seen in Figure 5.3. However, there is no evidence of crystalline PEO peaks in the XRD data. This could be due to the small nanoscale size of the crystals and the reduced electron density contrast which highlights the importance of considering the limitations of various analytical techniques. The indication of excess polymer outside the clay galleries supports recent findings by Chrissopoulou et al. [45] for a series of PEO/sodium MTM nanocomposites with polymer weight fractions of 70 wt% or higher. In our study, the melting temperature (T_m) decreases with increasing NHT loading, which could be due to the reduction in the size of crystalline domains.
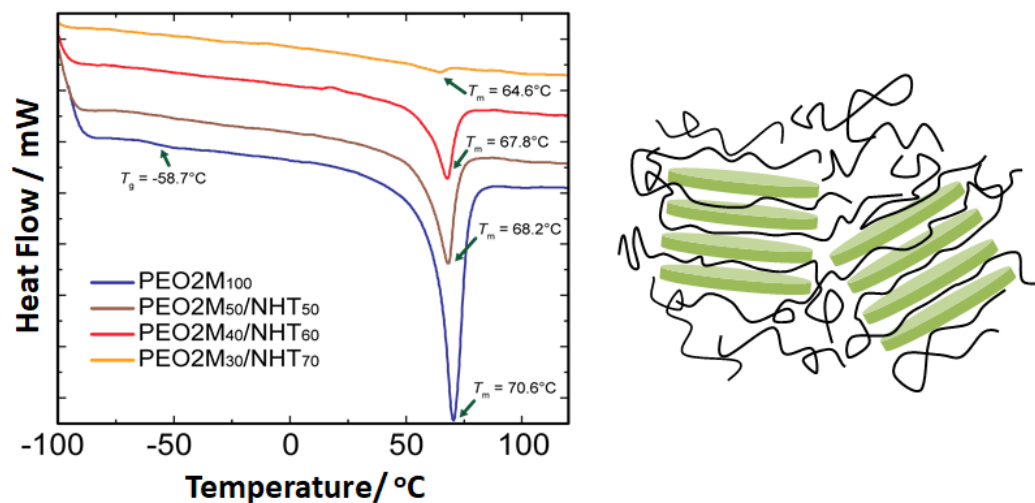
Figure 5.3. Evidence of melting transition of PEO2M/NHT nanocomposites by DSC. Adapted from Ref. [25] with permission from the American Chemical Society.

It is noteworthy that the presence of PEO crystallinity in our samples, even at lower PEO contents, can be attributed to the formation of a dominant tactoid structure with a defined stoichiometry. This stands in contrast to melt-intercalated samples, where achieving a well-defined structure formation is more challenging due to a lack of dynamics. It is important to mention that our nanoclay materials underwent a thorough purification process, resulting in single, well-delaminated nanosheets. The absence of non-delaminated agglomerates further bolsters the validity of our results. Overall, our findings offer fresh insights into the relationship between the composition of polymer/clay nanocomposites and their crystalline behavior.

5.4 Dynamic and structural studies by ^{1}H NMR

An investigation into the molecular dynamics of PEO, using low-resolution proton NMR at a range of temperatures was conducted. Measurements were carried out using a Bruker minispec mq20, which has a proton resonance frequency of 20 MHz and a static magnetic field of 0.5 T. To achieve full relaxation, we used standard $\pi/2$ pulse durations of 2.35 μs and recycle delays of 3 s. To prevent water and oxygen absorption, we evacuated the 10 mm diameter NMR tubes with Ar and flame-sealed them.

5.4.1 Hydration and dynamic state of polymer

To determine the molar fractions of each phase in this multi-phase system, the proton FID and the MSE pulse sequences were utilized. To avoid the effects of B_0 inhomogeneity in the low-field NMR instrument and assess slower large-scale motions, we used the Carr-Purcell-Meiboom-Gill (CPMG) echo train experiment with MLEV-4 phase cycling to suppress artifacts from pulsed spin lock effects. The CPMG decay curve extended the decay of the FID data, enabling us to properly distinguish intermediate-to-slow timescale dynamics in the amorphous phase. We simultaneously fitted both the FID extended with CPMG and MSE signals, assuming that the relaxation components had equal shapes but different amplitudes, which means all β exponents are shared in the global fit of MSE-FID and combined FID-CPMG data but the amplitudes of the components are fitted independently.
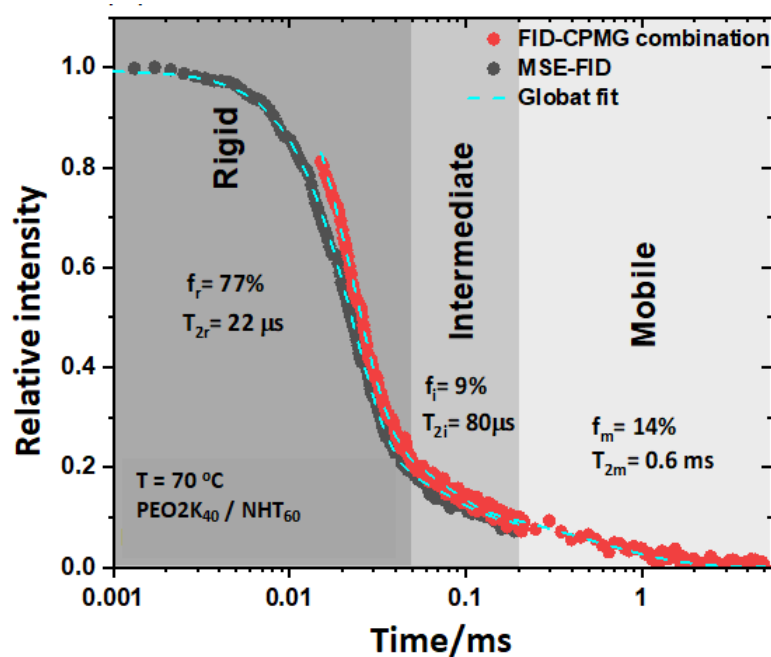

Figure 5.4. Proton low-resolution NMR, Global fit of MSE-FID and combined FID-CPMG data for the sample with 70 wt% clay content and 30 wt% PEO2k (dried). Adapted from Ref. [25] with permission from the American Chemical Society.

Figure 5.4, which depicts the decay behavior of the NMR signal in PEO2k with 60% NHT at 70 °C, a good fit to the full decay is obtained using a combination of stretched or compressed exponential functions with a shape parameter of $0.8 \leq \beta \leq 2$.

The observed decay behavior and associated T_2 values in this system are a result of the strength of dipole-dipole couplings between the protons in the sample. The strong couplings lead to a short T_2 rigid limit in the range of 10 - 20 μs follows the decay shape of a Gaussian function with $\beta = 2$, with the fast initial decay within a few tens of microseconds, assigned to the intercalated portion of PEO or some crystalline component. An intermediate phase with slightly lower residual dipolar couplings arises from a partially anisotropic chain motion decay at longer time scales associated with the chains located near the edges of the clay nanosheets and free isotropically moving polymer chains which exhibit a relatively mobile phase with quick segmental movements and a relatively long T_2 in the millisecond to the second range.

The impact of water within the galleries was explored by comparing NMR results of hydrated and dried samples. Our research has shown a direct correlation between hydration and the dynamics of polymers. As shown in Figure 5.5, we examined the NMR data of ambient hydrated and dried samples, in a way that the same measured sample was placed for 48 hours in a vacuum oven at 60 °C and measured again under the same procedure. For instance, in the case of PEO2M$_{40}$/NHT$_{60}$, the significant change in relaxation rate is quite obvious, indicating the presence of water in the galleries. The results showed that drying led to a decrease in the mobility of the nanoclay-associated fractions, as seen in the significant shortening of the T_2 values in the early stages of decay.

It has long been known through various methods such as wide-angle X-ray diffraction, infrared, and Raman spectroscopy, that a PEO chain in its crystalline state exhibits a helical structure. Previous studies have often assumed a helical structure for intercalated PEO, but this is still a subject of debate. This structure is defined by the presence of gauche OC-CO torsions and trans CO-CC torsions. Schmidt-Rohr and co-workers [46] studied a fully intercalated PEO system and proposed that if all of the gauche OC-CO bonds in long chain sections have the same sign, either all gauche+ or all gauche-, the chain would form a helix. However, their observations showed that only 10% of the OC-CO bonds in intercalated PEO were in the trans conformation, and a significant percentage of the CO-CC bonds were likely in the gauche conformation. This suggests that a helical structure is unlikely. One hypothesis is that water may cause the disordering of some helical parts, making local motions more isotropic. In this sense, water acts as a plasticizer in hydrated samples.
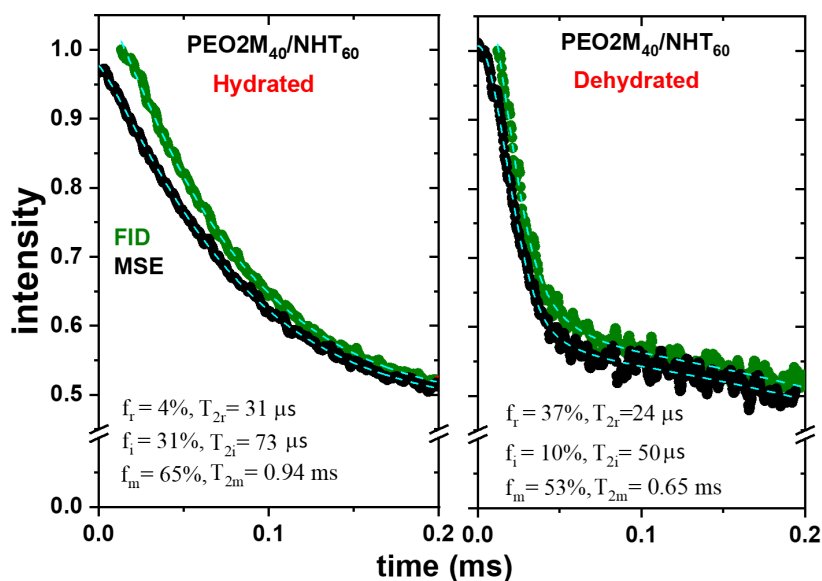
66

Figure 5.5. Proton low-resolution NMR, the comparison of an ambient hydrated and dried sample with 60 wt% clay and 40 wt% PEO2M at 70°C. Adapted from Ref. [25] with permission from the American Chemical Society.

From now on we concentrate on dried samples since hydrated samples make it more difficult to distinguish between PEO linked with nanoclay and more mobile portions due to the presence of water and the longer T_2 values [136, 137].

The results of a study on the temperature dependence of PEO/NHT samples showed a significant correlation between temperature and both the amount of polymer that was immobilized and the duration of its relaxation. This pattern was consistent across all NHT fractions and molecular weights of PEO. As illustrated in Figure 5.6, specifically, we observe a significant decrease in the amount of immobilized fraction above 60 °C, transitioning from a high value that includes both crystalline PEO and clay-confined PEO to a lower value at temperatures above 60 °C, where the crystals are molten and only confined PEO remained. This suggests that the only component that retains stability beyond the melting point of PEO is the confined polymer chains in the galleries. Therefore, all subsequent tests from here on were performed at 70 °C.
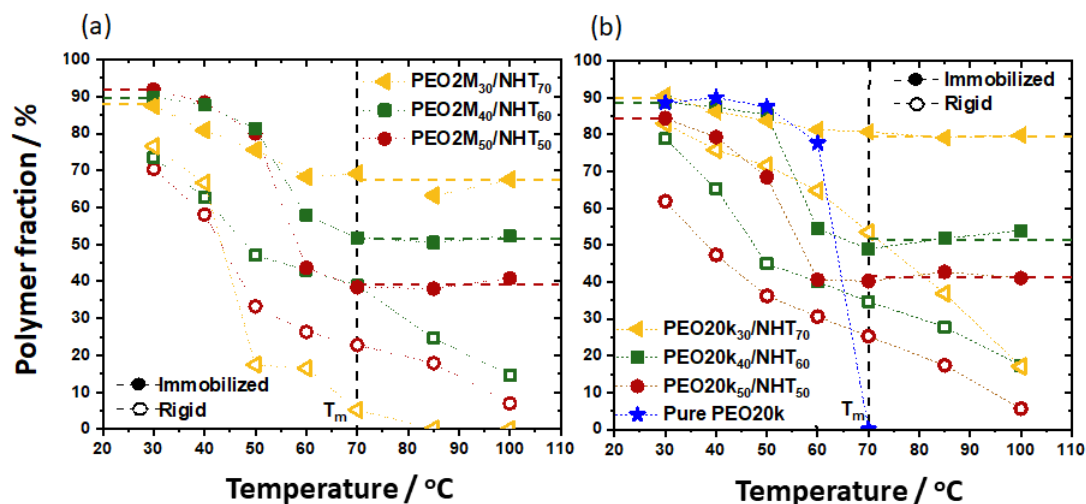
Figure 5.6. Total immobilized polymer fraction of a) PEO2M and b)PEO2Ok with NHT content variation as a function of temperature (the distance between the high-T and low-T horizontal dash lines of each color represents the amount of crystalline material).

Our study also demonstrates the significant impact of clay concentration and PEO molecular weight on the behavior of PEO/NHT nanocomposites. Therefore NMR measurements were done in a series of samples with all different PEO molecular weights in different ratios and measurement temperature set at 70 °C. The effect of rising clay content on each molecular weight of PEO is depicted in Figure 5.7, which reveals that the immobilized fraction increases almost linearly with the NHT content above the bulk melting point. At a constant clay content, there is a slight inverse trend with the molecular weight of the intercalated polymer being higher. In a system like ours, where the interlayer spacing remains constant, high molecular weight polymers can result in a greater number of polymer chains remaining outside the gallery, rather than being confined within tactoids. These chains have the potential to reinforce and stiffen the entire system by forming more bonds between the nanoclay particles. However, shorter chains are able to more easily penetrate the interlayer space, which leads to an increase in the amount of intercalated PEO that is immobilized within the gallery.
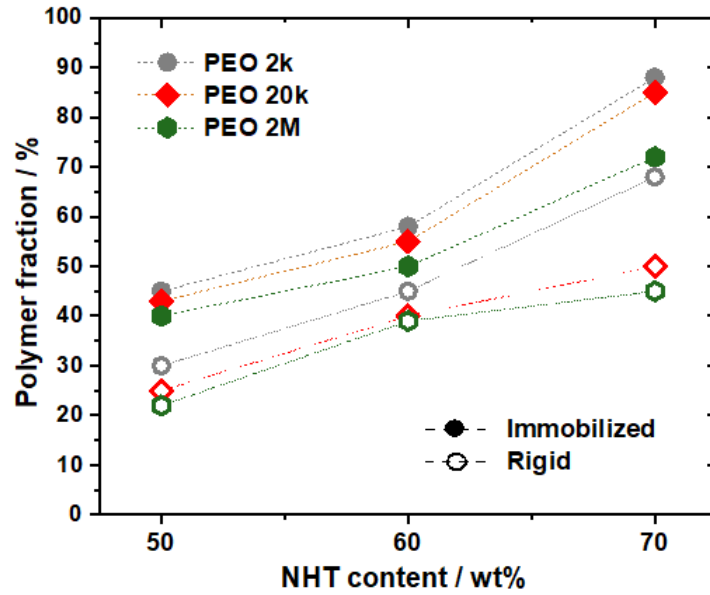
Figure 5.7. Influence of increasing clay concentration for all PEO molecular weight.

To calculate the fraction of PEO incorporated between the clay nanosheets in a layered system, we performed a model calculation using X-ray data and NMR-determined mass fractions. Our calculation assumed that the intra-gallery PEO has the same density as PEO in the bulk. We also assumed a layered system (a stack of sheets), where the height of pristine nanoclay is $h = 1$ nm and the change in height after intercalation of polymer is $t = 0.8$ nm. Thus, we defined $V_{NHT} = kh$, $V_{PEOin} = kt$, and $V_{PEOout} = v'$, which together make up the system's overall volume. We used the concept of mass conservation, and with knowledge of the densities of PEO and NHT, we provide an example calculation for a sample with 70% wt NHT:

$$f_{NHT} = \frac{Mass_{NHT}}{Mass_{total}} = \frac{kh \cdot \rho_{NHT}}{kt \cdot \rho_{PEOin} + kh \cdot \rho_{NHT} + v' \cdot \rho_{PEOout}}$$

$$\frac{v'}{k} = 0.985 - 0.66 \cdot \rho_{PEOin}$$

and also from NMR, where the amplitude of the decay curve for a specific relaxation component is directly proportional to the amount of that component in the

sample, the mass fraction of the component in the sample can be quantified:

$$f_{immob.} = \frac{M_{PEOin}}{M_{PEOin} + M_{PEOout}} = \frac{kh \cdot \rho_{PEOin}}{kt \cdot \rho_{PEOin} + v' \cdot \rho_{PEOout}}$$

$$\frac{v'}{k} = \frac{t \cdot \rho_{PEOin}}{\rho_{PEOout}} \cdot \left(\frac{1}{f_{immob.}} - 1\right)$$

by equating two equations, one from the mass conservation definition and the other from the NMR definition, we theoretically calculated polymer fractions which are listed in brackets in the following in table 5.1.

The results showed that when the share of polymer in the sample is much lower than clay, the majority of the polymer is incorporated between the clay nanosheets. However, in samples with an equal share of polymer/clay, a significant amount of polymer remains outside the sheets, which is the reason for the bulk-like behavior of the system. The data obtained by DSC and NMR were found to have a good consistency, although there may be some deviations due to the different enthalpy of fusion in the samples, caused by the strong confinement due to a high clay content in the sample. This study allows us to estimate the PEO crystallinity ratio outside the nanoclays sheets and confirm that polymers confined in less than 1 nm space can no longer crystallize. The immobilized fraction measured at 25°C only has to be subtracted from the stable intercalated contribution obtained at and above 70°C.

Table 5.1: Fractions and Crystallinity of all Nanocomposites obtained by NMR and DSC Experiments

		fraction (%) average for T≥ 70°C		Crystallinity at 25°C(%)	
MW	PEO/NHT	immobilized[1]	mobile[1]	NMR	DSC
PEO2k[2]	50/50	43.7(35)	56.3(65)	-	-
PEO2K	40/60	57.1±1.5(52)	42.9±1.5(48)	30.0	-
PEO2k[2]	30/70	86(80)	14(20)	-	-
PEO20k	50/50	41.3±1.3(35)	58.7±1.3(65)	43.1	-
PEO20K	40/60	51.6±2.5(52)	48.4±2.5(48)	37.2	-
PEO20k	30/70	79.8±0.8(80)	20.2±0.8(20)	10.8	-
PEO2M	50/50	39.1±1.5(35)	60.9±1.5(65)	49.3	59.9(37)[3]
PEO2M	40/60	51.5±0.9(52)	48.5±0.9(48)	36.3	59.8(29)[3]
PEO2M	30/70	66.7±3.1(80)	33.3±3.1(20)	14.2	12.7(4)[3]

[1.] Error margins reflect the standard deviations of experiments at different temperatures; fractions in brackets are predicted values based on the d-spacing from XRD. [2] Sample measured only at 70°C.[3] Crystallinity based on the total polymer mass obtained by DSC.

5.4.2   Timescale and amplitude of motion

Let's delve into the information about the motion of confined PEO. As previously mentioned, the MSE sequence proves to be a superior method in detecting strong dipole interactions compared to the FID but the MSE also has a signal loss that varies based on echo pulse sequence defects, and the strength of dipole coupling, which makes it a valuable tool for exploring molecular dynamics on intermediate timescales. Figure 5.8 highlights the MSE signal loss (i.e., the ratio of the fitted amplitudes at zero acquisition time) for both pure PEO and PEO/NHT as the temperature changes. Below the melting temperature, there is a significant loss of signal and a pronounced temperature dependency. This signal loss is due to the motion of the PEO chains within the crystalline domains, which occurs on an intermediate timescale of around 10 μs. This intercrystalline motion is the reason why PEO is classified as a crystal-mobile polymer. However, above the melting temperature, the signal loss remains relatively stable at approximately 15%. The rate of signal decay in NMR is related to the correlation time of the molecular motion. The signal loss in MSE becomes

more pronounced as the correlation time of the molecular motions increases. This observation suggests that the motion of the PEO chains between clay nanosheets is in the fast-motion limit, meaning that the motion occurs on a much shorter timescale with a correlation time much shorter than 10 μs. This observation may hold true even at temperatures below 60°C, where the larger signal loss primarily originates from the crystalline fraction.
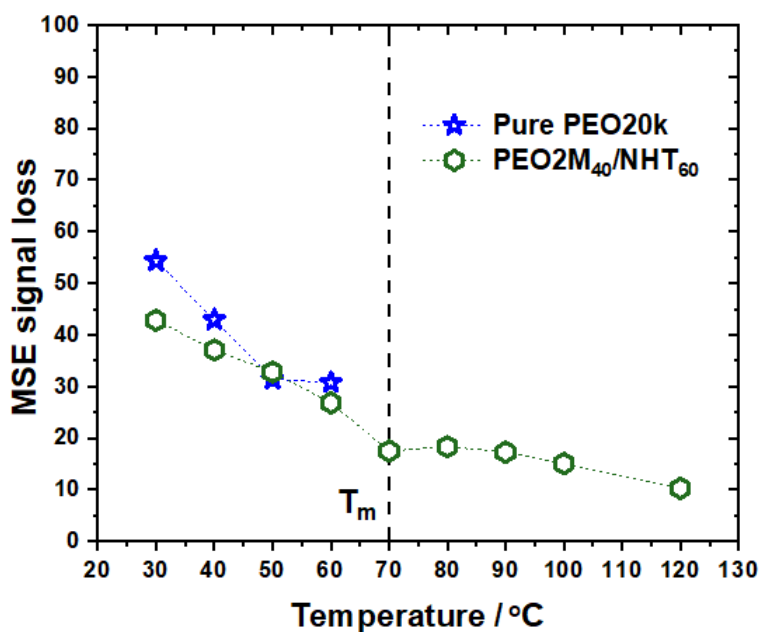

Figure 5.8. MSE signal loss of PEO20k and PEO20M$_{40}$/NHT$_{60}$ as a function of the temperature. Adapted from Ref. [25] with permission from the American Chemical Society.

In Figure 5.9, we analyzed the T_{2r} values and their temperature dependence, focusing on the immobilized polymer phase corresponding to a near-Gaussian decay in the fast initial part of the FID decay. We compared the behavior of confined PEO to that of neat PEO. We observed that the segmental motions of PEO chains confined between clay nanoplatelets are initially constrained in amplitude, with a relaxation time shorter than in crystalline PEO at the same temperatures which means chains are more restricted in their motions.
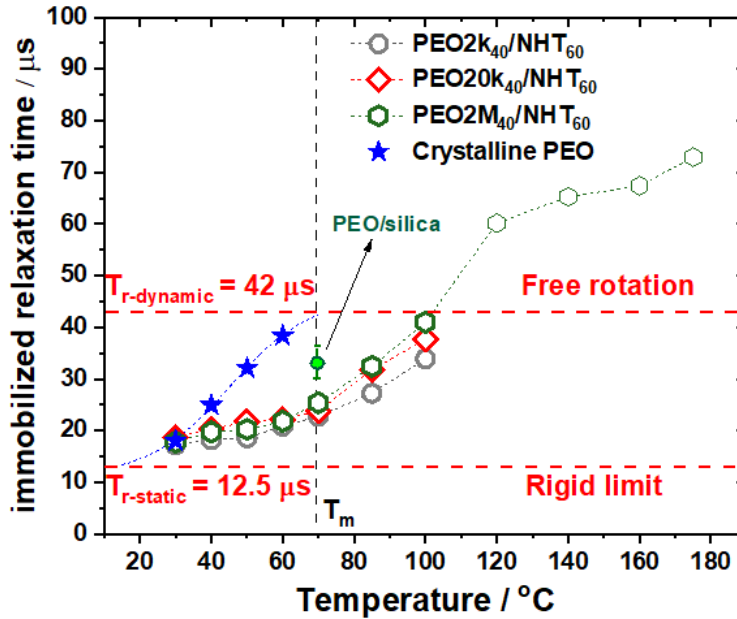
Figure 5.9. Transverse relaxation time T_{2r} in PEO20k crystallites and PEO/NHT with different molecular weights, both as a function of temperature. Adapted from Ref. [25] with permission from the American Chemical Society.

With an increase in temperature, the chains in crystalline PEO undergo fast rotation [138]. However, the "free-rotation limit" of T_{2r}, is not reached before the PEO melts, but we can estimate it through extrapolation. The T_{2r} relaxation time of a molecule reaches a maximum value at the free-rotation limit, the chain is able to rotate rapidly around its bonds without being constrained by its environment. On closer inspection, the T_{2r} values of confined PEO initially cover the same range as compared to PEO crystallites but shift in temperature. These values further increase to a significantly higher plateau, suggesting larger conformational freedom than in the neat PEO.

We observed that the dynamics of the confined PEO chains in NHT galleries occur at a faster timescale than in PEO crystallites above 60 °C, as indicated by the low MSE signal loss. Interestingly, the T_{2r} relaxation time of the confined PEO chains increases to values beyond the intra-crystalline free-rotation limit at a much higher temperature than that observed in PEO crystallites. This implies that the motional amplitude of the confined PEO chains is a strong function of temperature and differs from that of PEO in its crystalline form. We propose that the difference in motional

amplitude could be due to a change in the helical structure of the PEO chains with increasing temperature. Specifically, we hypothesize that the PEO chains adopt an increasingly disordered structure at higher temperatures, which provides the chains with greater conformational freedom. The results are similar to those of Jurga et al. [139] regarding PEO in the interlayer space of MTM. However, it is important to keep in mind that they used proton T_1 relaxation, which can be influenced by paramagnetic impurities and de-localization due to spin diffusion.

In Figure 5.9, we have incorporated the T_{2r} value derived from another study on our model polymer nanocomposite, where PEO is anchored to silica particle surfaces. Notably, the observed T_{2r} value exceeds what is typically anticipated for a rigid glassy polymer. This can be attributed to the internal mobility of the interfacial PEO layer in the vicinity of the silica surface. It should be noted this value remains unaffected by temperature variations [22]. The results will be discussed in detail in the next chapter. But comparing the T_{2r} values of PEO molecules in these different environments can provide insights into the extent of molecular confinement and the nature of the interactions between PEO and the different surrounding environments. It can be said that the motional amplitude of PEO is a strong function of temperature and it varies depending on whether is absorbed on the silica surface or intercalated in clay sheets, or confined in its own crystal structure. This difference can be explained by the different chemical structures of nanoclay and silica. As can be seen at the melting temperature, PEO molecules confined between the NHT galleries, are more restricted in their motion which also led to a shorter T_{2r} value compared to the PEO/silica. But as mentioned earlier, the increase in T_{2r} of confined PEO with temperature indicates that the PEO chains have a higher motional amplitude in the NHT galleries compared to their state absorbed by silica particles.

Poly(ethylene oxide)/Silica Nanocomposites

This study examines the dynamics of polyethylene oxide (PEO) in a confined environment near spherical nanoparticles using proton low resolution as well as proton and carbon magic-angle spinning (MAS) NMR spectroscopy. The focus is on understanding how the adsorbed polymeric interphases behave on the surface of amorphous silica. The study characterizes a reduced-mobility component of the PEO and investigates how preparation parameters such as polymer molecular weight, NP size, shape, surface, and NP-polymer interaction can affect it. The aim is to understand how these parameters can be varied and controlled to tune the dynamic processes of polymer melts in these hybrid materials. We also delve into a thorough exploration of the internal dynamics of PEO chains within a confined interfacial layer. An intriguing aspect of our investigation is the remarkable NMR transverse relaxation time of confined PEO chains, which exceeds 10 to 20 μs, the range usually associated with the rigid fraction. Since our measurement temperature is above T_m, we are already in the fast motion limit, therefore this T_2 only relates to an anisotropy caused by motional restrictions imposed by silica nanoparticles.

6.1   The effect of initial dispersing solvent

Formation of PNCs requires a series of dynamic processes including dispersion in solvents, mixing with polymers, evaporation of solvents, and drying. The samples used in this study were produced by our collaborators in Korea. Here we are using samples with 40 nm silica particles with volume fractions of 0.05 and 0.5 dispersed in either ethanol or water as two different casting agents and mixed with PEO of 3 and 20 kg/mol [24].

To study the microstructures of particle dispersions, our colleagues used Small-angle X-ray scattering (SAXS). Analyzing the scattering intensity using particle form and structure factors, gives us information on interparticle correlations. The SAXS results showed a significant change in particle dispersion for systems with different initial dispersion solvents, even though the solvent was evaporated in the last step [24,81,129]. The nanoparticle structure factors, $S(q, \phi_c)$, which described correlations between the particles, were obtained by dividing the scattering intensities of the concentrated particle suspension and the diluted particle limit by the same high polymer level in which the nanoparticles are stable. All experimental structure factors show an amorphous liquid-like peak with a plateau value at low qD and a large angle that increases in amplitude and moves to larger qD as the volume fraction is increased.
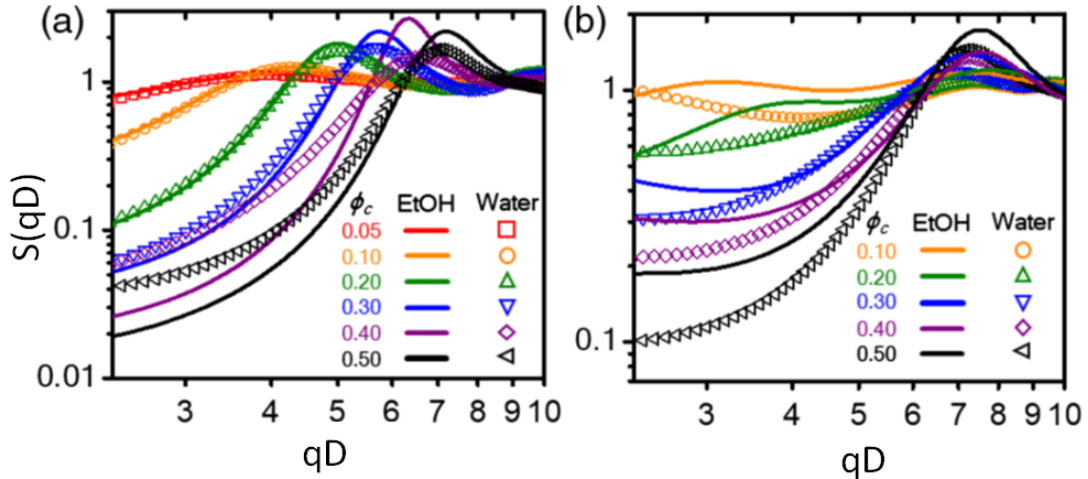

Figure 6.1. The structure factors of silica nanoparticles in PNCs vs. qD for PEO molecular weights of (a) 0.4kg/mol and (b) 20 kg/mol, where D is particle diameter. Reprinted from [24] with permission from American Physical Society.

The positions of the peaks in the sample's scattering patterns changed slightly with increasing silica content, suggesting a decrease in the average distance between the particles [140]. The samples that started with ethanol had higher peak heights, indicating better-ordered nanoparticles compared to those started with water. The difference is even more pronounced in samples with higher silica content. The results showed that the systems become less compressible and more ordered with increasing silica volume fraction. The ethanol systems showed better dispersion and stability, with stronger repulsive interactions between nanoparticles, compared to water-

started systems. As shown in Figure 6.1, for the silica contribution of 0.1 and 0.2 in ethanol started sample, the appearance of two peaks is obvious, while the same samples with initial water solvent have shown only one correlation peak. This means the ethanol systems formed multiscale structures, while water-started systems showed loosely packed nanoparticle networks [140]. With an increase in the volume fraction of nanoparticles, the ethanol-started samples showed the formation of fractal-like aggregates with more stable particle networks, shorter interparticle spacing, and stronger interparticle coherence.

As reported in some previous studies [26,27,73], the different processing pathways of polymer nanocomposites can lead to non-equilibrium effects that affect the final structures and properties of the PNCs despite having the same final compositions and components. Solvent casting is a widely used method for manufacturing PNCs, involving dispersing and drying the solvent, but this approach frequently results in nonequilibrium PNCs. Polymer/particle dynamics in PNCs can experience significant deceleration, leading to a failure to reach equilibrium within experimentally accessible processing times. Thus, here the solvent is the driving force for the non-equilibrium state. This can have important consequences in physical processes, as it can drive the system towards a more energetically favorable state. Depending on the initial solvent, the nanoparticles exhibited significantly different microstructures and dispersion states. This effect could be due to different solvent-particle and solvent-polymer interactions in the initial dispersion states. Since the completely different evaporation rates of EtOH and water can affect the dispersion of nanoparticles in PNCs, both solvents were allowed to evaporate at similar rates by changing the temperature and pressure of the vacuum oven.

Since the mobility and conformation of polymer chains are restricted at interfaces, the change in polymer dynamics close to nanoparticle surfaces is thought to cause this non-equilibrium effect. Therefore, we investigate how this difference in the initial dispersant, which is supposedly absent in the final state of PNCs, affects the interfacial layer, which, as mentioned earlier in Chapter 2, is defined as the region where the properties of the polymer change. These changes can be in density, relaxation time, mechanical properties, and other factors [23,31,32]. To study the segmental dynamics in these systems and quantify the domains of different polymer mobilities, we employed high field ^{1}H NMR experiments, specifically with a 200 MHz Bruker Avance

III spectrometer which features a short dead time of only 2.5 μs and utilizes a 5mm
Bruker static probe rather than relying on a low field system with tens of megahertz
Larmor frequency. This decision was predominantly influenced by the nature of our
samples. The samples we worked with had a low abundance of components with high
dipolar coupling. A low field system typically possesses a dead time of about 12-15
μs, which can potentially decimate these low-abundance, high-dipolar-coupling com-
ponents further. All FIDs were restricted to an acquisition time of 200 microseconds.
This limit was imposed because, beyond this time frame, the effects of field inhomo-
geneity and sample susceptibility begin to distort the signal, making it challenging
to achieve accurate fitting [36]. The results have shown that samples prepared with
ethanol have slightly more polymers trapped near the surface as shown in Figure 6.2
as the effect of the initial solvent for the same samples at different molecular weights.
The molecular weight effect is discussed later in a separate section.
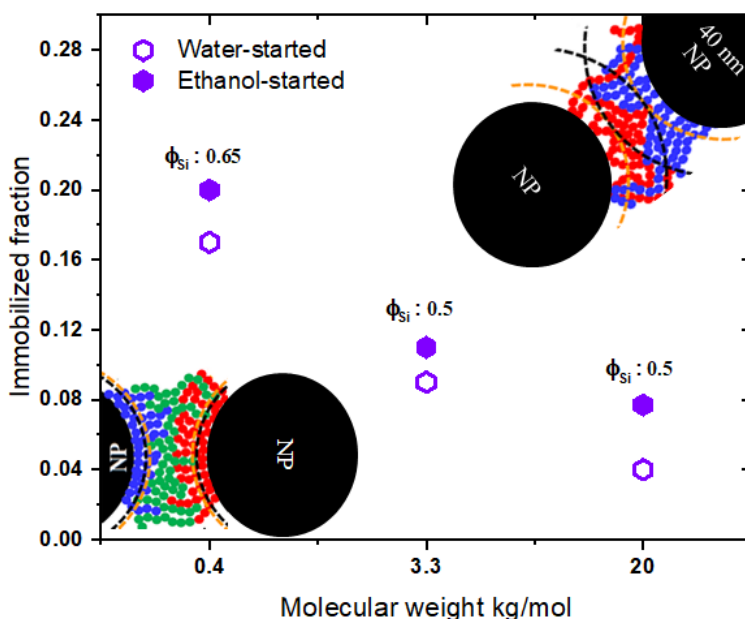
Figure 6.2. Immobilized polymer fractions as a function of MW in ethanol-and water-
started PNCs with closed and open symbols. The schematics included herein represent
the chain packing of low and high MW PNCs. The black and orange dash lines indicate
the height of the loops and the thickness of the dynamic interfacial layer and have been
reproduced from the work of Cheng et al. [17] with permission from American Physical
Society.

It's important to mention that before conducting the NMR experiments, we ac-

counted for PEO's tendency to retain moisture. Consequently, some samples were evaluated in their received state and after drying in a vacuum oven. The resulting data were analyzed using a composite of exponential functions, as previously detailed in the NMR chapter. A significant change is evident in the 0.4k PEO samples after drying, as seen in Figure 6.3. This remarkable change could potentially be attributed to these samples undergoing a longer storage duration in contrast to those with higher molecular weights. As explored in the preceding chapter, our model of layered nanocomposites demonstrated minimal alteration in the total immobilized fraction, with water acting as a plasticizing agent, thereby enhancing the segment dynamics. However, in the present context, drying appears to substantially augment the volume of rigid polymer on the surface. This effect is particularly evident in samples prepared with low molecular weight, whereas freshly prepared high molecular weight samples exhibit negligible modification.

It should be noted that considering this water uptake issue, all the samples under investigation in this chapter were subjected to a drying process in a vacuum oven at a temperature of 75 °C for 24 hours and then followed by an immediate sealing process. It's important to highlight that all measurements also were conducted at a temperature of 75°C, which is beyond the melting point of PEO.
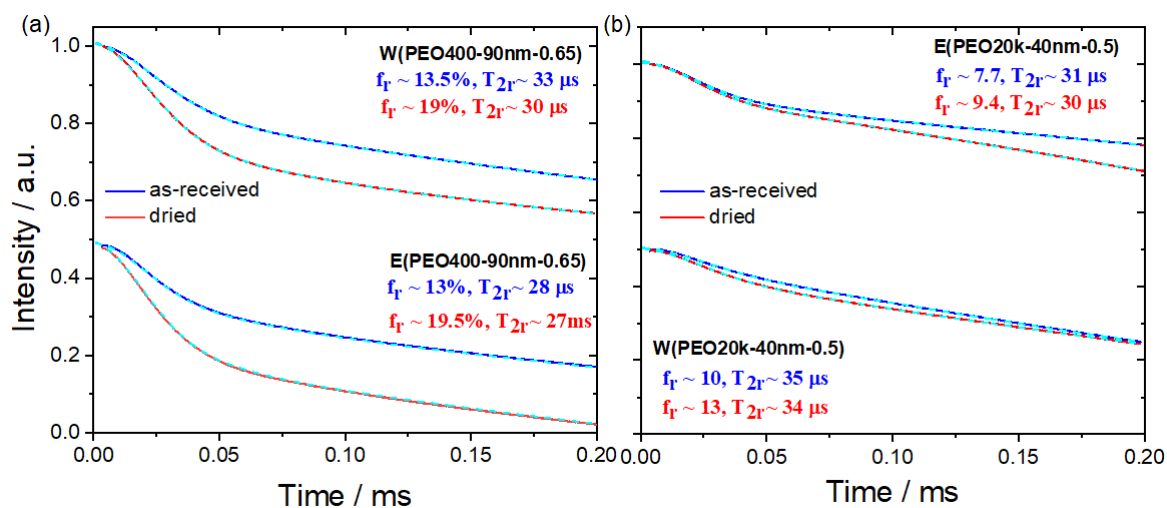

Figure 6.3. Comparison of ambient-hydrated and dried highly filled samples with PEO 0.4k (a) and PEO 20k (b) based on ^{1}H FID measurements at 200 MHz and 75°C.

Looking at the summarized results of rigid relaxation time values ranging from 27 - 35 μs in Table 6.1, one quickly recognizes that this value is much longer than

one would expect for the quasi-rigid polymer as already reported in the recent study within our research group by Golitsyn et al. [22]. These additional complications arise as the adsorbed PEO segments in the form of tails and loops on the silica locally exhibit considerable internal mobility. Although here we have used the word immobilized in reference to this component, it means adsorption at the molecular level, and should not be incorrectly interpreted as complete inhibition of mobility at the level of the whole macromolecule and not a completely glassy or dead layer. Later we will study the time scale of this internal motion in this adsorbed PEO layer.

Table 6.1: Comparison of a series of samples: as received and after drying.

$MW_{vol\%}/D_{SiO2vol\%}$	state	initial solvent	immobilized	Relaxation time
$PEO0.4k_{35}/40nm_{65}$	as received	water	12%	$33\mu s$
$PEO0.4k_{35}/40nm_{65}$	dried	water	17%	$31\mu s$
$PEO0.4k_{35}/90nm_{65}$	as received	water	13.5%	$33\mu s$
$PEO0.4k_{35}/90nm_{65}$	dried	water	19%	$30\mu s$
$PEO0.4k_{35}/90nm_{65}$	as received	EtOH	13%	$28\mu s$
$PEO0.4k_{35}/90nm_{65}$	dried	EtOH	19.5%	$27\mu s$
$PEO0.3k_{50}/40nm_{50}$	as received	EtOH	10%	$30\mu s$
$PEO0.3k_{50}/40nm_{50}$	dried	EtOH	11%	$30\mu s$
$PEO0.20k_{50}/40nm_{50}$	as received	Water	10%	$35\mu s$
$PEO0.20k_{50}/40nm_{50}$	dried	Water	13%	$34\mu s$
$PEO0.20k_{50}/40nm_{50}$	as received	EtOH	7.7%	$31\mu s$
$PEO0.20k_{50}/40nm_{50}$	dried	EtOH	9.4%	$30\mu s$

To determine the thickness of the interfacial layer on the surface, we measured the immobilized polymer fractions,$f_{immob.}$, for a series of samples with two different particle sizes, 40 and 90 nm, and volume fractions of 0.2 and 0.5 and using water and ethanol as two different dispersing solvents. The fit results are shown in Figure 6.4 as a function of the silica-specific inner surface (total silica surface area per unit volume) with D being the silica diameter and Φ_{SiO_2} the silica volume fraction to reach the estimated thickness of the interfacial layer δ:

$$f_{immob.} = \frac{\phi_{immob.}}{\phi_{polymer}} = \frac{\dfrac{1/6\pi(D+2\delta)^3 - 1/6\pi D^3}{V_{total}}}{1 - \phi_{SiO_2}}$$

$$= \frac{\dfrac{1/6\pi(D+2\delta)^3 - 1/6\pi D^3}{(1/6\pi D^3)/\phi_{SiO_2}}}{1 - \phi_{SiO_2}}$$

$$= \frac{(8\delta^3 + 12\delta^2 D + 6\delta D^2)\phi_{SiO_2}}{(1 - \phi_{SiO_2})D^3}$$

$$= \frac{2\phi_{SiO_2}}{(1 - \phi_{SiO_2})}(4\frac{\delta^3}{D^3} + 6\frac{\delta^2}{D^2} + 3\frac{\delta}{D})$$

By neglecting the two higher-order terms, we have :

$$f_{immob.} = \delta \frac{6\phi_{\mathrm{SiO_2}}}{D(1 - \phi_{\mathrm{SiO_2}})}$$

Therefore at this high enough temperature of 75°C at which we did the measurement, the slope of the linear fit of the immobilized polymer fraction data versus the silica-specific surface gives an approximate thickness of the interfacial polymer layer around the silica particle.

It can be seen that, in agreement with what has been said so far, a thicker interfacial layer was observed for samples with ethanol as the initial solvent. Furthermore, we see again that for the same silica-specific surface area, the samples that started with ethanol contained more immobilized polymer than the samples with water as the initial solvent. Thus, in conclusion, we can say that preparing PNC from ethanol leads to a better packing of chains in the interfacial layer and to the formation of a thicker interfacial layer. Possible nonpolymeric contributions [141] such as the Si–O–Et units that can be formed during drying, Si-OH, and residual water and ethanol in the system will be discussed further.
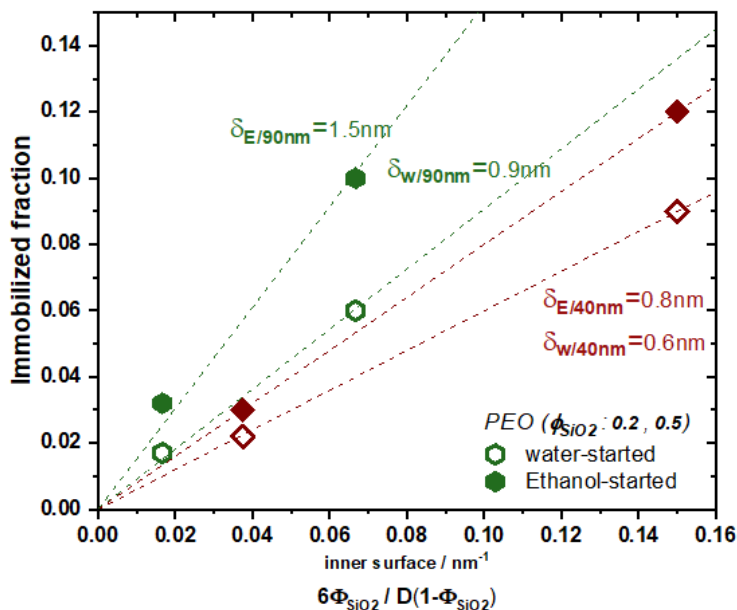
Figure 6.4. Fraction of immobilized polymer as a function of the silica-specific inner surface. A linear fit of the points is shown for each set of samples. The slopes of these curves indicate the approximate thickness of the interfacial layer. Filled markers for samples started with ethanol and open markers for samples started with water.

6.2   Effect of water and ethanol content

In our study of the time scale of samples, we utilized measurements of 400 MHz and observed the presence of peaks corresponding to water and ethanol in the spectra. This finding was contrary to the assertions made by our colleagues in Korea, who claimed that the solvents used in the process were fully removed from the final samples. However, the residual water and ethanol are still present, which means that the non-polymeric contributions of Si-O-Et and Si-OH to our FID signal are very likely. To better understand the contribution of residual water and ethanol in silica samples, a series of test experiments were conducted. The goal was to determine how large this contribution is and if these residual amounts of water and ethanol were tightly bound to the silica surface or if they were free. To accomplish this, a set of PNCs samples and also same size pure silica as reference samples were chosen.

A weight-controlled experiment was performed to ensure that the same weight of silica was used in the MAS rotor for both the PNC sample and the reference pure

silica sample. This allowed for a direct comparison of NMR spectra if the experiment detection conditions were consistent. This comparison is never fully quantitative but we could at least estimate how much ethanol and water are from the synthesis of silica.

The first set of check samples consisted of 0.65 volume fraction of 40 and 90 nm silica particles in a 0.4k PEO matrix, in both water and ethanol starting series as well as reference samples of pure silica in sizes of 40 and 90 nm and at the same concentration as the composite. The ^{1}H NMR spectra for all selected samples were recorded, both as received and after drying and sealing. The Hahn Echo rotor synchronization was also applied, where the delay between the $\pi/2$ and π pulses was set to an integer multiple of the rotor period. The spectra results showed that both the 40 and 90 nm particles contained residual ethanol, with higher amounts in samples that started with ethanol. Water and Si-OH bonds were also present and did not completely leave the sample even after drying for 1-2 days at 80°C in a vacuum oven. Only the main bulk water peak at 4.76 ppm disappeared, but a broad signal distribution remained over the entire ppm range, which is known to be attributed to inhomogeneous binding site distribution [141, 142]. Figure 6.5 provides an illustration of the test series and highlights the presence of residual water and ethanol in the samples.
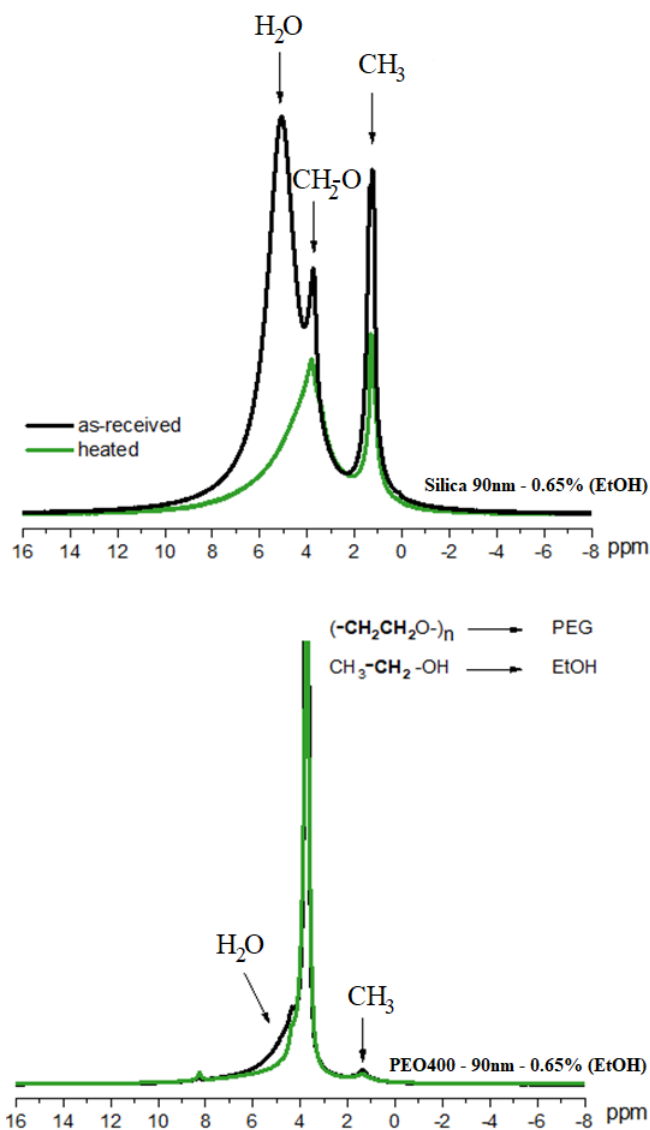
Figure 6.5. ^{1}H-MAS spectrum of 65 vol% pure 90 nm silica (top), and related composite PEO3k-90nm-65 vol% (bottom), both ethanol started, with signal assignments.

To estimate the amount of ethanol and water in the composite sample, we calculated the integral of resonances of the PNC and silica paste of equal weight in the polymer matrix. By comparing the peak integration of the PNC and silica paste, we could roughly estimate the amount of signal due to silica particles in the composite. In practice, determining the exact beginning and end of the integration range can be challenging, and the ratios obtained from peak integration are not always the exact whole numbers. It is also important to mention that maintaining a stable dry state in

samples with MAS rotors can be challenging due to the caps not being fully tightened.

Results showed that even after drying the sample, approximately 57% of the signal from pure silica synthesized in ethanol still originates from residual water and the remaining 43% comes from ethanol. A similar ratio was observed for the pure silica sample synthesized in water, with 60% coming from residual ethanol and 40% from water. In the case of the composite sample, CH_2 of ethanol and PEO both resonances at about 3.6 ppm, thus if we get the integral of three protons from CH_3, 2/3 of this value is also part of the big PEO+CH_2 peak at 3.6 ppm and should be subtracted from this value. By doing so, we will have the total proton values of ethanol and PEO in the composite sample. By determining the integral value of the entire spectrum, we can gain the proton ratio of each component present in the sample as a whole. It was determined through the calculations of the selected samples that the composite sample with 65 vol% of 90 nm silica content showed 7% of ethanol and 20% of water contributing to the total signal. On the other hand, about 70% of the signal was found to be related to protons in PEO, with only a small fraction of about 3% corresponding to impurities appearing at around 8 ppm.

To determine the proportion of the composite signal that is attributed to silica particles, the same samples were analyzed using a 200 MHz static spectrometer. The free induction decay of the composite sample and its related pure silica particle was measured and analyzed. The FID measurement provided information on the fraction of rigid and mobile or intermediate components.
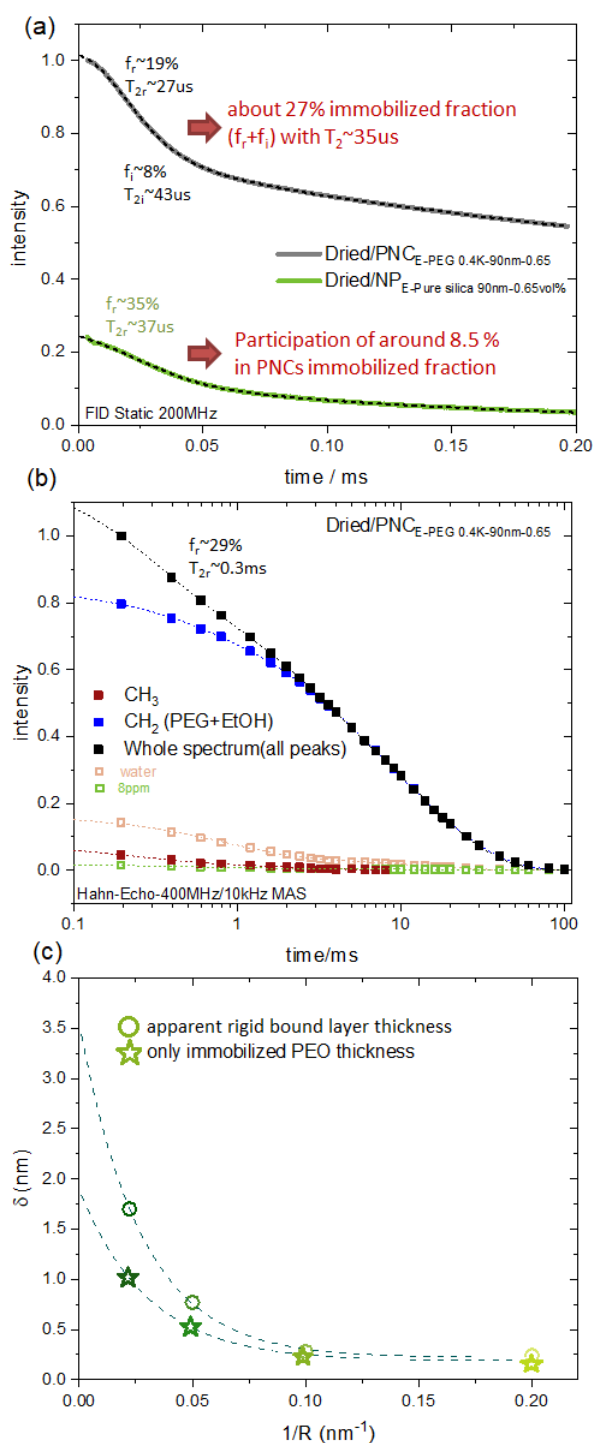
Figure 6.6. a)FID and b)Hahn-echo decay of all individual resonances in ^{1}H-MAS spectrum of PEO0.4k-90nm-65vol% and c) total immobilized layer thickness and only PEO adsorbed layer thickness vs. particle radius for series of samples with PEO 0.4 and particle diameter from 10 to 90 nm and 0.3 to 0.65 volume fraction contribution in ethanol started sample.

For a dried PNC sample with 65 vol% silica and 90 nm diameter that was synthesized in ethanol, the FID data indicated that out of 27% of the immobilized fraction ($f_r + f_i$) of the PNC, 8.5% came from the contribution of ethanol or water that was bound to the silica (Figure 6.6a). A similar result was obtained for the sample that was synthesized in water, which showed that nearly 10% of the total immobilized fraction (30%), was attributed to silica.

To gain insight into the contribution of water, alcohol, and polymer in each fraction, the rotor-synchronized Hahn-echo pulse sequence at 400 MHz and under a spinning frequency of 10 kHz was utilized. As shown in Figure 6.6b, this allowed for the decay of each element to be fitted by using different peak projections. Thus Hahn-echo decays were obtained for the entire spectrum and at the corresponding peaks. The obtained data were fitted by a combination of exponential functions. The results of the Hahn-echo decay measurement and fitting revealed that ethanol made up 8-10% of the total fraction with slowed mobility in the selected PNC sample.

As can be seen from Figure 6.5, the water peak is so broad and not clearly distinguishable therefore we can only rely on individual peaks of CH_3 and CH_2 groups. Although the exact rigid and mobile fractions of water are not reliable due to the uncertainty of the projection region of this broad water resonance, this ratio clearly shows that almost all of the remaining water is attached to the surface. This is also evident for the impurity peak at 8 ppm. The complete MAS-Hahn echo and static FID fitting results of the two totally similar composite samples, one started with ethanol and the other with water, are shown in Table 6.2 and 6.3, respectively.

Table 6.2: Fitting results of rotor-synchronized Hahn-echo decays and integration of each peak appearing in the spectrum for the water-started and ethanol-started samples.

							W(PEO400-90nm-0.65)
	Whole	CH_2	CH_3	H_2O	8ppm	EtOH	PEO
A_0	1						
fr	0.36	0.108	0.064	0.194	0.035	0.106	0.065
fi	0.115	0.12	0.023				0.12
fm	0.53	0.48		0.04	0.005		0.48
T_{2r}	0.35	0.2	0.2	0.76	0.4		
T_{2i}	2.7	3.35	5.06				
T_{2m}	44.13	46.1		49.25	157.8		
							E(PEO400-90nm-0.65)
A_0	1						
fr	0.23	0.067	0.04	0.18	0.034	0.067	0.04
fi	0.09	0.016					0.016
fm	0.68	0.63	0.01	0.03	0.002		0.63
T_{2r}	0.26	0.17	0.26	0.74	0.4		
T_{2i}	1.86	2.95					
T_{2m}	9.9	9.7	9.2	16.7	41		

Table 6.3: Fitting results of static FID, along with peak integration.

W(PEO400-90nm-0.65)

	static		Integral
A_0	1	Whole	1
f_r	0.19	8 ppm	0.04
f_i	0.11	CH_3	0.0865
f_m	0.7	EtOH	0.14
T_{2r}	0.03	H_2O	0.23
T_{2i}	0.053	PEO	0.64
T_{2m}	0.8		

E(PEO400-90nm-0.65)

	static		Integral
A_0	1	Whole	1
f_r	0.19	8 ppm	0.0323
f_i	0.077	CH_3	0.481
f_m	0.733	EtOH	0.08
T_{2r}	0.027	H_2O	0.2075
T_{2i}	0.045	PEO	0.7121
T_{2m}	0.72		

By applying the same process for a series of a sample of the same short molecular weight of PEO 0.4 with different particle sizes from 10 to 90 nm and 0.3 to 0.65 volume fraction contribution in ethanol started sample, it was observed that the thickness of the adsorbed layer increased with the size of the particle even after subtracting the non-polymeric portion of the adsorbed layer. This result is shown in Figure 6.6c. It is important to note that the rigid and intermediate fractions in the MAS probe are related to T_2 values ranging from 0.3 to 2 ms, instead of the typical 25-100 μs in static probes, and the mobile fraction is clearly separated with T_2 values beyond 10 ms.

By analyzing these four different samples, two pure silica and two composite samples made of the same silica particles but with different primary solvents, we were able to determine that about 7-10% of the total immobilized fraction in the sample is due to the silica nanoparticles. The residual amounts of ethanol and water in the sample were found to be tightly bound to the surface and not free.

It is worth mentioning that the comparison between the pure silica paste and the composite samples may not be accurate as the neat silica paste definitely contains more water and excess ethanol than the composites. In pure silica, the entire particle surface is available for the reaction with water and ethanol, whereas, in composites, the PEO chains compete for surface bonding, which could lead to a reduced amount of water and ethanol. Additionally, it was observed that drying the samples resulted in some loss of PEO signal, which further complicates the analysis. Therefore, to overcome these limitations, another series of experiments were performed with PEO with higher molecular weight.

It should be noted that our results from high-field MAS measurements showed a higher fraction of immobilized material compared to those obtained from static methods. This discrepancy is believed to be due to susceptibility artifacts. Magnetic susceptibility is a measure of a material's ability to be magnetized in response to an external magnetic field and can have a significant impact when there is a difference in magnetic susceptibility between the polymer matrix and the reinforcement. In high-field NMR spectroscopy, susceptibility-induced artifacts can be especially pronounced. According to Wapler et.al [143], the difference in susceptibility between polymers and SiO_2 is in the range of 2 to 3 ppm, which results in a frequency shift of 40 to 60 Hz when measured using Minispec and about 1000 Hz when measured using 9.4 T magnets. This difference in susceptibility would be negligible at Minispec but can

cause additional decay in the sub-millisecond region in high-field MAS measurements, leading to an overestimation of the rigid fraction of the immobilized material.

To further understand the amount of non-polymeric surface adsorption, a new set of experiments was conducted using samples with PEO3k. In addition to the previously applied Hahn-echo rotor synchronization method, the spectrum was also recorded at a prolonged Hahn echo delay of approximately 3ms to capture only the mobile signals. The idea is based on the fact that the width of the MAS line is much larger for the rigid fraction.
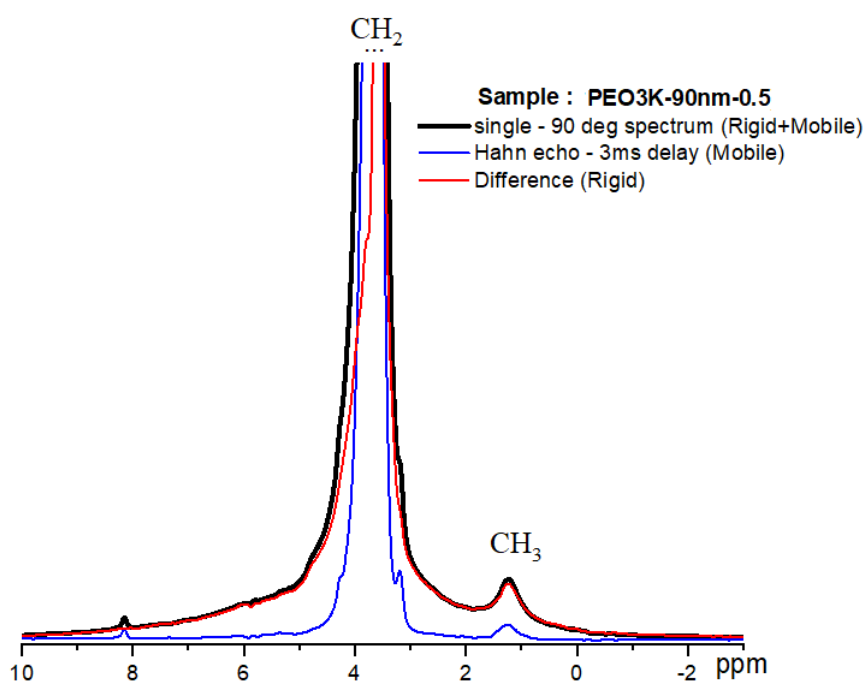

Figure 6.7. Representation of subtracted almost total mobile component from the whole spectrum to highlight the most rigid part of the spectrum.

The mobile component is subtracted from the single 90° spectrum. The subtracted spectrum was scaled to physically reasonable values, resulting in a spectrum of the fairly rigid fraction, as demonstrated in Figure 6.7 for the sample of PEO3k-90nm-0.5. This process was stabilized by applying a specific degree of Gaussian multiplication, which introduced some additional artificial line broadening to all spectra during processing. This allowed for a clearer differentiation between mobile and intermediate signals. These results again showed that roughly 75% of the signal originated from PEO. The result of this procedure for two samples is given in Table 6.4 which shows

the rigid fraction of all seen resonances in the spectrum.

Table 6.4: The contribution of each of the surface adsorbed factors in sample PEO3K-90nm-0.5 with both water and ethanol as initial solvent. 'total' represents the total immobilized fraction in the sample. The percentage values represent the contribution of that particular material to the total immobilized fraction.

	W(PEO3K-90nm-0.5)	**E**(PEO3K-90nm-0.5)
total	0.27	0.27
8ppm	$0.0066 \sim 2.4\%$	$0.006 \sim 2.2\%$
H_2O	$0.06 \sim 22\%$	$0.05 \sim 18.5\%$
CH_2	0.195	0.22
CH_3	0.009	0.02
PEO	$0.19 \sim 70\%$	$0.2 \sim 75\%$
EtOH	$0.014 \sim 5\%$	$0.03 \sim 11\%$
Total rigid fraction from Static probe	~ 0.08	~ 0.1

Based on the analysis of the data obtained from the experiments, it has been determined that the quantity of ethanol adsorbed onto the surface of PNCs is not constant and can vary from one sample to another. However, a general trend that can be observed is that the quantity of PEO bound to the silica surface is slightly greater in PNCs prepared from ethanol as compared to the water-started sample. It is worth noting that water still contributes significantly to the surface and the level of contamination (8ppm) in the samples was found to be very low.

Thus after conducting these series of tests aimed at discerning the relative contributions of water, ethanol, and PEO to the observed surface adsorption, it was determined that a substantial fraction, approximately 75%, consistently originated from PEO across all tested conditions. To represent the contribution of the rigid fraction purely arise from PEO, a correction factor is employed. The total observed surface adsorption was multiplied by the coefficient of 0.75 to isolate the fraction solely attributable to PEO. This correction served to enhance the accuracy of our results by effectively subtracting the contributions of water and ethanol from the overall surface adsorption. In conclusion, we can say that we have successfully quantified the levels of water and ethanol within the sample and accurately reported the proportion

of these substances that exhibit strong surface adsorption. Although there were initial concerns that the excessive surface layer in ethanol-initiated systems was due to ethanol-water bonding on the silica surface, our results indicate that even accounting for this possibility, the samples prepared with ethanol still have a thicker interfacial layer.

Henceforth, the results have been corrected by subtracting the contribution of EtOH/H$_2$O, and only the immobilized fractions originating from adsorbed PEO are represented in the plotted data.

6.3 The effect of temperature

The stability of adsorbed polymer chains near particles is an important factor to consider, as temperature variations can affect the attraction between the polymer and the particle surface. In order to gain a better understanding of how heating affects the immobilization of polyethylene oxide chains, a study was conducted in which the polymer mobility was examined as the temperature was increased from 75 to 150°C. The study used FID data measured for samples with a molecular weight of 3k and a particle concentration of $\Phi_{SiO_2} = 0.5$ in water and ethanol.

The results of the study, presented in Figure 6.8, showed that heating had minimal impact on the immobilized PEO chains near the silica surface which is also consistent with the findings in previous work by Golitsyn et al. [22]. Despite the temperature increase, the amount of immobilized polymer remained unchanged, as did its motional amplitude. This suggests that the stability of the adsorbed polymer chains is limited by nanoscale forces, which are largely unaffected by changes in temperature. Note that the time scale of existing local motion is for sure changing but is in the fast limit for the ^{1}H dipolar effect studied here.
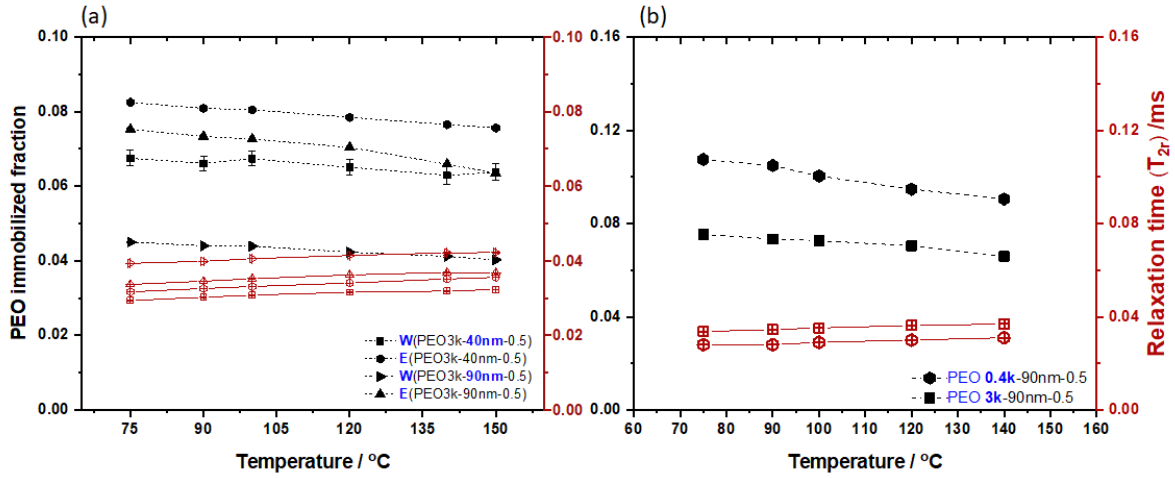
Figure 6.8. Rigid polymer fractions and associated relaxation time as a function of temperature (a) in PNCs started with ethanol and water (b) with different molecular weights in ethanol-started samples.

These minor changes observed in the stability of the adsorbed polymer chains near particles in response to temperature increases can be attributed to thermal expansion, which amplified low-amplitude local oscillations. However as highlighted in Chapter 2, numerous systems including our recent collaborative research with the Baeza group [43] on poly-2-vinyl pyridine and silica nanoparticles have observed a notable temperature dependence in both the immobile fraction and relaxation parameters [43, 54, 62, 63, 144]. They have shown that with rising the temperature, the thickness of the polymer layer absorbed on the particle surface decreases. Indeed, the temperature somehow has eliminated the confinement effect and this is associated with the increase in the glass transition temperature.

In this regard, recent models attributed the increase in glass transition temperature to faster dynamics as a result of having more free volume which causes the reduction of mean relaxation time and its distribution. This confirmed the existence of a T_g gradient around solid particles and shows the simple core-shell approximation no longer holds in such cases. The core-shell approximation refers to a simplified theoretical model for describing the T_g gradient around solid particles. This model assumes that the glass transition temperature distribution around the particle is a simple two-layer system, with a constant T_g difference between the core and the shell. This model speculates that the close connection between structure and dynamics in

the adsorbed layer was a result of the monomer density at the polymer/substrate interface, which acted as a local free volume and altered the structural dynamics, therefore affecting T_g. Based on this idea, an increase in free volume, caused by factors such as packing frustration, also may lead to an acceleration of segmental dynamics and thus explain the increase in T_g, even when slower dynamics caused by chain adsorption are present [52].

Our observations align with the hypothesis that alterations in the free volume content at the polymer/particle interface serve as the molecular basis for the correlation between T_g and the adsorbed polymer quantity, although the PEO/SiO_2 nanocomposite shows no heat-induced softening and lacks a noticeable gradient in its glass transition temperature for unknown reason, it distinguishes itself from other polymer nanocomposites in similar scenarios. Put differently, the rise in glass transition temperature is directly linked to the polymer adsorption process occurring on the particles' surface. This process undergoes variation as the distance from the surface varies. This relationship has been qualitatively tested and confirmed by Napolitano et al. [52] and it has been shown, that the time evolution of the glass transition temperature followed the adsorption kinetics, meaning that as the quantity of polymer absorbed onto the particle surface changes, the glass transition temperature also changes in a correlated manner. Thus, the thickening of the interfacial layer near particles at the polymer/particle interface in our system results in a reduction of local free volume, which restricts the conformations of the polymer chains and leads to a very high glass transition temperature. The stability of the adsorbed polymer layer is not affected by temperature changes, and the polymer chains remain firmly attached to the particle surface, indicating that the adsorption is long-lasting and durable [28, 63, 145].

Moving forward, our focus is on studying the internal mobility present in the most immobilized component of our sample. As a result, we require samples that contain a higher proportion of this component. This leads us to the decision to use samples that began with ethanol, as these consistently demonstrate a higher presence of the immobilized component in question.

6.4   Molecular Weight Dependence of Interfacial Interactions

Having presented the stabilized polymer fractions as a function of MW for ethanol-and water-started PNCs in Figure 6.2, and recognizing the superiority of samples prepared with ethanol, as well as observing the decreasing trend in the fraction of the interfacial polymer layer on the surface with increasing molecular weight, Figure 6.9 shows how the thickness of the interfacial layer is affected by the different length of the PEO chains. The diameter of silica particles in all selected samples is 40 nm with a share of 0.2 to 0.5 volume fraction. The molecular weight of the polymer matrix plays a crucial role in the resulting interfacial layer thickness. Although the dynamics of the pure polymer are relatively insensitive to changes in molecular weight where the molecular weight exceeds the critical molecular weight, the significant presence of interfaces in PNCs and the relative size of NPs introduce different perturbations depending on the molecular weight of the matrix. The results reveal the increase of the MW from 0.4 kg/mol to 20 kg/mol leads to a decrease in the interfacial layer volume fraction, leading to a reduction in interfacial layer thickness from 0.6 nm to 0.4 nm. This indicates that low molecular weight samples have a stronger imposed perturbation compared to high molecular weight polymers. Evidently, shorter polymer chains more effectively establish a solid interfacial layer between particles. This efficiency stems from their ability to pack more densely onto the surface. In contrast, long chains act as a screening layer and make the surface inaccessible to other segments. This implies that segments shaped like trains, in direct contact with the surface, experience greater monomeric friction compared to loop-shaped segments that dangle away from the surface.
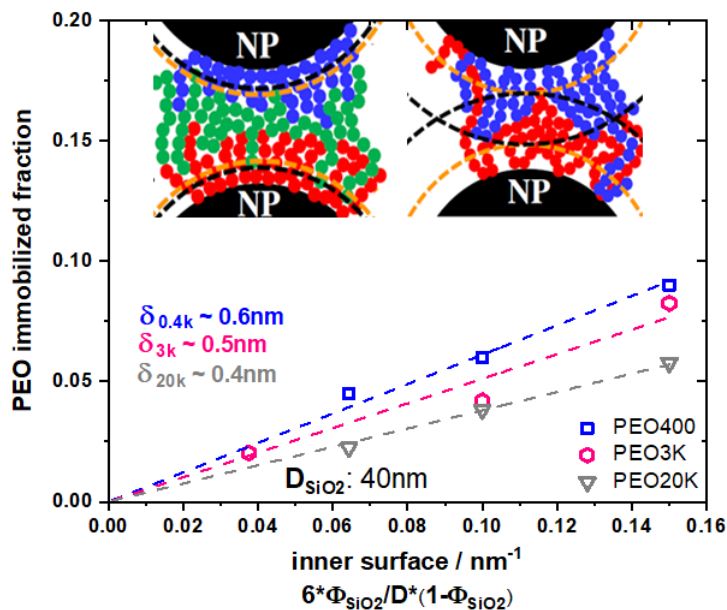
Figure 6.9. The proportion of immobilized polymer with different molecular weights as a function of silica-specific surface area. The schematics included herein represent the chain packing of low and high MW PNCs. The black and orange dash lines indicate the height of the loops and the thickness of the Dynamic interfacial layer and have been reproduced from the work of Cheng et al. [17] with permission from American Physical Society.

Our results underscore the significant influence of molecular weight on the interactions between physically adsorbed chains and nanoparticles. This is consistent with the recent experimental discoveries by the Sokolov group [17, 80]. Their analysis of XPS data revealed a diminished hydrogen bonding between the pyridine rings of P2VP and the NP surface as MW increased. Complementary SFG data further observed a surge in free OH's on the silica NP surface in correlation with rising MW. These insights emphasize the pivotal role molecular weight plays in shaping both structural and dynamical changes at the polymer-NP juncture. However, this perspective challenges certain theoretical models [146, 147] and some experimental studies [148, 149]. These earlier works posited that the thickness of the adsorbed layer grows in tandem with the polymer's increasing MW, directly corresponding to its radius of gyration. This discrepancy could possibly arise from conflating the surface layer with the bound polymer layer [88]. The latter, shaped by adsorbed chains, mirrors Guiselin brushes in character, with its thickness typically matching the polymer's radius of gyration, R_g.

6.5　Particle size and loading

Despite advancements in the study of interfacial regions, a comprehensive under-standing of the parameters that control the structure and properties of this layer is still lacking. One of the outstanding challenges is to determine the impact of par-ticle size and curvature on the interfacial layer. The use of nano-sized particles in a polymer offers a higher surface-to-volume ratio compared to larger fillers, leading to a greater total interfacial area. This makes the interphase between the polymer and the particles critical for affecting properties as it governs the interactions be-tween the two components. However, it is important to note that extremely small particles such as POSS molecules can also have a negative effect and act as plasticiz-ers [103, 150], reducing the intermolecular interactions between polymer chains and causing the polymer to become more flexible and less stiff, ultimately decreasing its properties and performance.

Therefore, the relative amount of filler is an effective factor as it modifies the amount of interface between NP and polymer effectively. The interparticle spacing can be much larger or smaller than the PEO chain size, $2Rg$. Thus, assuming a random distribution of NPs in the polymer matrix, the average distance between the particles is given by [42]:

$$ID = D_{NP}[(\frac{2}{\pi\Phi_{NP}})^{\frac{1}{3}} - 1] \tag{6.1}$$

which expresses the interparticle spacing (ID) as a function of the particle di-ameter (D_{NP}) and the volume fraction of particles in the polymer matrix (Φ_{NP}). Equation 5.1 shows that the interparticle spacing decreases as the volume fraction of particles in the polymer matrix increases, as shown in Figure 6.10. The interparticle spacing is an important factor that affects the properties of the polymer-nanoparticle composite as it determines the degree of confinement of the nanoparticles in the poly-mer matrix. A smaller interparticle spacing leads to a higher degree of confinement and a more significant effect on the properties of the composite.
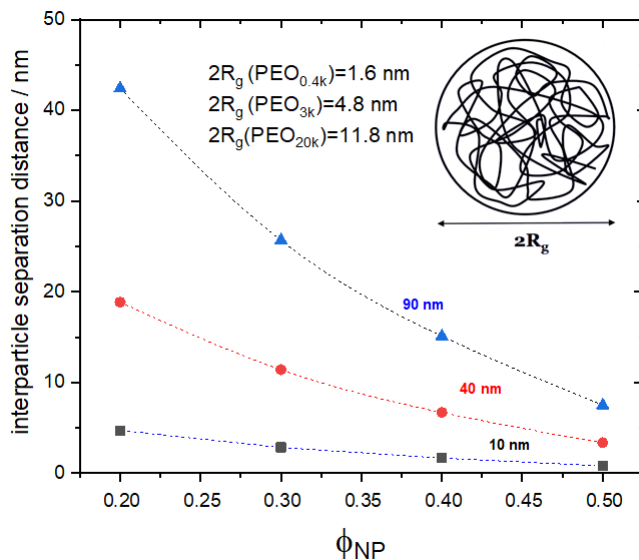
Figure 6.10. Calculated interparticle distance (ID) is plotted as a function of the volume fraction of NP (Φ_{NP}) for systems with three different silica nanoparticle sizes under the assumption that NPs are randomly distributed in a polymer matrix according to eq.6.1

The results of simulations and experiments on the effect of interparticle spacing on the behavior of polymer chains in a polymer matrix filled with nano-particles state that when the interparticle spacing (ID) approaches the chain size ($2Rg$), polymer bridges form between adjacent nano-particles. At ID less than $2Rg$, the system is considered to be in a crowded matrix condition, which means that the polymer chains must undergo significant conformational changes in order to fit between the nano-particles. Thus, as the interparticle spacing decreases further and approaches the Kuhn length of the polymer fragments, all of the polymer chains should be interfacial, as discussed in recent research works [42, 82, 84, 151].

Figure 6.11 shows our experimental results based on NMR measurements of solid polymer fraction versus the volume fraction of silica nanoparticles and the effect of particle size at different polymer molecular weights. The results indicate that the fraction of strongly immobilized polymers increases with increasing volume fraction of nano-particles for all systems, due to the greater surface area of the particles that is available for adsorption of the polymer chains. The effect of particle size on the proportion of solid polymer becomes more apparent as the amount of particles in the matrix increases. Thus, at a constant concentration of 0.5 volume fraction of nano-particles, the fraction of the interfacial layer increased significantly with an increase

in particle size. This implies that larger nano-particles with less curved surfaces will affect more segments of the polymer chains.
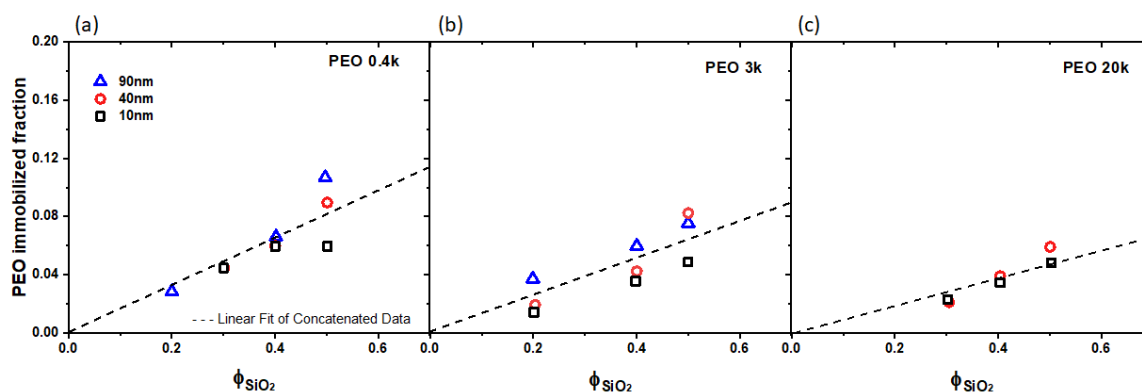

Figure 6.11. The PEO immobilized polymer fraction as a function of the volume fraction of silica nanoparticles at different particle sizes for a)0.4k, b)3k, and c)20k PEO molecular weights.

In Figure 6.12, the fractions of strongly adsorbed polymers are plotted, derived from our fit results, against the specific particle for all ethanol-initiated samples with varying matrix molecular weights (0.4, 3, and 20k), particle diameters (10, 40, and 90 nm), and polymer/particle volume ratios (0.2 to 0.5). By analyzing the slope of the linear fit of this data, the interfacial layer thickness was determined, as described in section 6.1.

These data provide a comprehensive overview of the effects of particle curvature and polymer molecular weight on the thickness of interfacial polymer layers. the effect of particle size on the thickness of the interfacial layer is clearly depicted in this diagram. The formation of a thicker interfacial layer around a less curved surface, as observed in the case of larger particles, highlights the significance of curvature in shaping the structure of the interfacial layer. Furthermore, the results also illustrate one more time the impact of the molecular weight of the polymer on the mass density of the interfacial layer. A noticeable decrease in the thickness of the interfacial layer is observed as the molecular weight of the polymer increases.
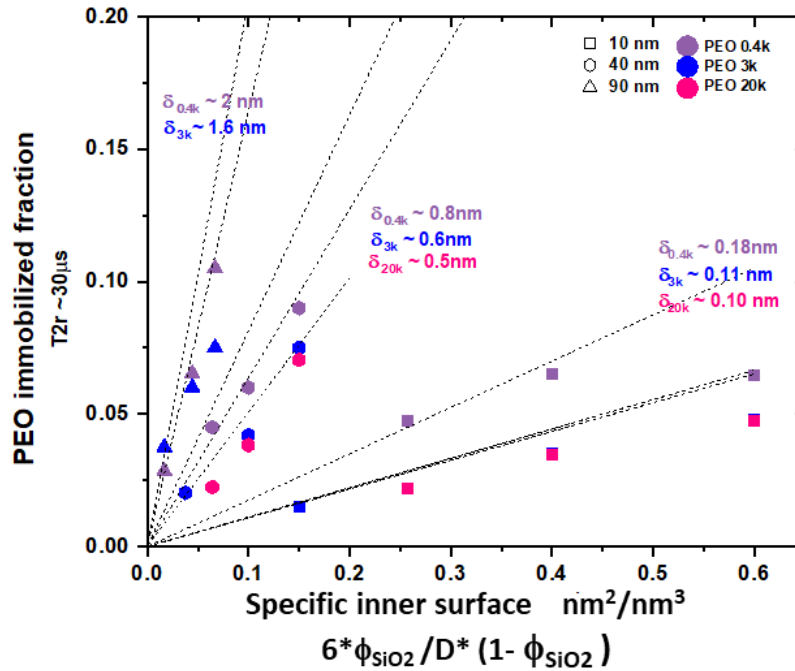
99

Figure 6.12. The fraction of strongly adsorbed polymers as a function of the specific inner surface. The thicknesses obtained by analyzing the slope of the linear fit are given in the diagram.

Figure 6.13 shows the obtained interfacial layer thickness δ for all the PEO/silica nanocomposites, plotted against particle radius at T = 75 °C for samples having R = 5, 20, and 45 nm and all three different polymer molecular weights. It can be seen that δ ranges from 0.1 to 2 nm and in fact increases as R grows. For discussing the effect of particle curvature on the immobilization of polymer segments near a surface, we use a simple assumption that a unit of interface binds a fixed number of segments, regardless of the strength of the curvature, which is supported by previous work of Kumar and Colby [30]. We calculated the thickness of the absorbed layer $(\delta(R))$ based on a given thickness for a flat surface (δ_f), using the equation $\delta(R) = (3R^2\delta_f + R^3)^{\frac{1}{3}} - R$. Note that a flat surface can be assumed when $R \gg \delta_f$. The calculated result gives δ_f in the range of 0.3 for PEO with 20k molecular weight and 1.2 nm for PEO 0.4k which compared to the experimental results, shows a much slower thickness growth with increasing R.
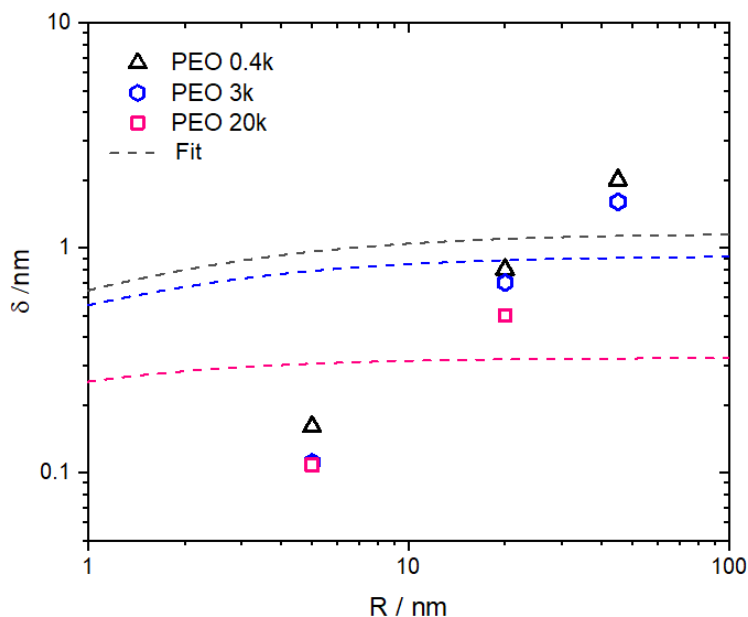
Figure 6.13. Interfacial layer thickness δ as a function of the radius of particle. Dashed line is prediction of equation $\delta(R) = (3R^2\delta_f + R^3)^{\frac{1}{3}} - R$ based on the simple assumption of constant immobilized segment number per unit of the interface.

Our experimental result shows clearly that the increase of δ with R is much stronger than the simple prediction, meaning that a unit area of a more curved surface effectively immobilizes a smaller amount of segments than a unit area of a flatter surface. This is further supported by previous work of Kumar's group [75] that compared the behavior of P2VP films on planar silica substrates as a representation of the ultimate limit of a large particle composite, to P2VP with well-dispersed 15 nm silica nanoparticles via dielectric relaxation spectroscopy and demonstrated that the thickness of the immobilized polymer layer is significantly increased going from a nanoparticle to a flat surface.

The thicknesses (δ) obtained from Figure 6.12 are again plotted in Figure 6.14 this time against $1/R$, the reciprocal particle radius. The density of adsorbed monomer at the polymer/substrate interface can be attributed to the free volume, i.e., space accessible for the molecule to relax, which is thought to be the cause of the high link between structure and dynamics in the adsorbed layer. We believe that the free volume perturbation resulting from chain adsorption should be considered a crucial parameter in describing the deviation of polymer behavior under confinement from bulk behavior. However, intriguingly, an absence of discernible shifts or gradients in

glass transition temperature within the PEO/SiO$_2$ nanocomposite defies conventional expectations, as typically observed in polymer matrices. Notably, there appears to be a unique layer characterized by distinctive confined dynamics. The exact reasons underlying this distinctive behavior remain elusive and warrant further investigation.
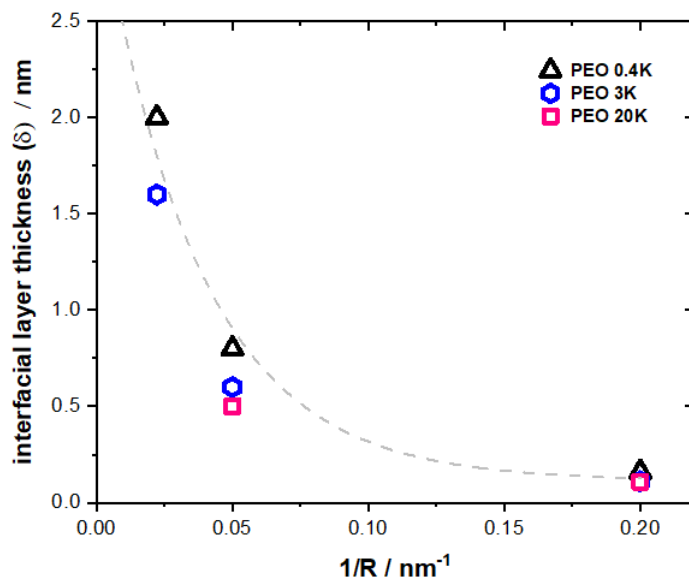

Figure 6.14. Interfacial layer thickness δ against reciprocal particle radius 1/R.

6.6   Time scale of motion

Confinement effects in polymer melts cause unexpected characteristics. Therefore, filling the polymer matrix with particles may change the chain composition and dynamics due to interactions with the filler surfaces. The majority of studies on these microscopic properties are conducted through simulations [152–154]. Only a few experimental works have addressed these properties [155], focusing on the special confined layer formed by PEO/SiO$_2$ where the details of the dynamics are of interest. Our objective is to characterize the rigid layer while also exploring the constrained dynamics within the mobile component. In doing so, we draw comparisons with bulk PEO for a comprehensive understanding of the system.

As previously mentioned, depending on the type of NMR experiments, we can provide information on very fast or much slower motions. ^{13}C NMR relaxation time measurements such as the spin-lattice relaxation time have been used for a long time

to characterize local dynamics in polymer melts [156]. However, quantitative description of molecular dynamics in PEO/SiO_2 polymer nanocomposites with irregular conformations and complex interactions is a challenging task. The implementation of T_1 and $T_{1\rho}$ relaxation experiments holds significant promise for unveiling molecular dynamics with selectivity. As mentioned earlier these experiments capitalize on the sensitivity of relaxation times to the motion of nuclear spins across various timescales. This is achieved through careful adjustment of experimental parameters and utilization of frequency-selective techniques. The choice of radiofrequency pulse sequences, spin-lock parameters, and temperature variations allows for tailored investigations into the dynamics of interest. The spin-lattice relaxation time in the rotating frame, $T_{1\rho}$, allows us to study internal motions in the microsecond time-scale regime. $T_{1\rho}$ measurements extend the correlation time range determined by T_1 in the GHz range to the kHz range, providing a more accurate representation of molecular motion in a wider frequency range.
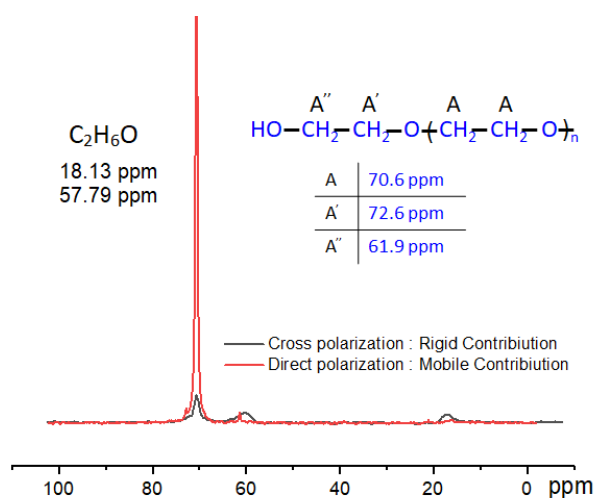
Figure 6.15. ^{13}C DP and CP/MAS NMR spectra of PEO3k-40nm-0.5. The DP spectrum predominantly exhibits signals from the mobile components, while CP assignments are attributed to the rigid components.

Figure 6.15 showcases the ^{13}C cross and direct polarization spectra, corresponding respectively to the immobilized surface layer and the mobile phase. Subsequently, the relaxation decay profiles discerned from these spectra illustrate the separation of contributions arising from the quasi-rigid and mobile components. The ^{13}C NMR experiments were conducted utilizing a Bruker 400 NMR spectrometer operating at a

^{13}C resonance frequency of 100 MHz, employing a 4 mm MAS probe with a spin frequency of 5 kHz. To ensure consistent conditions in the proton system and maintain uniform decoupling efficiency during signal acquisition, the amplitude of the proton RF field, was kept constant within the range of 100-110 kHz. Experimental parameters included a 400 μs CP contact time to accentuate selective polarization of the adsorbed layer, and $\pi/2$ pulse lengths of 3 to 4 μs for carbon and 3 μs for proton channels. For $T_{1\rho}$ three different on-resonance spin lock fields of 13, 23, and 53 kHz were applied at an effective temperature of 87.5°C. Furthermore, the experiment employing a 53 kHz spin lock frequency was repeated at 75°C and 100°C for comparative analysis.
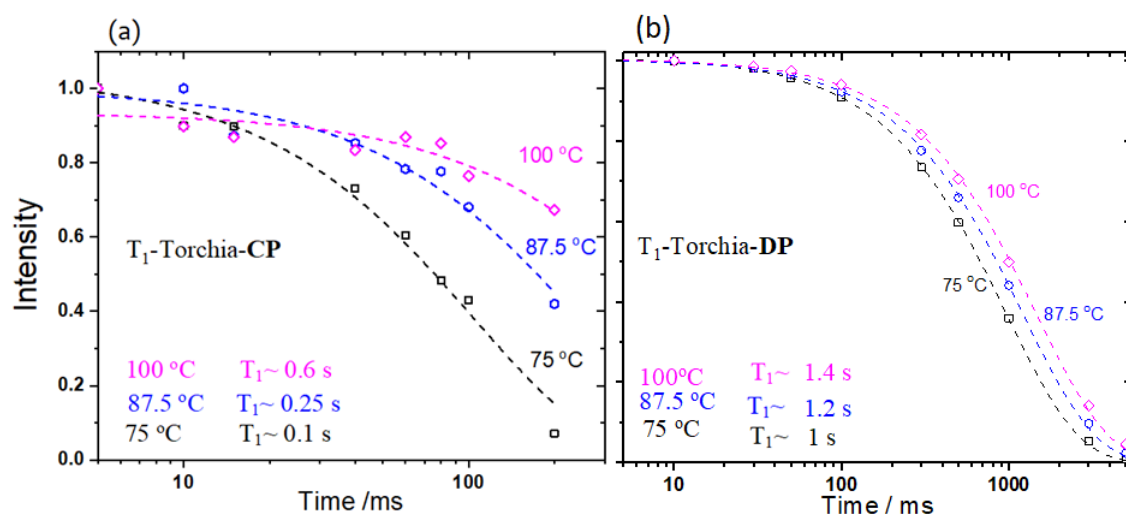

Figure 6.16. ^{13}C T_1 decays of PEO3k-40nm-0.5 at various temperatures, illustrating distinct profiles using a) cross-polarization (CP) with a 400 μs contact time to highlight the rigid component and b) direct polarization (DP) to emphasize the mobile fraction.

Figures 6.16(a,b) show the results of the T_1 cross and direct polarization measurement, which provide the carbon spin-lattice relaxation time for the adsorbed surface layer, and the bulk, respectively which are determined through mono-exponential fitting. The measured results reveal a striking contrast in the T_1 relaxation times between the surface layer and the bulk of the material. This deviation reflects the different motional amplitude and the motional time scale. The so-called immobilized surface layer as a result of CP, exhibits significantly shorter T_1 values, in the order of tenths of seconds, while bulk can be much more dynamic (larger motional ampli-

tude), but it has a shorter correlation time and thus longer T_1 in the range of seconds which is close to the fast (extreme narrowing) limit. The tested samples include pure PEO3k and a PNC sample with a relatively higher interfacial component (compared to the other samples) along with the same molecular weight as the pure matrix, as well as 50% silica nanoparticles with a size of 40 nm. The results of the neat polymer are not depicted in this context.
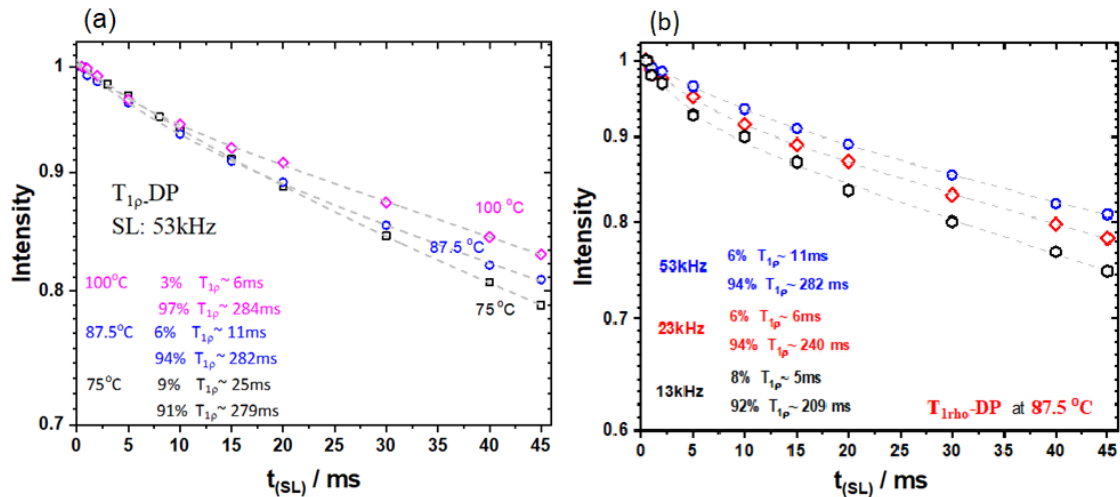

Figure 6.17. ^{13}C direct polarization $T_{1\rho}$ of PEO3k-40nm-0.5 at different a) temperatures and b) spin lock frequencies.

Figure 6.17 presents the measured DP $T_{1\rho}$ relaxation decays at different temperatures and spin lock frequencies. These relaxation decays have been analyzed using both mono- and bi-exponential fitting functions $\propto exp(-t_{SL}/T_{1\rho})$. It is noteworthy that a fraction exhibiting a shorter $T_{1\rho}$ (closer to the $T_{1\rho}$ minimum) is present. Since this short $T_{1\rho}$ gets shorter upon heating (as opposed to the CP-based results for the rigid layer in Fig. 6.19), we attribute it to a more confined part of the mobile fraction. The temperature dependency of the T_1 and $T_{1\rho}$ data mentioned above is illustrated in Figure 6.18. These data are subjected to fitting using correlation function formalism and the model-free approach, as detailed in Section 3.6.4. In cases where T_1 and $T_{1\rho}$ values are derived from biexponential fits, a weighted average of the two values is employed which accounts for the presence of an inhomogeneous population exhibiting significantly distributed dynamics. These dynamics can be described using the classical theories of polymer dynamics. The T_1 relaxation time serves as a probe for the segmental timescale, specifically the alpha process, which remains relatively con-

sistent for every segment along a polymer chain. Only in the middle of the chain is the alpha process somewhat less isotropic. On the other hand, $T_{1\rho}$ investigates slower and longer timescales, during which chain modes, Rouse model, become relevant.

Therefore, we start describing our data with a model composed of a very fast segmental relaxation in picosecond time scale resulting from vibrational motions within the Kuhn segments and a long time tail with nanosecond time scale motion for pure PEO, the latter possibly corresponding to the Rouse modes. For the composite sample, the significant effect of the particles presence in the matrix is clearly established. Notably, certain parts of the polymer chain become absorbed into the particles, leading to a considerable reduction in the chain's overall mobility and shifting it towards a more special confined state with limited capacity for relaxation beyond local regions. Looking at the mean correlation times of the neat polymer matrix and PNC listed in Table 6.5, we can clearly see even with all experiments and fitting uncertainties, the presence of NPs significantly slowed down the movement of the slow component by three orders of magnitude. Achieving a low beta value, approximately 0.5 for the bulk/free chains, represents the distribution of the mode expected for a Rouse chain, while a beta value of 1 for the confined chains is associated with the local intra-segmental motions and surprisingly little or no distribution.
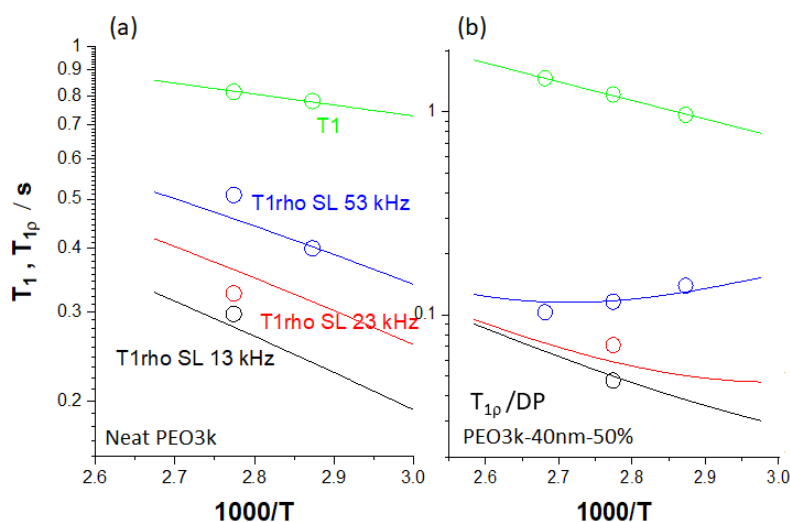

Figure 6.18. The temperature-dependent carbon relaxation times of a) neat PEO 3k polymer and b) mobile component in the PNC. The composite, featuring the same polymer molecular weight as the pure matrix, includes 50 volume percent of 40 nm silica nanoparticles.

Table 6.5: Values obtained for fitting parameters of carbon spin-lattice relaxation data.

Sample	motion	S^2	$\tau(75°C)$	β	E_a
Neat PEO3k	fast	0.001	30 ps	1	4.2
	slow	~ 0	25 ns	0.53	35
DP:PEO3k/SiO$_2$	fast	0.003	23 ps	1	18
	slow	0.0022	6 μs	1	29

Figure 6.19a displays the $T_{1\rho}$ CP data collected at various temperatures, utilizing the highest spin lock frequency among those measured during the experimental procedure. These data points are subjected to fitting with a single exponential function, revealing a slight increase in the $T_{1\rho}$ of the adsorbed surface layer upon heating. Additionally, the results obtained from fitting the CP $T_{1\rho}$ experiment at different spin lock frequency ranges, as depicted in Figure 6.19b, indicate a relaxation time of 6-8 ms for the surface layer. Moreover, the analysis reveals the significant contribution of very short $T_{1\rho}$ times. It's important to emphasize that interpreting the $T_{1\rho}^C$ results for the rigid layer cannot be straightforwardly analyzed in terms of only dynamics. Unlike liquids, where the decay of rotating frame ^{13}C magnetization can be easily understood, solids present a more complex scenario. Here, the nucleus under study experiences fluctuations of the local field not only due to molecular motions but also because of the spin fluctuations of the more abundant ^{1}H nuclei, stemming from their mutual static dipolar interactions. In line with previous research of Vanderhart and Akasaka [122, 157], this complexity can be elucidated through thermodynamic modeling as shown in the schematic in Figure 6.19c. The ^{13}C rotating frame Zeeman system is intricately coupled with the lattice system and the proton dipolar reservoir (i.e. dipolar order as a relevant spin state), represented by the relaxation times $T_{1\rho}^C$ and T_{CH}^D, respectively. Moreover, the proton dipolar order relaxes to the lattice with the relaxation time T_{1D}. Consequently, the experimentally observed relaxation time for the decay of the rotating frame ^{13}C magnetization does not solely reflect the true $T_{1\rho}^C$ value but encompasses effects influenced by the interplay between the $T_{1\rho}^C$, spin-lattice relaxation times, T_{CH}^D spin-spin relaxation occurring between the proton dipolar and ^{13}C rotating frame systems arising from fluctuations in the proton spin

bulk, T_{1D}, (the proton dipolar order spin-lattice relaxation time), and the heat capacity of the proton dipolar reservoir. Thus the ^{13}C rotating frame magnetization decays through two distinct pathways either via $T_{1\rho}^{C}$ relaxation to the lattice or through relaxation facilitated by T_{CH}^{D}, to the proton dipolar reservoir which consistently achieves a uniform spin temperature with the lattice due to the brief relaxation time T_{1D} during sample spinning and thermal equilibrium will therefore quickly be achieved between the two spin systems.
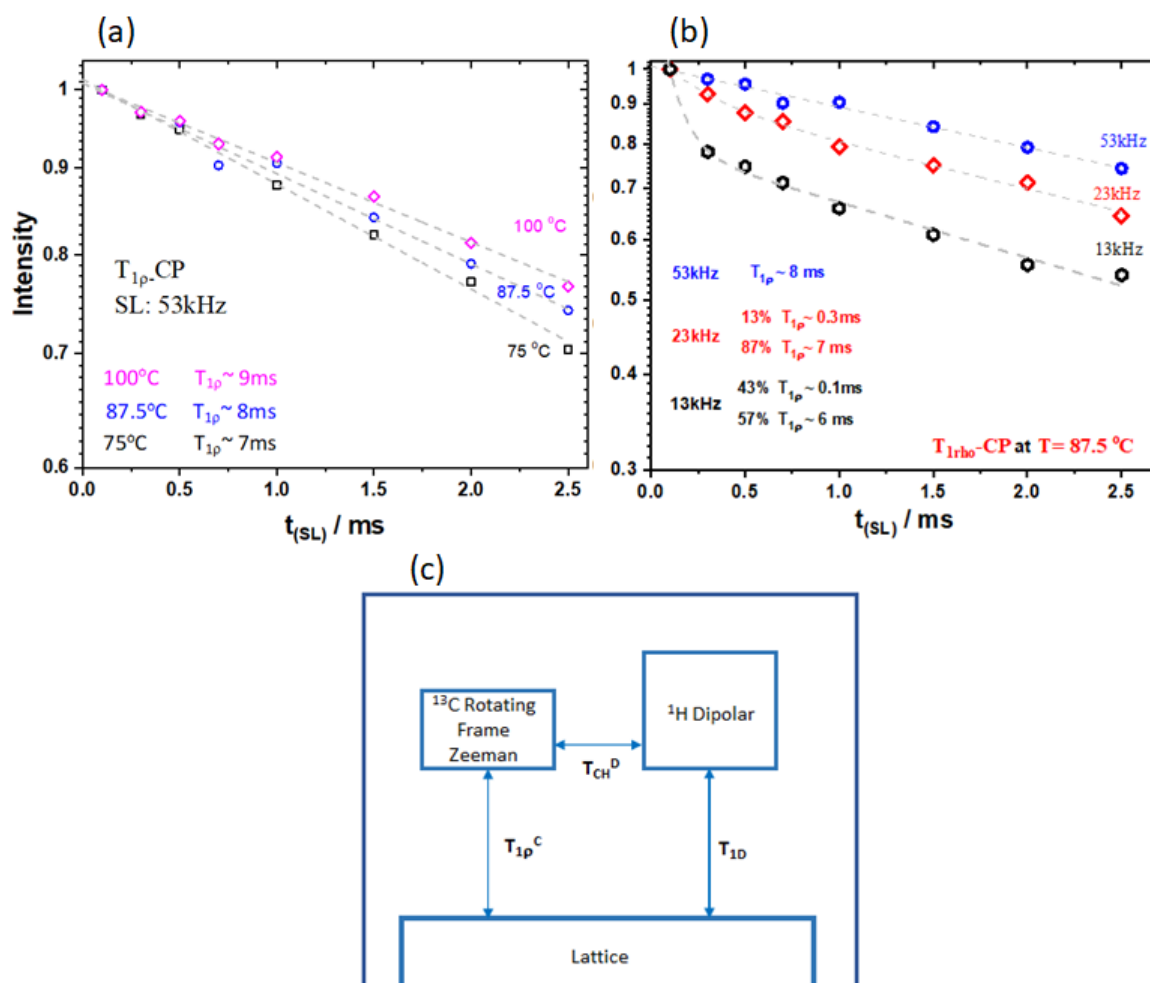
Figure 6.19. ^{13}C cross polarization $T_{1\rho}$ of PEO3k-40nm-0.5 at different a) temperatures and b) spin lock frequencies. c) The schematic is taken from VanderHart's work [122], and represents a thermodynamic model for the carbon rotating frame experiment. In this model, ^{13}C nuclei interact with the lattice via molecular motion characterized by $T_{1\rho}$ and with the ^{1}H dipolar reservoir through spin-spin fluctuations represented by T_{CH}^{D}. The dipolar-order spin-lattice relaxation under carbon decoupling is quantified by T_{1D}.

In our dataset, as shown in Figure 6.19b, a two-component decay is observed in our $T_{1\rho}$ result of the rigid layer at lower rf frequencies. This pronounced dependency on spin lock power for the initial decay has previously been documented by Vanderhart [122] and shows evidence of significant T_{CH}^{D} influence. Indeed the formation of spin-lock magnetization through spin-lock cross-polarization inherently sets the protons in a dipolar-ordered state. In this scenario, two distinct time regimes govern this alteration: the initial decay associated with T_{CH}^{D} processes and the long-time decay would be a combination of true $T_{1\rho}^{C}$ and T_{1D} processes. However, neither period offers direct insights into the motion of the C-H vectors.

Thus, we have to ignore the $T_{1\rho}$ data and exclusively examine T_1 data, employing a straightforward motional model characterized by a single fast process. Additionally, we include the potential presence of a slow process, but it is only accounted for through its order parameter, as T_1 measurements are not sensitive to its timescale. As mentioned previously, the second moment of the static ^{1}H line shape, denoted as M_2, serves as a quantitative measure of this order parameter. At low temperatures ($T \leq -50\,°\mathrm{C}$), M_2 provides valuable insights into both the inter-proton distances and the small-amplitude motions of the CH_2 groups. This behavior of M_2 in the quasi-rigid low-temperature regime is mathematically described by the equation: $M_{2\mathrm{stat}}(T) = (13500 - 20T)\,\mathrm{kHz}^2$, where T represents the temperature in degrees Celsius [158]. The dynamically arranged second moment, denoted as $M_{2\mathrm{dyn}}$, is determined from the FID-based transverse relaxation time, of the rigid layer at higher temperature through the relationship of $M_{2dyn} = 2/T_{2r}{}^2$. Therefore for $T_{2r} = 30\ \mu s$, $M_{2dyn} \sim 2200 kHz^2$ and then we will have the long-time plateau of $S^2 = M_{2dyn}/M_{2stat} \sim 0.154$, where the corresponding motion must be faster than the timescale of the FID, extending up to $50\ \mu s$. Even slower processes remain beyond the scope of detection by $T_{1\rho}$ and T_2 methods.
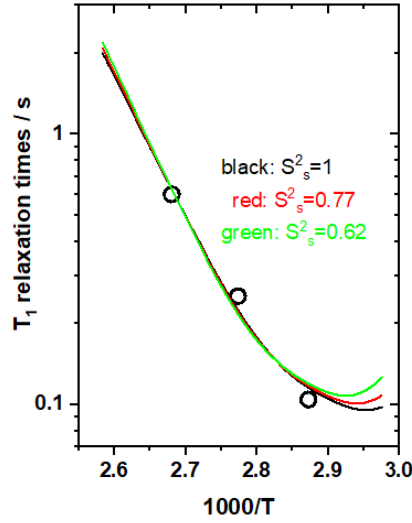
Figure 6.20. The temperature-dependent carbon relaxation times of rigid fraction of PEO/SiO$_2$ composite. The composite, featuring the same polymer molecular weight as the pure matrix, includes 50 volume percent of 40 nm silica nanoparticles.

By performing fitting on the rigid layer T_1 data and maintaining a constant long-term $S^2 = S_f^2 \cdot S_s^2$ value set at 0.154, and permitting a slow process with an order parameter less than one, the fast process proportionally diminishes (table 6.6). This phenomenon results in deteriorated fitting quality, which indicates that a slow process is either not present or has a very high order parameter (i.e. must have a very small amplitude). Therefore, the T_1 values support the presence of a single fast process, as the introduction of a slow process would only worsen the deviation between the lowest measured T_1 and the predicted minimum value.

Table 6.6: Values obtained for fitting the rigid layer T_1 relaxation data.

S$_f^2(fixed)$	S$_s^2 = 0.154/S_f^2$	E$_a(kJ/mol)$	$\tau_f(87^\circ C, ns)$	χ^2
0.154	1	100±1	0.15±0.01	0.093
0.2	0.77	104.1±1.5	0.17±20.02	0.105
0.25	0.62	106.4±2	0.19±0.03	0.121

The observed fast correlation time of 0.15 ns within the adsorbed layer suggests slower dynamics compared to both the mobile fraction (23 ps) and bulk PEO (30 ps). This disparity implies clearly that molecules within the adsorbed layer experi-

ence stronger constraints, leading to reduced mobility. The rigid layer may exhibit characteristics reminiscent of glassy dynamics, potentially featuring a WLF-like divergence. This suggests that the observed high apparent activation energy values are reasonable, given the similarities with glassy dynamics and the fastest dynamics are observed in bulk PEO, reflecting the α relaxation time.

One should note that the distribution of relaxation times cannot be accurately determined due to the limited frequency range of the measurements. To overcome this limitation, measuring the relaxation times in a wider frequency range and at different temperatures is recommended. By doing so, we can avoid the need for a certain temperature dependency assumption and instead implement frequency-temperature superposition, which can provide a more reliable understanding of the dynamic behavior of our system.

Summary

The advancement in the field of nanocomposites has opened avenues for the development of materials with novel and enhanced properties. Understanding the interplay between polymers and nanoparticles is not only fundamental from a scientific perspective but also crucial for tailoring materials that meet the demands of modern technological applications. Polyethylene oxide (PEO), due to its unique properties and wide range of applications, has been a subject of significant interest in the context of nanocomposites. However, the underlying dynamics, especially in confined environments or in the presence of nanoparticles, still possess intriguing facets that warrant deeper investigation. This thesis sheds light on the behavior of PEO in various environments, aiming to bridge the gap between fundamental research and potential practical applications.

The first part of this study aimed to understand the behavior of a unique combination of PEO and sodium fluorohectorite in forming nacre-mimetic nanocomposites. This case is particularly unique due to its fixed d-spacing between clay sheets, a feature that stands in contrast to typical behaviors where interlayer spacing widens with an increase in polymer content. Nacre-mimetic materials are highly sought after for their advanced properties, such as a high barrier against oxygen, exceptional mechanical strength, fire resistance, and glass-like transparency. This study investigated the adsorption behavior of a basic, water-soluble, nonionic PEO and synthetic high-aspect-ratio nano clay to form a simplified model that mimics the structure of the nacre that does not conform to established models, where the expansion of the nanoclay gallery spacing was limited upon increasing amounts of polymer. First, the impact of the water present in the galleries of a nacre-mimetic material was investigated. The research showed that hydration affects the dynamics of polymers and a direct correlation was found between hydration and the mobility of the nanoclay-associated fractions. The results from NMR measurements showed that drying led to

a decrease in mobility, as seen in the shortening of the T_2 values in the early stages of decay. However, due to the difficulties in differentiation between nanoclay-linked PEO and more mobile portions in hydrated samples, the focus was shifted to dried samples.

The study used X-ray diffraction and proton low-resolution solid-state NMR to quantify the amount of mobile and immobilized polymer species within the nanoclay galleries. The analysis of proton time-domain NMR data helped illustrate the separation of confined and free chains, the latter explaining the significant crystallinity in both DSC and NMR experiments. The study finally revealed the unusual confined polymer dynamics, highlighting the crucial role of specific surface interactions. The segmental motion of confined PEO chains between clay layers was found to be faster but initially more restricted than in bulk crystalline PEO. Our results emphasized the importance of specific surface interactions on the dynamics of intercalated polymers and ultimately larger amplitude, as compared to data for PEO absorbed to silica or confined in its own crystal structure.

Our next PNCs model contained silica NPs inserted in PEO. We showed the critical role of the properties of the NPs and the polymer matrix in the overall properties of the nanocomposite material. The results suggested that the adsorption of polymer chains to NPs in different initial solvents even after extended vacuum annealing and solvent evaporation, is a critical factor affecting the structure and dynamics of the interfacial layer in PNCs, and could provide a means of tuning their macroscopic properties. Interestingly, we found that preparing PNCs from ethanol led to a denser packing of chains in the interfacial layer, resulting in a thicker layer. Our findings highlight the potential of simple variations in PNC preparation conditions. The non-polymer contribution of EtOH/H_2O of the adsorbed layer was eliminated.

Then a study was conducted to investigate how heating affects the immobilization of PEO chains by examining the mobility of the polymer at increasing temperatures from 75 to 150°C. The results indicate that raising the temperature did not have a significant effect on the immobilized PEO chains near the particle surface. This observation aligns with the earlier findings by Golitsyn et al. [22]. Furthermore, these outcomes lead to the speculation that a T_g gradient might not exist for PEO. The amount of immobilized polymer and its motional amplitude remained unaltered despite the heating, implying that the stability of the adsorbed polymer chains is mainly

controlled by nanoscale forces, which are not significantly influenced by temperature changes. This idea is based on the monomer density at the polymer/substrate interface. In our system, as the particle diameter increases, there's a pronounced thickening of the adsorbed polymer layer near the particles, which subsequently results in a reduction of local free volume, restricting the conformations of the polymer chains and leading to a high T_g.

Our study also revealed qualitatively different behaviors of PNC dynamics when NPs are of different sizes. The thickness of the interfacial polymer layer surrounding the silica nanoparticle is estimated from the slope of the linear fit of the immobilized polymer fraction from the free induction decay NMR data versus the silica-specific surface. It has been observed that the interfacial layer thickness increases with the size of the particle, and this trend is attributed to changes in curvature. Results revealed that a unit area of a more curved surface effectively immobilizes a smaller amount of segments than a unit area of a flatter surface. This finding has important implications for the potential applications of nanocomposites, as it suggests that it may be possible to adjust the thickness of the bound layer by controlling the size of the nanoparticles. Additionally, the results suggest that very small particles may have an insignificant bound layer, and may ultimately act primarily as plasticizers for the polymer matrix [150]. These insights highlight the potential for tailoring the properties of nanocomposites through careful selection and manipulation of nanoparticle size.

We utilized ^{13}C NMR relaxation time measurements, specifically T_1 and $T_{1\rho}$, to examine the rather special internal dynamics of PEO chains within a confined interfacial layer due to the unusual transverse relaxation time longer than 10-20 μs known for the rigid fraction. $T_{1\rho}$ and T_1 are complementary techniques that provide different types of information about the dynamics of polymer chains. $T_{1\rho}$ probes longer timescales when chain modes are relevant (Rouse modes), and are influenced by the overall dynamics of the chain, while T_1 probes segmental timescale (alpha process), and this process is almost the same for every segment along a chain. Together, these techniques can provide a more complete picture of the dynamics of polymer chains and their interactions with their environment. The data were fitted with a model for C-H vector reorientation which is based on the dipolar relaxation mechanism and is composed of two modes (Although in reality, it is even more because it is an intercon-

nected chain system with modes) a fast segmental relaxation and a mode contribution described by Rouse dynamics for dangling chains, chains linked with one end to the hairy particles. Our data is consistent with the persistent anisotropy. The presence of NPs significantly slowed down the segmental motion by three orders of magnitude. Thus, NMR relaxation measurements have enabled us to explore the dynamic behavior of systems with multiple components and obtain a precise characterization of the segmental dynamics for each component. Despite the limitations of our simple finding approach, our $T_1/T_{1\rho}$ experiments have offered valuable insights into the complex dynamics of our complex multi-component system. More systematic future work may enable the development of more accurate models that can better predict their behavior under different conditions.

In conclusion, it can be concluded that the motional amplitude of PEO is highly dependent on the type of confinement it is subjected to. Whether it is absorbed on the surface of silica particles, intercalated in clay sheets, or confined in its own crystal structure, the motional amplitude of PEO will change accordingly.

References

[1] R. P. Feynman. There's plenty of room at the bottom. *Miniaturization*, 22:282, 1961.

[2] K. Pielichowski and T. M. Majka. *Polymer composites with functionalized nanoparticles: Synthesis, properties, and applications.* Woodhead Publishing, 2018.

[3] S. K. Kumar, B. C. Benicewicz, R. A. Vaia, and K. I. Winey. 50th anniversary perspective: Are polymer nanocomposites practical for applications? *Macromolecules*, 50:714, 2017.

[4] J. H. Koo. *Fundamentals, properties, and applications of polymer nanocomposites.* Cambridge University Press, 2016.

[5] A. R. Payne. The dynamic properties of carbon black-loaded natural rubber vulcanizates. part i. *J. Appl. Polym. Sci.*, 6:57, 1962.

[6] L. Mullins. Softening of rubber by deformation. *Rubber Chem. Technol*, 42:339, 1969.

[7] J.Y. Lee and A. J. Crosby. Crazing in glassy block copolymer thin films. *Macromolecules*, 38:9711, 2005.

[8] Y. A. Kim, T. Hayashi, M. Endo, Y. Gotoh, Wada N, and J. Seiyama. Fabrication of aligned carbon nanotube-filled rubber composite. *Scripta Materialia*, 54:31, 2006.

[9] J. Kalfus and J. Jancar. Relaxation processes in PVAc-HA nanocomposites. *J. Polym. Sci. Part B: Polym. Phys.*, 45:1380, 2007.

[10] T. C. Merke, B. D. Freeman, R. J. Spontak, Z. He, I. Pinnau, P. Meakin, and A. J. Hill. Ultrapermeable, reverse-selective nanocomposite membranes. *Science*, 296:519, 2002.

[11] Henriette M.C. de Azeredo. Nanocomposites for food packaging applications. *Food Res. Int*, 42:1240, 2009.

[12] O. Kojima, A. Usuki, M. Kawasumi, A. Okada, Y. Fukushima, T. Kurauchi, and O. Kamigaito. Mechanical properties of nylon 6-clay hybrid. *J. Mater. Res.*, 8:1185, 1993.

[13] S. K. Kumar and R. Krishnamoorti. Nanocomposites: Structure, phase behavior, and properties. *Annual Review of Chemical and Biomolecular Engineering*, 1:37, 2010.

[14] S. K. Kumar, N. Jouault, B. Benicewicz, and T. Neely. Nanocomposites with polymer grafted nanoparticles. *Macromolecules*, 46:3199, 2013.

[15] N. Pandey, S. K. Shukla, and N. B. Singh. Water purification by polymer nanocomposites: an overview. *Nanocomposites*, 3:47, 2017.

[16] S.C. Tjong. Structural and mechanical properties of polymer nanocomposites. *Mater. Sci.Eng. R. Rep.*, 53:73, 2006.

[17] S. Cheng, A. P. Holt, H. Wang, F. Fan, V. Bocharova, H. Martin, T. Etampawala, B. T. White, T. Saito, N. G. Kang, M. D. Dadmun, J. W. Mays, and A. P. Sokolov. Unexpected molecular weight effect in polymer nanocomposites. *Phys. Rev. Lett.*, 116:038302, 2016.

[18] A. C. Genix, V. Bocharova, B. Carroll, M.Lehmann, T. Saito, S. Krueger, L. He, P. Dieudonné-George, A. P. Sokolov, and J. Oberdisse. Understanding the static interfacial polymer layer by exploring the dispersion states of nanocomposites. *ACS Applied Materials & Interfaces*, 11:17863, 2019.

[19] L. S. Schadler, S. K. Kumar, S. L. Lewis B. C. Benicewicz and, and S. E.Harton. Designed interfaces in polymer nanocomposites: A fundamental viewpoint. *MRS Bulletin*, 32:335, 2007.

[20] A. P. Holt, P. J. Griffin, V. Bocharova, A. L. Agapov, A. E. Imel, M. D. Dadmun, J. R. Sangoro, and A. P. Sokolov. Dynamics at the polymer/nanoparticle interface in poly(2-vinylpyridine)/silica nanocomposites. *Macromolecules*, 47:1837, 2014.

[21] A. P. Holt, V. Bocharova, S. Cheng, A. M. Kisliuk, B. T. White, T. Saito, D. Uhrig, J. P. Mahalik, R. Kumar, A. E. Imel, T. Etampawala, H. Martin,

N. Sikes, B. G. Sumpter, M. D. Dadmun, and A. P. Sokolov. Controlling interfacial dynamics: Covalent bonding versus physical adsorption in polymer nanocomposites. *ACS Nano*, 10:6843, 2016.

[22] Y. Golitsyn, G. J. Schneider, and K. Saalwächter. Reduced-mobility layers with high internal mobility in poly(ethylene oxide)–silica nanocomposites. *J. Chem. Phys.*, 146:203303, 2017.

[23] Bobby B. Carroll, S. Cheng, and A. P. Sokolov. Analyzing the interfacial layer properties in polymer nanocomposites by broadband dielectric spectroscopy. *Macromolecules*, 50:6149, 2017.

[24] S. M. Oh, M. Abbasi, T. J. Shin, K. Saalwächter, and S. Y. Kim. Initial solvent-driven nonequilibrium effect on structure, properties, and dynamics of polymer nanocomposites. *Phys. Rev. Lett.*, 123:167801, 2019.

[25] A. Eckert, M. Abbasi, Thomas. Mang, K. Saalwächter, and A. Walther. Structure, mechanical properties, and dynamics of polyethylenoxide/nanoclay nacre-mimetic nanocomposites. *Macromolecules*, 53:1716, 2020.

[26] S. K. Kumar, V. Ganesan, and R. A. Riggleman. Perspective: Outstanding theoretical questions in polymer-nanoparticle hybrids. *J. Chem. Phys.*, 147:020901, 2017.

[27] N. Jouault, D. Zhao, and S. K. Kumar. Role of casting solvent on nanoparticle dispersion in polymer nanocomposites. *Macromolecules*, 47:5246, 2014.

[28] S. Napolitano and M. Wübbenhorst. The lifetime of the deviations from bulk behaviour in polymers confined at the nanoscale. *Nat.Commun.*, 2:260, 2011.

[29] N. Jouault, J. F. Moll, D. Meng, K. Windsor, S. Ramcharan, C. Kearney, and S. K. Kumar. Bound polymer layer in nanocomposites. *ACS Macro Letters*, 2:371, 2013.

[30] S. Gong, Q. Chen, J. F. Moll, S. K. Kumar, and R. H. Colby. Segmental dynamics of polymer melts with spherical nanoparticles. *ACS Macro. Lett.*, 3:773, 2014.

[31] S. Cheng, V. Bocharova, A. Belianinov, S. Xiong, A. Kisliuk, S. Somnath, A. P. Holt, O. S. Ovchinnikova, S. Jesse, H. Martin, T. Etampawala, M. Dadmun, and A. P. Sokolov. Unraveling the mechanism of nanoscale mechanical reinforcement in glassy polymer nanocomposites. *Nano Letters*, 16:3630, 2016.

[32] S. Cheng, S. J. Xie, J. M. Y. Carrillo, B. Carroll, H. Martin, P. F. Cao, M. D. Dadmun, B. G. Sumpter, V. N. Novikov, K. S. Schweizer, and A. P. Sokolov. Big effect of small nanoparticles: A shift in paradigm for polymer nanocomposites. *ACS Nano*, 11:752, 2017.

[33] P. Hanakata, J. Douglas, and F.Starr. Interfacial mobility scale determines the scale of collective motion and relaxation rate in polymer films. *Nat Commun*, 5:4163, 2014.

[34] Jan-Michael Y. Carrillo, S. Cheng, R. Kumar, M. Goswami, A. P. Sokolov, and Bobby G. Sumpter. Untangling the effects of chain rigidity on the structure and dynamics of strongly adsorbed polymer melts. *Macromolecules*, 48:4207–4219, 2015.

[35] Kenneth S. Schweizer and David S.Simmons. Progress towards a phenomenological picture and theoretical understanding of glassy dynamics and vitrification near interfaces and under nanoconfinement. *J. Chem. Phys*, 151:240901, 2019.

[36] K. Schäler, M. Roos, P. Micke, Y. Golitsyn, A. Seidlitz, T. Thurn-Albrecht, H. Schneider, G. Hempel, and K. Saalwächter. Basic principles of static proton low-resolution spin diffusion NMR in nanophase-separated materials with mobility contrast. *Solid State Nucl. Magn. Reson.*, 72:50, 2015.

[37] K. Schäler, A. Achilles, R. Bärenwald, C. Hackel, and K. Saalwächter. Dynamics in crystallites of poly(ϵ-caprolactone) as investigated by solid-state NMR. *Macromolecules*, 46:7818, 2013.

[38] Malcolm H. Levitt. *Spin Dynamics: Basics of Nuclear Magnetic Resonance.* 2008.

[39] K. Saalwächter. Robust NMR approaches for the determination of homonuclear dipole-dipole coupling constants in studies of solid materials and biomolecules. *Chem. Phys. Chem.*, 14:3000, 2013.

[40] K. Saalwächter. Proton multiple-quantum NMR for the study of chain dynamics and structural constraints in polymeric soft materials. *Prog. Nucl. Magn. Reson. Spectrosc*, 51:1, 2007.

[41] K. Saalwächter and H.W. Spiess. *Polymer Science: A Comprehensive Reference.* Elsevier, 2012.

[42] E. J. Bailey and K. I. Winey. Dynamics of polymer segments, polymer chains, and nanoparticles in polymer nanocomposite melts: A review. *Progress in Polymer Science*, 105:101242, 2020.

[43] C. Fernández de Alba, A. M. Jimenez, M. Abbasi, S. K. Kumar, K. Saalwächter, and G. P. Baeza. On the immobilized polymer fraction in attractive nanocomposites: Tg gradient versus interfacial layer. *Macromolecules*, 54:10289, 2021.

[44] P. Szymoniak, M. Abbasi X. Qu, B. R. Pauw, S. Henning, Z. Li, De-Yi. Wang, C. Schick, K. Saalwächter, and A. Schönhals. Spatial inhomogeneity, interfaces and complex vitrification kinetics in a network forming nanocomposite. *Soft Matter*, 17:2775, 2021.

[45] S. Fotiadou S. Bollas C. Karageorgaki D. Christofilos G. A. Voyiatzis K. Chrissopoulou, K. S. Andrikopoulos and S. H. Anastasiadis. Crystallinity and chain conformation in peo/layered silicate nanocomposites. *Macromolecules*, 44:9710, 2011.

[46] T. J. Bonagamba D. J. Harris and K. Schmidt-Rohr. Conformation of poly(ethylene oxide) intercalated in clay and mos2 studied by two-dimensional double-quantum nmr. *Macromolecules*, 32:6718, 1999.

[47] M. Rubinstein and R.H. Colby. *Polymer Physics.* OUP Oxford, 2003.

[48] G. Strobl. *The physics of polymers.* 3rd ed. Springer, 2007.

[49] L.H. Sperling. *Introduction to physical polymer science.* John Wiley & Sons, 2005.

[50] A. Schönhals, M. Böhning, and P. Szymoniak. *Dynamics of CompositeMaterials.* Springer, 2022.

[51] K. Doolittle. Studies in newtonian flow. ii. the dependence of the viscosity of liquids on free-space. *J. Appl. Phys.*, 12:1471, 1951.

[52] S. Napolitano, C. Rotella, and M. Wübbenhorst. Can thickness and interfacial interactions univocally determine the behavior of polymers confined at the nanoscale? *ACS macro letters*, 1:1189, 2012.

[53] F. Vaca Chávez and K. Saalwächter. Time-domain nmr observation of entangled polymer dynamics: Analytical theory of signal functions. *Macromolecules*, 44:1560, 2011.

[54] A. Mujtaba, M. Keller, S. Ilisch, H. J. Radusch, M. Beiner, T. Thurn-Albrecht, and K. Saalwächter. Detection of surface-immobilized components and their role in viscoelastic reinforcement of rubber–silica nanocomposites. *ACS Macro. Lett.*, 3:481, 2014.

[55] K Ralph Iler. *Solubility, polymerization, colloid and surface properties and biochemistry of silica.* John Wiley and Sons Inc, 1979.

[56] S. M. Jeon S. A. Yang, S. Choi and J. Yu. Silica nanoparticle stability in biological media revisited. *Sci Rep*, 8:185, 2018.

[57] A. K. Pal C. Bharti, U. Nagaich and N. Gulati. Mesoporous silica nanoparticles in target drug delivery system: A review. *Int. J. Pharm. Investig*, 5:124, 2015.

[58] F. Meng, M. Elsahati, J. Liu, and R. F. Richards. Thermal resistance between amorphous silica nanoparticles. *J. Appl. Phys.*, 121:194302, 2017.

[59] K. Chrissopoulou, I. Altintzi, S.H. Anastasiadis, E.P. Giannelis, M. Pitsikalis, N. Hadjichristidis, and N. Theophilou. Controlling the miscibility of polyethylene/layered silicate nanocomposites by altering the polymer/surface interactions. *Polymer*, 46:12440, 2005.

[60] S. S. Ray and M. Okamoto. Polymer/layered silicate nanocomposites: a review from preparation to processing. *Prog. Polym. Sci.*, 28:1539, 2003.

[61] J. Jancar, J. F. Douglas, F. W. Starr, S. K. Kumar, P. Cassagnau, A. J. Lesser, S. S. Sternstein, and M. J. Buehler. Current issues in research on

structure–property relationships in polymer nanocomposites. *Polymer*, 51:3321, 2010.

[62] A. Papon, K. Saalwächter, K. Schäler, L. Guy, F. Lequeux, and H. Montes. Low-field NMR investigations of nanocomposites: Polymer dynamics and network effects. *Macromolecules*, 44:913, 2011.

[63] A. Papon, H. Montes, M. Hanafi, F. Lequeux, L. Guy, and K. Saalwächter. Glass-transition temperature gradient in nanocomposites: Evidence from nuclear magnetic resonance and differential scanning calorimetry. *Phys. Rev. Lett.*, 108:065702, 2012.

[64] A. C. Balazs, T. Emrick, and T. P. Russell. Nanoparticle polymer composites: where two small worlds meet. *Science*, 314:1107, 2006.

[65] K. I. Winey and R. A. Vaia. Polymer nanocomposites. *MRS Bull*, 32:314, 2007.

[66] T. Glomann, G. J. Schneider, J. Allgaier, A. Radulescu, W. Lohstroh, B. Farago, and D. Richter. Microscopic dynamics of polyethylene glycol chains interacting with silica nanoparticles. *Phys. Rev. Lett.*, 110:178001, 2013.

[67] T. Glomann, A. Hamm, J. Allgaier, E. G. Hübner, A. Radulescu, B. Farago, and G. J. Schneider. A microscopic view on the large scale chain dynamics in nanocomposites with attractive interactions. *Soft Matter*, 9:10559, 2013.

[68] J. Fawaz and V. Mittal. *Synthesis Techniques for Polymer Nanocomposites*. John Wiley Sons, Ltd, 2014.

[69] B. J. Anderson and C. F. Zukoski. Rheology and microstructure of polymer nanocomposite melts: Variation of polymer segmentsurface interaction. *Langmuir*, 26:8709, 2010.

[70] H. Barthel. Surface interactions of dimethylsiloxy group-modified fumed silica. *Colloids and Surfaces A: Physicochemical and Engineering Aspects*, 101:217–226, 1995.

[71] H. Montes, T. Chauss´ee, A. Papon, F. Lequeux, and L. Guy. Particles in model filled rubber: Dispersion and mechanical properties. *Eur. Phys. J. E*, 31:263, 2010.

[72] A. Papon, H. Montes, M. Hanafi, K. Saalwächter F. Lequeux, J. Oberdisse, and L. Guy. Solid particles in an elastomer matrix: impact of colloid dispersion and polymer mobility modification on the mechanical properties. *Soft Matter*, 8:4090, 2012.

[73] P. Lepcio, F. Ondreas, K. Zarybnicka, M. Zboncak, O. Caha, and J. Jancar. Bulk polymer nanocomposites with preparation protocol governed nanostructure: the origin and properties of aggregates and polymer bound clusters. *Soft Matter*, 14:2094, 2018.

[74] D. W. Janes, J. F. Moll, S. E. Harton, and C. J. Durning. Dispersion morphology of poly(methyl acrylate)/silica nanocomposites. *Macromolecules*, 44:4920, 2011.

[75] S. E. Harton, S. K. Kumar, H. Yang, T. Koga, K. Hicks, H. Lee, J. Mijovic, M. Liu, R. S. Vallery, and D. W. Gidley. Immobilized polymer layers on spherical nanoparticles. *Macromolecules*, 43:3415, 2010.

[76] J. M. H. M. Scheutjens and G. J. Fleer. Statistical theory of the adsorption of interacting chain molecules. 2. train, loop, and tail size distribution. *J. Phys. Chem*, 84:178, 1980.

[77] D. N. Theodorou. Lattice models for bulk polymers at interfaces. *Macromolecules*, 21:1391, 1988.

[78] O. Guiselin. Irreversible adsorption of a concentrated polymer solution. *Europhysics Letters*, 17:225, 1992.

[79] G. J. Fleer. Polymers at interfaces and in colloidal dispersions. *Adv. Colloid Interface Sci*, 159:99, 2010.

[80] D. N. Voylov, A. P. Holt, B. Doughty, V. Bocharova, H. M. Meyer, S. Cheng, H. Martin, M. Dadmun, A. Kisliuk, and A. P.Sokolov. Unraveling the molecular weight dependence of interfacial interactions in poly(2-vinylpyridine)/silica nanocomposites. *ACS Macro Letters*, 6:68, 2017.

[81] S. Y. Kim, H. W. Meyer, K. Saalwächter, and C. F. Zukoski. Polymer dynamics in PEG-silica nanocomposites: Effects of polymer molecular weight, temperature and solvent dilution. *Macromolecules*, 45:4225, 2012.

[82] Q. Chen, S. Gong, J. Moll, D. Zhao, S. K. Kumar, and R. H. Colby. Mechanical reinforcement of polymer nanocomposites from percolation of a nanoparticle network. *ACS Macro Letters*, 4:398, 2015.

[83] G. P. Baeza, C. Dessi, S. Costanzo, S. Gong D. Zhao, A. Alegria, R. H. Colby, M. Rubinstein, D. Vlassopoulos, and S. K. Kumar. Network dynamics in nanofilled polymers. *Nat Commun*, 7:11368, 2016.

[84] H. Emamy, S. K. Kumar, and F. W. Starr. Diminishing interfacial effects with decreasing nanoparticle size in polymer-nanoparticle composites. *Phys. Rev. Lett.*, 121:207801, 2018.

[85] A. Y. Liu, H. Emamy, J. F. Douglas, and F. W. Starr. Effects of chain length on the structure and dynamics of semidilute nanoparticle–polymer composites. *Macromolecules*, 54:3041, 2021.

[86] J. Feng, S. R. Venna, and D. P. Hopkinson. Interactions at the interface of polymer matrix-filler particle composites. *Polymer*, 103:189, 2016.

[87] E. N. Skountzos, D. G. Tsalikis, P. S. Stephanou, and V. G. Mavrantzas. Individual contributions of adsorbed and free chains to microscopic dynamics of unentangled poly(ethylene glycol)/silica nanocomposite melts and the important role of end groups: Theory and simulation. *Macromolecules*, 54:4470, 2021.

[88] I. Popov, B. Carroll, V. Bocharova, A. C. Genix, S. Cheng, A. Khamzin, A. Kisliuk, and A. P. Sokolov. Strong reduction in amplitude of the interfacial segmental dynamics in polymer nanocomposites. *Macromolecules*, 53:4126, 2020.

[89] D. W. Gidley Ming Zhu H. A. Hristov G. B. DeMaggio, W. E. Frieze and A. F. Yee. Interface and surface effects on the glass transition in thin polystyrene films. *Phys. Rev. Lett.*, 78:1524, 1997.

[90] S. Napolitano and M. Wu1bbenhorst. Dielectric signature of a dead layer in ultrathin films of a nonpolar polymer. *J. Phys. Chem. B*, 111:9197, 2007.

[91] S. Napolitano, A. Pilleri, P. Rolla, and M. Wübbenhorst. Unusual deviations from bulk behavior in ultrathin films of poly(tert-butylstyrene): Can dead layers induce a reduction of T_g? *ACS Nano*, 4:841, 2010.

[92] P. Gin, N. Jiang, C. Liang, T. Taniguchi, and S. K. Satija B. Akgun, M. K. Endoh, and T. Koga. Revealed architectures of adsorbed polymer chains at solid-polymer melt interfaces. *PRL*, 109:265501, 2012.

[93] M. L Braatz, L. I. Meléndez, M. Sferrazza, and S. Napolitano1. Unexpected impact of irreversible adsorption on thermal expansion: Adsorbed layers are not that dead. *The Journal of Chemical Physics*, 146:203304, 2017.

[94] H. Lee, S. Jo, T. Hirata, N. L. Yamada, K. Tanaka, E. Kim, and D. Y. Ryu. Interpenetration of chemically identical polymer onto grafted substrates. *Polymer*, 74:70, 2015.

[95] J. Huang, J. Zhou, and M. Liu. Interphase in polymer nanocomposites. *JACS Au*, 2:280, 2022.

[96] R. P. White and J. E. G. Lipson. Thermodynamic treatment of polymer thin-film glasses. *Phys. Rev. E*, 84:041801, 2011.

[97] J. Xu, D.Li, J. Chen, L. Din, X. Wang, F. Tao, and G. Xue. Detection of interchain proximity and segmental motion of polymer glass. *Macromolecules*, 44:7445, 2011.

[98] D. S. Fryer, P. F. Nealey, and J. de Pablo. Thermal probe measurements of the glass transition temperature for ultrathin polymer films as a function of thickness. *Macromolecules*, 33:6439, 2000.

[99] C. Rotella, S. Napolitano, L. D. Cremer, G. Koeckelberghs, and M. Wübbenhorst. Distribution of segmental mobility in ultrathin polymer films. *Macromolecules*, 43:8686, 2010.

[100] J. L. Keddie and R. A. L. Jones. Glass transition behavior in ultra-thin polystyrene films. *J. Chem.*, 35:21, 1995.

[101] P. Akcora, S. K. Kumar, S. V. García, Y. Li, B. C. Benicewicz, and L. S. Schadler. Segmental dynamics in PMMA-grafted nanoparticle composites. *Macromolecules*, 43:8275, 2010.

[102] F. W. Starr, Douglas J. F, D. Meng, and D. K. Kumar. Bound layers "cloak" nanoparticles in strongly interacting polymer nanocomposites. *ACS Nano*, 10:10960, 2016.

[103] L. Somasekharan, S. Thomas, N. Kalarikkal, and S. Anil Kumar. *Polyhedral Oligomeric Silsesquioxane (POSS) Polymer Nanocomposites*. Elsevier, 2021.

[104] W. Zhang, H. Emamy, B. A. P. Betancourt, F. Vargas-Lara, F. W. Starr, and J. F. Douglas. The interfacial zone in thin polymer films and around nanoparticles in polymer nanocomposites. *Chem. Phys.*, 151, 2019.

[105] F. T. Oyerokun and K. S. Schweizer. Theory of glassy dynamics in conformationally anisotropic polymer systems. *J. Chem. Phys.*, 123:224901, 2005.

[106] H. Gunther. Wiley Chichester, 1980.

[107] J. H. Keeler. *Understanding NMR Spectroscopy*. John Wiley & Sons, Inc., 2013.

[108] W-K. Rhim, A. Pines, and J. S. Waugh. Time-reversal experiments in dipolar-coupled spin systems. *Phys. Rev. B*, 3:684, 1971.

[109] A. Pines, W. Rhim, and J. S. Waugh. Homogeneous and inhomogeneous nuclear spin echoes in solids. *Journal of Magnetic Resonance*, 6:457, 1972.

[110] E. L. Hahn. Spin echoes. *Phys. Rev.*, 80:580, 1950.

[111] A. Lozovoi, C. Mattea, M. Hofmann, K. Saalwächter, N. Fatkullin, and S. Stapf. Segmental dynamics of polyethylene-alt-propylene studied by NMR spin echo techniques. *J. Chem. Phys.*, 146:224901, 2017.

[112] M. H. Levitt and R. Freeman. Composite pulse decoupling. *Journal of Magnetic Resonance (1969)*, 43:502, 1981.

[113] B. J. Suh, F. Borsa, and D. R. Torgeson. Use of an alternating-phase CPMG sequence to avoid spin-locking effects in T_2 measurements in solids. *J. Magn. Reson, Series A*, 110:58, 1994.

[114] A. E. Bennett, C. M. Rienstra, M. Auger, K. V. Lakshmi, and R. G. Griffin. Heteronuclear decoupling in rotating solids. *J. Chem. Phys.*, 103:6951, 1995.

[115] S.R. Hartmann and E.L. Hahn. Nuclear double resonance in the rotating frame. *Phys. Rev.*, 128:2042, 1962.

[116] M. J. Duer. *Introduction to solid-state NMR spectroscopy.* Wiley-Blackwell, 2004.

[117] M. J. Duer. *Solid-State NMR Spectroscopy Principles and Applications.* John Wiley Sons, Ltd, 2001.

[118] G. Metz, X. Wu, and S. O. Smith. Ramped-amplitude cross polarization in Magic-Angle-Spinning NMR. *J. Magn. Reson*, 110:219, 1994.

[119] G. Metz, M. Ziliox, and S.O. Smith. Towards quantitative CP-MAS NMR. *Solid State Nucl. Magn. Reson.*, 7:155, 1996.

[120] J.-D. Mao, W.-G. Hu, K. Schmidt-Rohr, G. Davies, E.A. Ghabbour, and B. Xing. Quantitative characterization of humic substances by solid-state ^{13}C NMR. *Soil Sci. Soc. Am. J.*, 64:873, 2000.

[121] D. A. Torchia. The measurement of proton-enhanced carbon-13 t1 values by a method which suppresses artifacts. *J. Magn. Reson.*, 30:613, 1976.

[122] D. L. VanderHart and A. N. Garroway. 13C NMR rotating frame relaxation in a solid with strongly coupled protons: Polyethylene. *J. Chem. Phys.*, 71:2773, 1979.

[123] A. Krushelnitsky and D. Reiehert. Response of lysozyme internal dynamics to hydration probed by ^{1}H and ^{13}C solid-state NMR relaxation. *Appl. Magn. Reson.*, 27:501, 2004.

[124] P. Ma, J. D. Haller, P. Macek J. Zajakala, A. C. Sivertsen, D. Willbold, J. Boisbouvier, and P. Schanda. Probing transient conformational states of proteins by solid-state $R_{1\rho}$ relaxation-dispersion NMR spectroscopy. *Angew Chem Int Ed Engl.*, 53:4312, 2014.

[125] A. Krushelnitsky, D. Gauto, D. C. Rodriguez Camargo, P. Schanda, and K. Saalwächter. Microsecond motions probed by near-rotary-resonance $R_{1\rho}$ ^{15}N mas NMR experiments: the model case of protein overall-rocking in crystals. *J Biomol NMR*, 71:53, 2018.

[126] V. D. Fedotov, N. P. Obuchov, R. A. Zadikhanov, J. Spevacek, and J. Straka. ^{1}H and ^{13}C nuclear magnetic relaxation and local dynamics of lysozyme and synthetic polypeptides. *Appl. Magn. Reson.*, 4:491, 1993.

[127] R. Kurbanov, T. Zinkevich, and A. Krushelnitsky. The nuclear magnetic resonance relaxation data analysis in solids: General $R_1/R_{1\rho}$ equations and the model-free approach. *J. Chem. Phys*, 135:184104, 2011.

[128] C. Ammann, P. Meier, and A. E. Merbach. A simple multinuclear NMR thermometer. *Journal of Magnetic Resonance*, 46:319, 1982.

[129] W. Stöber, A. Fink, and E. Bohn. Controlled growth of monodisperse silica spheres in the micron size range. *J. Colloid Interface Sci.*, 26:62, 1968.

[130] F. Barthelat. Nacre from mollusk shells: a model for high-performance structural materials. *Bioinspiration Biomimetics*, 5:035001, 2010.

[131] J. Sun and B. Bhushan. Hierarchical structure and mechanical properties of nacre: a review. *RSC Adv.*, 2:7617, 2012.

[132] and T.J. Harvey I. Corni, J. A. Wharton, K. R. Stokes, F. C. Walsh, and R. J. K. Wood. A review of experimental techniques to produce a nacre-like structure. *Bioinspiration Biomimetics*, 7:031001, 2012.

[133] P. Das, J. M. Malho, K. Rahimi, F. H. Schacher, B. Wang, D. E. Demco, and A. Walther. Nacre-mimetics with synthetic nanoclays up to ultrahigh aspect ratios. *Nat. Commun.*, 6:1, 2015.

[134] A. Walther, I. Bjurhager, J. M. Malho, J. Pere, J. Ruokolainen, L. A. Berglund, and O. Ikkala. Large-area, lightweight and thick biomimetic composites with superior material properties via fast, economic, and green pathways. *Nano Letters*, 10:2742, 2010.

[135] T. Tigges and A. Walther. Hierarchical self-assembly of 3D printed Lock-and-Key colloids through shape recognition. *Angew. Chem. Int. Ed.*, 55:11261, 2016.

[136] R. M. Hodge, T. J.Bastow, G. H. Edward, G. P. Simon, and A. J. Hill. Free volume and the mechanism of plasticization in water-swollen poly(vinyl alcohol). *Macromolecules*, 29:8137, 1996.

[137] T. Verho, M. Karesoja, P. Das, L. Martikainen, R. Lund, A. Alegría, A. Walther, and O. Ikkala. Hydration and dynamic state of nanoconfined polymer layers govern toughness in nacre-mimetic nanocomposites. *Advanced Materials*, 25:5055, 2013.

[138] R. Kurz, A. Achilles, W. Chen, M. C. Schäfer, A. Seidlitz, Y. Golitsyn, J. Kressler, W. Paul, G. Hempel, T. Miyoshi, T. Thurn-Albrecht, and K. Saalwächter. Intracrystalline jump motion in poly(ethylene oxide) lamellae of variable thickness: A comparison of NMR methods. *Macromolecules*, 50:3890, 2017.

[139] J. Krzaczkowska, M. Strankowski, S. Jurga, K. Jurga, and A. Pietraszko. NMR dispersion studies of poly(ethylene oxide)/sodium montmorillonite nanocomposites. *J. Non-Cryst. Solids*, 356:945, 2010.

[140] B. J. Anderson and C. F. Zukoski. Rheology and microstructure of entangled polymer nanocomposite melts. *Macromolecules*, 42:8370, 2009.

[141] K. Saalwächter, M. Krause, and W.Gronski. Study of molecular interactions and dynamics in thin silica surface layers by proton solid-state NMR spectroscopy. *Chem. Mater.*, 16:4071, 2004.

[142] D. R. Kinney, I. S. Chuang, and G. E. Maciel. Water and the silica surface as studied by sariable temperature high resolution ^{1}H NMR. *J. Am. Chem. Soc.*, 115:6786, 1993.

[143] M. C. Wapler, J. Leupold, I. Dragonu, D. von Elverfeld, M. Zaitsev, and U. Wallrabe. Magnetic properties of materials for MR engineering, micro-MR and beyond. *Journal of Magnetic Resonance*, 242:233, 2014.

[144] D. S. Fryer, R. D. Peters, E. J. Kim, J. E. Tomaszewski, J. J. de Pablo, P. F. Nealey, Chris C. White, and Wen li. Wu. Dependence of the glass transition temperature of polymer films on interfacial energy and thickness. *Macromolecules*, 34:5627, 2001.

[145] C. Rotella, M. Wübbenhorst, and S. Napolitano. Probing interfacial mobility profiles via the impact of nanoscopic confinementon the strength of the dynamic glass transition. *Soft Matter*, 7:5260, 2011.

[146] P. G. de Gennes. Scaling theory of polymer adsorption. *Journal de Physique*, 37:1445, 1976.

[147] P. G. de Gennes. Conformations of polymers attached to an interface. *J. Theor. Exp. Phys.*, 13:1069, 1980.

[148] N. Jouault, M. K. Crawford, C. Chi, R. J. Smalley, J. Jestin B. Wood, Y. B. Melnichenko, W. E. Guise L. He, and S. K. Kumar. Polymer chain behavior in polymer nanocomposites with attractive interactions. *ACS Macro Lett.*, 5:523, 2016.

[149] P. J. Griffin, V. Bocharova, L. R. Middleton, R. J. Composto, N. Clarke, K.S. Schweizer, and K. I.Winey. Influence of the bound polymer layer on nanoparticle diffusion in polymer melts. *ACS Macro Lett.*, 5:1141, 2016.

[150] K. N. Raftopoulos and K. Pielichowski. Segmental dynamics in hybrid polymer/poss nanomaterials. *Prog. Polym. Sci.*, 52:136, 2016.

[151] S. Gam, J. S. Meth, S. G. Zane, C. Chi, B. A. Wood, M. E. Seitz, K. I. Winey, N. Clarke, and R. J. Composto. Macromolecular diffusion in a crowded polymer nanocomposite. *Macromolecules*, 44:3494, 2011.

[152] Y. Li, D. Wei, C. C. Han, and Q. Liao. Dynamics of polymer melts confined by smooth walls: Crossover from nonentangled region to entangled region. *J. Chem. Phys.*, 126:204907, 2007.

[153] H. Meyer, T. Kreer, A. Cavallo, J. P. Wittmer, and J. Baschnagel. On the dynamics and disentanglement in thin and two-dimensional polymer films. *Eur. Phys. J. Special Topics*, 141:167, 2007.

[154] R. A. Riggleman, G. Toepperwein, G. J. Papaconstantopoulos, J.-L. Barrat, and J. J. de Pablo. Large-area, lightweight and thick biomimetic composites with superior material properties via fast, economic, and green pathways. *J. Chem. Phys.*, 130:244903, 2009.

[155] J. Martín, M. Krutyeva, M. Monkenbusch, A. Arbe, J. Allgaier, A. Radulescu, P. Falus, J. Maiz, C. Mijangos, J. Colmenero, and D. Richter. Direct observation of confined single chain dynamics by neutron scattering. *Phys. Rev. Lett.*, 104:197801, 2010.

[156] D. W. McCall. Nuclear magnetic resonance studies of molecular relaxation mechanisms in polymers. *Acc. Chem. Res.*, 4:223, 1971.

[157] K. Akasaka, S. Ganapathy, C. A. McDowell, and A. Naito. Spin–spin and spin-lattice contributions to the rotating frame relaxation of ^{13}C in L-alanine. *J. Chem. Phys.*, 78:3567, 1983.

[158] Y. Golitsyn, M. Pulst, J. Kressler, and D. Reichert. Molecular dynamics in the crystalline regions of poly(ethylene oxide) containing a well-defined point defect in the middle of the polymer chain. *JPC B*, 121:4620, 2017.

Erklärung

Hiermit versichere ich, die vorliegende Arbeit selbstständig und ohne fremde Hilfe verfasst und keine anderen als die von mir angegebenen Quellen und Hilfsmittel verwendet zu haben. Die den benutzten Werken wörtlich oder inhaltlich entnommenen Stellen habe ich als solche kenntlich gemacht.

Ich erkläre, keine anderweitigen Promotionsversuche unternommen und die vorliegende Dissertation weder in der jetzigen noch in einer anderen Fassung einer anderen wissenschaftlichen Einrichtung vorgelegt zu haben.

Halle (Saale), den   Mozhdeh Abbasi

Acknowledgments

I extend my heartfelt gratitude to all the amazing people who helped me throughout my doctoral journey.

First and foremost, I am deeply grateful to Prof. Dr. Kay Saalwächter for granting me the opportunity to join his research group. His unwavering support, both during my time in the NMR group at Martin Luther University and after I moved to Munich, was invaluable to me.

To everyone in the NMR group, thank you for making work enjoyable and for being great company, especially Dr. Tiago Mendes Ferreira and Dr. Mareen Schäfer for creating a welcoming office environment.

My gratitude knows no bounds for Dr. Alexey Krushelnitsky and Dr. Günter Hempel, whose guidance and assistance were indispensable during my time with the group and beyond. Their support, even through distant emails, has been a source of strength.

I owe a great deal to the friendship and kindness of my dear friends Dr. Farhad Shahsavan, Faryal Farahani, and Ammar Kaboul whose constant support and encouragement served as guiding lights during the most challenging phases. Their presence and support have been a source of joy and positivity.

To my beloved family, I cannot begin to express the depth of my gratitude. Your endless love, unwavering support, and steadfast belief in me have been the solid foundation upon which I've pursued my goals.

Publications

1. C. Fernández-de-Alba, and A. M. Jimenez, and **M. Abbasi**, and S. K. Kumar, and K. Saalwächter and G. P. Baeza, On the Immobilized Polymer Fraction in Attractive Nanocomposites: T_g Gradient versus Interfacial Layer, Macromolecules 54, 10289, 2021.

2. P. Szymoniak, and X. Qu, and **M. Abbasi**, and B. R. Pauw, and S. Henning, and Z. Li, and De-Yi. Wang, and C. Schick, and K. Saalwächter and A. Schönhals, Spatial inhomogeneity, interfaces and complex vitrification kinetics in a network forming nanocomposite, Soft Matter 17, 2775, 2021

3. A. Eckert, and **M. Abbasi**, and Thomas. Mang, and K. Saalwächter and A. Walther, Structure, Mechanical Properties, and Dynamics of Polyethylenoxide/Nanoclay Nacre-Mimetic Nanocomposites, Macromolecules, 53, 1716, 2020.

4. S. M. Oh, and **M. Abbasi**, and T. J. Shin, and K. Saalwächter and S. Y. Kim, Initial Solvent-Driven Nonequilibrium Effect on Structure, Properties, and Dynamics of Polymer Nanocomposites, Phys. Rev. Lett. 123, 167801, 2019.

Curriculum Vitae

Personal data

Family name: Abbasi
First name: Mozhdeh

Education

Jun 2017 - Oct 2024   **Ph.D. in Physics**, *Martin Luther University Halle-Wittenberg, Institute of Physics, Faculty of Natural Sciences II*

Okt 2010 - Aug 2013   **M.Sc. Physics**, *Guilan University, Institute of Physics, Faculty of Natural Sciences*, Rasht (Iran)

Okt 2005 - Jul 2009   **B.Sc. Physics**, *Guilan University, Institute of Physics, Faculty of Natural Sciences*, Rasht (Iran)

Work Experience

Jun 2023 - Present   **Applied Laboratory Manager**, **Product developer**, *PNDetector GmbH, Munich, Germany*

Jun 2017 - Dec 2022   **Research Associate and Lecturer at Martin Luther University Halle-Wittenberg**, *Institute of Physics, Faculty of Natural Sciences II*

Sep 2011 - Jan 2017   **Lecturer and Laboratory Director at Guilan University**, *Institute of Physics, Faculty of Natural Sciences*, Rasht (Iran)

Halle (Saale), den   Mozhdeh Abbasi